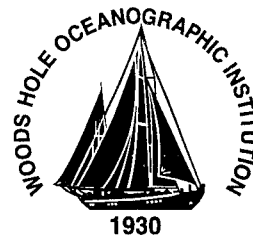# Massachusetts Institute of Technology

Woods Hole Oceanographic Institution
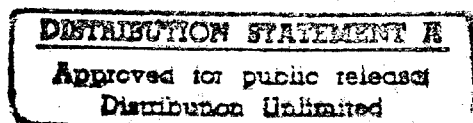
Joint Program
in Oceanography/
Applied Ocean Science
and Engineering

1930

DOCTORAL DISSERTATION

Estimating Open-Ocean Boundary Conditions:
Sensitivity Studies

by

19960509 062

James R. Gunson

September 1995

MIT/WHOI
95-23

Estimating Open-Ocean Boundary Conditions:
Sensitivity Studies

by

James R. Gunson

Massachusetts Institute of Technology
Cambridge, Massachusetts 02139

and

Woods Hole Oceanographic Institution
Woods Hole, Massachusetts 02543

September 1995

DOCTORAL DISSERTATION
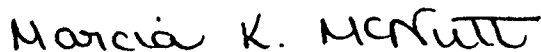
Approved for publication; distribution unlimited.

Approved for Distribution:

Philip L. Richardson

Philip L. Richardson, Chair
Department of Physical Oceanography

Marcia K. McNutt

Marcia K. McNutt
MIT Director of Joint Program

John W. Farrington

John W. Farrington
WHOI Dean of Graduate Studies

ESTIMATING OPEN–OCEAN BOUNDARY CONDITIONS: SENSITIVITY STUDIES

by

James Reginald Gunson

B.Sc.(Hons.) The Flinders University of South Australia.
(1988)

Submitted in partial fulfillment of the
requirements for the degree of

Doctor of Philosophy

at the

MASSACHUSETTS INSTITUTE OF TECHNOLOGY

and the

WOODS HOLE OCEANOGRAPHIC INSTITUTION

August 1995

© James R. Gunson 1995

Signature of Author .... *James Gunson* ....
Joint Program in Physical Oceanography
Massachusetts Institute of Technology
Woods Hole Oceanographic Institution
August 24, 1995

Certified by .... *Paola Malanotte-Rizzoli* .
Paola Malanotte–Rizzoli
Professor of Physical Oceanography
Thesis Supervisor

Accepted by.......................................
Carl Wunsch
Chairman, Joint Committee for Physical Oceanography
Massachusetts Institute of Technology
Woods Hole Oceanographic Institution

ESTIMATING OPEN-OCEAN BOUNDARY CONDITIONS: SENSITIVITY STUDIES

by

James Reginald Gunson

Submitted in partial fulfillment of the requirements for the degree of
Doctor of Philosophy at the Massachusetts Institute of Technology
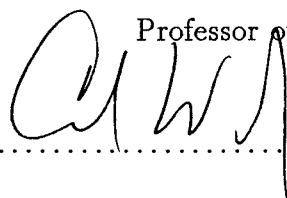and the Woods Hole Oceanographic Institution
August 29, 1995

Abstract

The problem of estimating boundary and initial conditions for a regional open–ocean model is addressed here. With the objective of mimicking the SYNOP experiment in the Gulf Stream system, a meandering jet is modeled by the fully nonlinear barotropic vorticity equation. Simulated observations of current velocity are taken using current meters and acoustic tomography. Twin experiments are performed in which the adjoint method is used to reconstruct the flow field. The estimated flow is forced to resemble the true flow by minimizing a cost function with respect to some control variables. At the minimum, the error covariance matrix of the estimated control variables can be evaluated from the inverse Hessian of the cost function.

The first major scientific objective of this work is the estimation of initial and boundary conditions for the model from sparse interior data. First the vorticity initial conditions are used as control variables and the boundary conditions are kept fixed. The jet–like flow is found to induce strong dependence of the model/data misfit upon the specified boundary conditions. Successively, the boundary values of streamfunction and vorticity are included among the control variables and estimated together with the initial conditions. Experiments are performed with various choices of scaling and first guess for the control variables, and various observational strategies. The first major new result obtained is the successful estimation of the complete set of initial and boundary conditions, necessary to integrate the vorticity equation forward in time. From a time–invariant first guess for the boundary conditions, the assimilation is able to create temporal variations at the boundaries that make the interior flow match well the velocity observations, even when noise is added. It is found that information from the observations is communicated to the boundaries by advection of vorticity and by the instantaneous domain–wide connections in the streamfunction field due to the elliptic character of the Poisson equation.

The second major scientific objective is the estimation of error covariances in the presence of strongly nonlinear dynamics. The evaluation of the full error covariance matrix for the estimated control variables from the inverse Hessian matrix is investigated along with its dependence upon the degree of nonlinearity in the dy-

3

namics. Further major new results here obtained are the availability of off-diagonal covariances, the successful calculation of error covariances for all boundary and initial conditions, and the estimation of errors for the interior fields of streamfunction and vorticity. The role of the Hessian matrix is assessed in gauging the sensitivity of the estimated boundary and initial conditions to the data. Also, the importance is stressed of retaining off–diagonal structure of the Hessian to obtain more accurate error estimates.

Thesis Supervisor: Paola Malanotte–Rizzoli,
Professor of Physical Oceanography
Department of Earth, Atmospheric and Planetary Sciences
Massachusetts Institute of Technology

Acknowledgements

Errors using inadequate data are much less than those using no data at all.

– Charles Babbage

Contents

Introduction

During 1988 and 1989, a moored array of current meters and acoustic tomographic transceivers were deployed at 39°N, 55°W in the northwest Atlantic Ocean. This array was part of the SYNOP (Synoptic Ocean Prediction) experiment and the purpose of the deployment was to provide time series of velocity, temperature and acoustic travel times, as a foundation for modeling and assimilation studies. A motivation for these studies was to construct the observed spatial and temporal behavior of a strong western boundary current, ie. the the Gulf Stream, to study the dynamics of the system.

Of particular interest is the high eddy kinetic energy found along the Gulf Stream axis, extending considerable distances into the interior (see maps in Schmitz, 1976, and Wyrtki, 1976). Some theoretical and modelling studies, Gill *et al.* (1974) and Holland & Rhines (1980), indicate that the southern recirculation is a region of baroclinic instability and could be a source of eddy energy. Bryden (1982) and Hogg (1985) looked for evidence of this baroclinic instability from observations taken in the southern recirculation. However the sparsity of the observations (LDE and POLYMODE) in space made it difficult to measure the growth rates and vertical phase propagation associated with baroclinic instability. Using objective analysis and quasigeostrophy, Hua *et al.* (1986), extrapolated data from the LDE experiment to produce three–dimensional maps of streamfunction and potential vorticity, but the mapping requires *a priori* spatial covariances to be supplied. Furthermore the temporal behavior of mapped fields is difficult to estimate from data alone. All of these

studies point to the desirability of extrapolating information from the observations in space and time using dynamical constraints.

An alternative source of eddy activity in the southern recirculation region is the radiation of planetary waves by the Gulf Stream. Pedlosky (1977), Malanotte–Rizzoli (1984) and Hogg (1988) present theoretical studies of the processes by which the Gulf Stream could radiate planetary waves, and numerical modelling experiments were performed by Malanotte–Rizzoli et al. (1987, 1995) to investigate these processes. The Eliassen–Palm relation for time–mean flows, which arises from the conservation of enstrophy (Plumb, 1986), predicts that the radiated waves can interact with the mean flow in the southern recirculation to produce eddies. Chester et al. (1994) was able to measure the radiative component of the Eliassen–Palm relation using data from the SYNOP East array at 55°W. Knowing the relative sizes of terms in the Eliassen–Palm relation will determine whether the region is a source or sink of eddy enstrophy, and whether wave radiation is significant.

Unfortunately both physical processes, baroclinic instability and wave radiation, require estimates of eddy potential vorticity fluxes over long periods of time which are difficult to make from observations. However potential vorticity conservation may be used as a dynamical interpolater to extract as much information as possible from the available data and to construct spatially and temporally varying fields of potential vorticity. The assimilation of temperature and velocity observations from the SYNOP East array, into a dynamical model of the ocean in the region of the southern recirculation, is necessary in order to perform such a dynamical interpolation and to examine the physical processes.

Thus, a prime motivation for model/data assimilations is the potential to construct the behavior of a dynamical system in regions of space and time that are devoid of data. The assimilation allows the construction of fields of important dynamical quantities, such as potential vorticity, which could not otherwise be directly observed in the real ocean. An assimilation may also supply error estimates to give a level of

9

confidence for the estimated fields. An attractive feature of the SYNOP data set for assimilation studies is that motions due to the Gulf Stream have high signal to noise ratio compared to other, more quiescent, parts of the ocean. Meanders and rings provide coherent signals in the data, which a dynamical model can reproduce.

The prospect of assimilating the SYNOP East data into an ocean model immediately raises two important issues. First, the large horizontal velocity gradients observed in the Gulf Stream and its recirculations imply that fully nonlinear dynamics are needed to adequately model the flow. Second, the SYNOP East observing array covers a rectangular region approximately 200 km by 600 km, straddling the Gulf Stream at 55°W. To successfully constrain an ocean model using this dataset alone, the spatial extent of the model domain cannot be too great, otherwise large regions of the model will not be influenced by the data. Thus, a basin–scale model may not be the most useful and the model domain may be chosen so as its boundaries are in the open ocean. These two issues have important implications for the model/data assimilation.

The issues of assimilation in the presence of strong nonlinearity and the implementation of open boundaries are of fundamental importance to modeling and assimilation studies. They are challenging issues that need to be fully investigated and understood. In this study, model/data assimilations are performed using simulated velocity observations with a simple nonlinear dynamical model (barotropic conservation of vorticity). With simulated data the true flow field is known, thus the estimated flow field from the assimilation can be directly compared to the true flow field. The effects of nonlinear dynamics and the presence of open boundaries on estimated dynamical fields and their error estimates can thus be well investigated. This idealized approach is a necessary first step before the actual SYNOP East dataset can be assimilated into an open–ocean model.

The fundamental difficulty caused by strongly nonlinear dynamics in assimilation studies is the unpredictability of error growth as the model state evolves forward

10

in time. For simple dynamical models, the dependence of predictability upon the degree of nonlinearity has been studied by Vallis (1983) and Lacarra & Talagrand (1988). Robinson & Haidvogel (1980) investigated error growth in a barotropic open ocean model identifying three sources of error: 1) physical errors due to inadequate representation of unresolved scales of motion; 2) computational errors due to truncation errors in the discretization and inaccurate implementation of the open boundaries and 3) observational errors in the available data, including inaccuracies in the initial conditions and boundary conditions. The propagation of errors in a strongly nonlinear model is a nontrivial issue.

Traditionally oceanographers have assimilated data into nonlinear models by linearizing the dynamics about some known model state (see Ghil & Malanotte–Rizzoli, 1991, for a review of assimilation methods). This enables the temporal evolution of the dynamical fields to be expressed in transition matrix form (Bryson & Ho, 1975), allowing the propagation of errors to be calculated, as is done in the extended Kalman filter. However, for many oceanographic cases, such as the variability of the Gulf Stream system under study here, a fully nonlinear model needs to be used for data assimilation. There is a limited choice of assimilation methods available (Evenson, 1994).

The adjoint method allows assimilation of data into a strongly nonlinear model without linearizing the dynamics. A decription of the adjoint method, as it is implemented here, is presented in the appendix. Details on the history of this assimilation method may be found in Bennett (1992), Ghil & Malanotte–Rizzoli (1991) and Talagrand & Courtier (1987). In short, the adjoint method minimizes a cost function which expresses the distance between the true observations and those produced by the model. The minimum of the cost function is found by varying a set of control variables.

Generally, the control variables are some subset of the model parameters. Schröter & Wunsch (1986) and Tziperman & Thacker (1989) used wind–stress curl,

11

frictional parameters and initial conditions as control variables for nonlinear barotropic models in a basin, and successfully assimilated simulated data. Moore (1991) used initial conditions as control variables to assimilate real satellite altimetric data from GEOSAT into a quasi–geostrophic open ocean model of the Gulf Stream system. The boundary conditions were kept at prescribed values throughout the assimilation. A quasi–geostrophic open–ocean model of the Gulf Stream was also used by Seiler (1993) in an adjoint assimilation using simulated GEOSAT data. Here the boundary conditions were used as control variables and the initial conditions were prescribed.

None of these previous studies have addressed the issue of estimating the error in the estimated fields in the presence of strong nonlinearity. When the minimum of the cost function is found, the Hessian matrix of the cost function may be inverted to give the estimated error covariances in the estimated control variables (Thacker, 1989). While this inversion is possible, the cost function contains multiple local minima when the dynamics are strongly nonlinear, and the adjoint method may provide convergence to one of these local minima and not to the global minimum. Thus, care must be taken in interpreting error estimates from the inverse Hessian.

The first major scientific objective of this dissertation is the optimal estimation of the flow field from sparse data, and the estimation of the error covariances, in the presence of strongly nonlinear dynamics.

The problem of open boundaries in a regional model has been with oceanographers and meteorologists for a long time. Charney *et al.* (1950) first addressed the problem for dynamics governed by the barotropic vorticity equation. They discovered a sufficient set of boundary conditions to integrate the model forward in time, namely: vorticity throughout the interior at the initial time, streamfunction over all the open boundary at all times, and vorticity at inflow parts of the open boundary at all times. This approach had been generally accepted until Miller & Bennett (1988) pointed out that the open–boundary problem, as configured by Charney *et al.*, is formally ill–posed. The ill–posedness arises at so–called characteristic points on the

open boundary, where the component of the flow normal to the open boundary is zero. At these points, the streamline is locally tangent to the boundary, and the transition from inflow to outflow occurs. Hence, there is an overspecification of vorticity in the limit as one approaches a characteristic point, due to the specification of vorticity at the inflow in tandem with the conservation of vorticity along the streamline. The overspecification of vorticity at characteristic points can give rise to infinite vorticity gradients, Bennett & Kloeden (1981). This rather subtle point is discussed at length in chapter eight of Bennett (1992). This problem may be circumvented to some degree by applying a smoothing operator along the boundaries, as was done in the numerical experiments of Robinson & Haidvogel (1980). The ill–posedness of the forward model at characteristic points on the boundary is not an objective of the present study. In this study the boundary vorticity is smoothed as part of the assimilation, preventing the formation of large vorticity gradients.

With the aim of assimilating SYNOP East data into an open ocean model, there are two choices available for the implementation of open boundaries. The first is to specify ahead of time, the boundary values of dynamical quantities sufficient to integrate the model. Until now this has been the most common technique used in open ocean assimilation studies (see Moore, 1991; Robinson *et al.*, 1988). However, in real situations the dynamical fields at the open boundaries are generally unknown. Modelers have therefore usually estimated the boundary values from some climatological large–scale dataset such as Levitus (1982), or taken the boundary values from a basin–scale model in which the local domain is embedded. With these approaches a sponge layer may be included around the boundaries to lessen the influence of errors due to the imposed boundary values (Cummins & Mysak, 1988, Chapman, 1985).

A more desirable yet more difficult approach is to estimate the open boundary conditions as part of the assimilation study. The dynamics may be used to extrapolate information from the observations to the boundaries. Zou *et al.* (1995) used a sequential estimation scheme to estimate open boundary conditions from interior

data for a barotropic model. The size of the estimation problem was reduced by estimating the boundary conditions at one time from the interior data only at that time. Time–dependent boundary conditions were estimated by Seiler (1993) using the adjoint method with quasigeostrophic dynamics. Also Bennett & McIntosh (1982) used a variational formulation with a linearized shallow–water equation model to estimate boundary conditions in a coastal model. These previous studies focussed on the estimation of the boundary conditions and did not include the initial conditions in the assimilation.

The major difficulty with time–dependent boundary conditions is that in general there are a great number of boundary values to be estimated, from relatively few data points. To address this difficulty, terms can be included in the cost function to penalize departures of the first–order statistics of the boundary conditions during the assimilation, from their *a priori* values. The *a priori* first–order statistics can be the expected variance of the boundary values about some mean value, and their expected spatial smoothness (Thacker, 1988).

The second major scientific objective of this dissertation is thus the optimal estimation of all of the initial and boundary conditions necessary to integrate the open–ocean model forward in time, in order to fit sparse interior data.

It will be shown that estimating the error in the estimated dynamical fields in the presence of strong nonlinearity is possible. The full error covariance matrix for the control variables can be computed from the inverse of the Hessian even when the model dynamics are strongly nonlinear. This is a major new result as no previous assimilation studies using the adjoint method have attempted to compute full error covariances with a nonlinear dynamical model.

The second major new result is the successful estimation of the full set of necessary boundary conditions specified by Charney *et al.* (1950). It is found that the interior data are sensitive to the boundary vorticity and streamfunction, via advection in the prognostic equation for vorticity. The interior data are also strongly sensitive

to the boundary streamfunction due to the elliptic character of the Poisson equation for streamfunction. This latter effect is instantaneous. From a time–invariant first guess for the boundary conditions, ie. persistence, the adjoint method is able to create temporal variations in the boundary conditions so that the ensuing interior flow field matches the signals recorded in the data.

This dissertation is divided into two parts each of which uses a different set of control variables, that is independent model parameters that are varied in order to minimize a model/data misfit. In the first part of this study, the open–ocean boundary conditions are treated as known in the assimilation experiments, and the model is constructed in such a manner that the prescribed boundary conditions have minimal influence on the assimilation of data into the dynamical model. For this first part, the control variables are the initial conditions for vorticity. Chapter one describes the set–up of the simulated ocean, and presents several twin experiments where different prescriptions of the boundary conditions are used. The formalism to derive the error covariance matrix for the control variables from the inverse Hessian matrix of the cost function at its minimum is presented in chapter two. Error estimates for the vorticity initial conditions are calculated using two different methods that illustrate the effects of nonlinearity. As this is a major new result, the calculation of the error covariance matrix and its off–diagonal structure are explored in detail. The sensitivity of the observed velocities in the estimated flow to the vorticity initial conditions is also shown.

In the second part of the dissertation the boundary conditions for streamfunction and vorticity, as well as the initial conditions for vorticity, are used as control variables in the adjoint method. The number of control variables to be estimated is reduced by expanding the temporal behavior of each boundary value of streamfunction and vorticity in Fourier series. This expansion is presented in chapter three, along with the results of several twin experiments illustrating the dependence of the assimilation on the availability of *a priori* information about the boundary conditions.

Experiments are run with noise added to the observations, and to the first guess for the control variables. Objective mapping of a simulated streamfunction survey is used to construct a first guess for the control variables. These latter experiments test the ability of the adjoint method to reconstruct the flow field from more realistic knowledge.

In chapter four the quality of the estimated initial and boundary conditions is assessed by examining the residuals with the true values, and again by calculating the error covariance matrix from the inverse Hessian. The sensitivity of the model counterparts of the observations to perturbations in the estimated boundary and initial conditions as well as the means by which information is spread in time and space is discussed. Error maps are then estimated for the interior fields of streamfunction and vorticity, by a Jacobian transformation of the error covariance matrix for the boundary and initial conditions.

Details of the formulation of the adjoint method is presented in the appendix, starting from the general form and then deriving the full adjoint model for the finite-difference forward model. For the mathematical formulae throughout this dissertation, vectors are denoted by lowercase boldface characters and matrices are denoted by uppercase boldface characters.

Chapter 1

Estimating initial conditions

In this chapter the adjoint method is used to optimally estimate the vorticity initial conditions for a quasi–geostrophic model that minimize the misfit between model and data at later times. The simulated experiments presented here are designed to simulate the observing array from the SYNOP East project, which consisted of an array of current meters that spanned the Gulf Stream and most of the southern and northern recirculations. There was also an array of tomographic transceivers in the southern recirculation. Results from these observations can be found in Chester (1993).

The difficulties of implementing boundary conditions in open ocean modeling were discussed in the introduction. A simple first approach taken in this chapter is to specify the the values of streamfunction and vorticity on the boundaries before the assimilation, based upon any available information. The effect of the assumed boundary values on the interior flow field can be diminished by enlarging the width of the model domain in order that the edges of the domain are far from the observation sites. This is an impractical fix as the number of interior grid points increases with the square of the number of boundary points. For a jet–like flow over a long time period the boundaries would have to be a great distance from the observations, so the number of model variables to estimate would become quite large.

Also the model domain would become so broad that most of the interior would be unobservable from the observations. A somewhat better fix is to impose a sponge layer around the edges of the model domain, with the hope that this will diminish the influence of the assumed boundary conditions on the model/data misfit in the interior.

Tziperman & Thacker (1989) used the adjoint method to estimate the vorticity initial conditions for a barotropic quasi–geostrophic model of the subtropical gyre, from synthetic observations of streamfunction and vorticity. Their forward and adjoint model codes were used as a basis for the estimation experiments presented here. The model codes were modified to include periodic boundary conditions and observations of velocity.

The simulation of the Gulf Stream is first described, then follows a section on the cost function and the simulated observations. Details on the adjoint method, which involves quite elaborate mathematics, can be found in the appendix. Twin experiments are then presented, and their results show the effectiveness or otherwise of the assimilation scheme.

1.1 Modeling the Gulf Stream

The model used here to represent the ocean dynamics is the nonlinear barotropic conservation of vorticity on a β–plane with bottom friction and biharmonic friction (Pedlosky, 1979),

$$\frac{\partial \zeta}{\partial t} + J\left(\psi, \zeta\right) + \beta \frac{\partial \psi}{\partial x} = -\epsilon_b \zeta - \epsilon_h \nabla^4 \zeta$$

where

$$\zeta = \nabla^2 \psi.$$

These two equations will be referred to as the forward model. When space and time are discretized, the prognostic equation in finite–difference form is

$$\frac{\zeta_{i,j}^{t+1} - \zeta_{i,j}^t}{\Delta t} + J\left(\psi_{i,j}^t, \zeta_{i,j}^t\right) + \beta\left(\frac{\psi_{i+1,j}^t - \psi_{i-1,j}^t}{2\Delta x}\right) + \epsilon_b\zeta_{i,j}^t + \epsilon_h\nabla^4\zeta_{i,j}^t = 0 \qquad (1.1)$$

where the grid spacing, Δx and Δy, is 20 km, and the time step, Δt, is one hour. With this choice of discretization the prognostic equation is stable in time using the Euler–forward form of the time derivative. The standard nine–point Arakawa Jacobian and the five–point Laplacian are used in the discretized forms. The model domain is a zonally periodic 1,280 x 1,280 km square. Streamfunction, ψ_{ij}^t, and vorticity, ψ_{ij}^t, at each interior grid point and time–step are called the state variables.

Charney, Fjørtoft and von Neumann (1950) investigated the open boundary conditions that are appropriate to integrate this same model forward in time. They found that a sufficient set of boundary conditions are: vorticity at all interior points at the initial time, streamfunction at all boundary points at all time–steps and vorticity at all inflow points on the boundary at all time–steps (see also Bennett, 1992, chapter 8). Denoted the CFvN conditions, they hold when the boundary "is not an interface between one system and another. Instead, the boundary merely defines a sub–region of a single system." (Bennett, 1992). One of the main aims of this study is the estimation of the CFvN boundary conditions for a sub–region of the zonally periodic channel.

The Gulf Stream is modeled by a thin zonal jet that meanders and goes barotropically unstable over a period of 24 days. The streamfunction and vorticity fields are shown in figure 1.1. The model parameters used to create this simulated flow field are based upon the numerical experiments of Flierl et $al.$ (1987). The meandering is made more pronounced by setting β to zero for the experiments in this chapter and in chapter three.

The barotropic vorticity equation is clearly an oversimplification of the physics of the Gulf Stream. However it does enable one to construct a flow field that contains
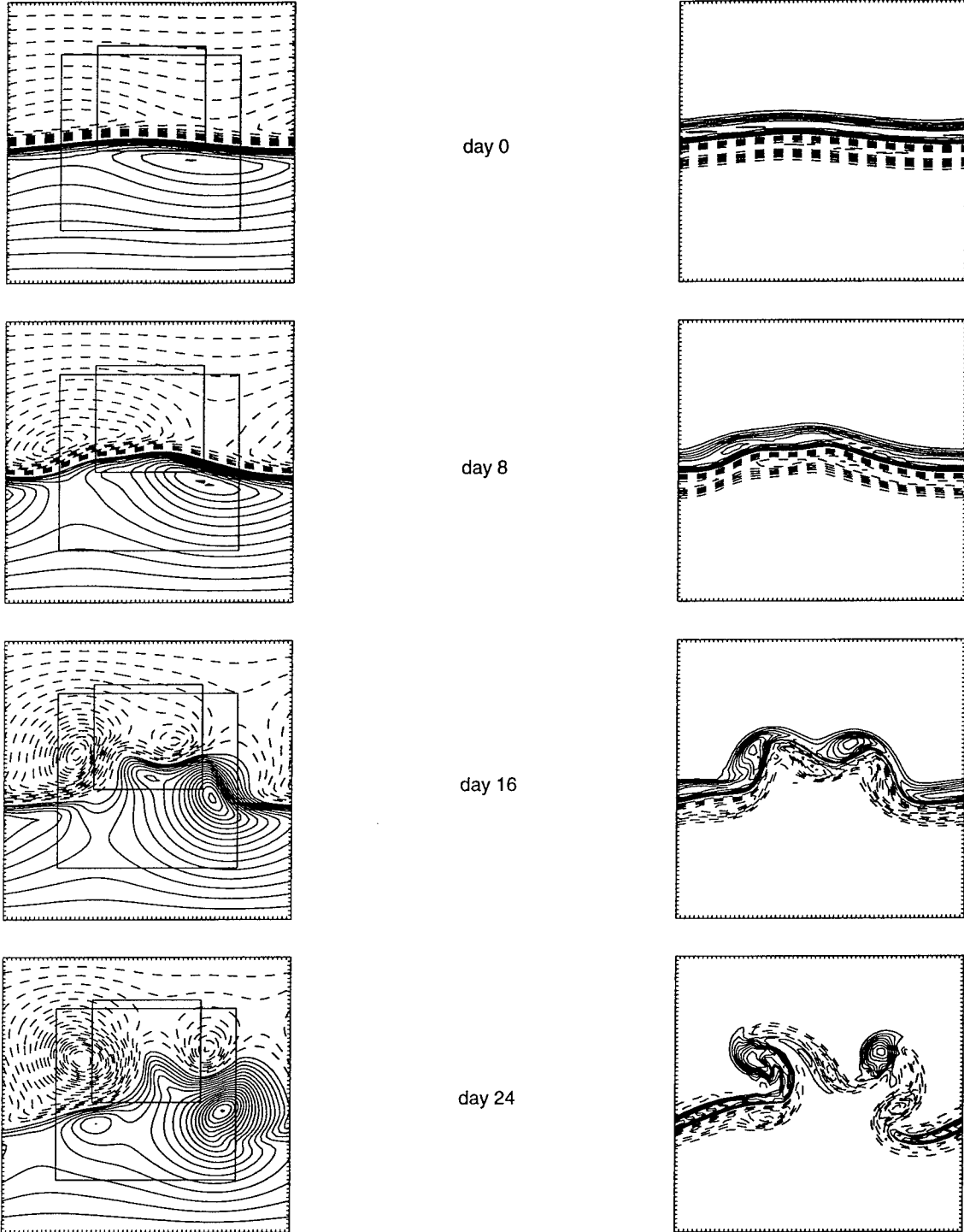
Figure 1.1: The evolution of the jet over 24 days, plotted are contours of (left) stream-function (C.I.=5000 m^2/s), and (right) vorticity (C.I.= 2×10^{-6} s^{-1}), every 8 days over the zonally periodic domain (1280 $km \times$ 1280 km, with a grid spacing of 20 km). The sub–domain boundaries used in the twin experiments are drawn on the streamfunction plots.

some of the principal features of the Gulf Stream using many fewer state variables than more complicated models. The nonlinearity in the barotropic vorticity equation is the strong advection of vorticity by the velocity field, which is regarded as a dominant dynamical feature of the Gulf Stream. The feature most obviously lacking is vertical variation. The barotropic component of the Gulf Stream increases after it leaves Cape Hatteras due to the northern and southern recirculation gyres (Hogg, 1992). Also, much of the variability in the region of the southern recirculation gyre is contained in the barotropic mode and the first and second baroclinic modes (Hua *et al.*, 1986, Richman *et al.*, 1976). For the assimilation of real instead of synthetic data, an adequate model for the Gulf Stream and its recirculations could be constructed using quasi–geostrophic dynamics in the barotropic and first few baroclinic modes, with the same assimilation procedure as is used here. The inclusion of vertical variability is a necessary next step for this line of research.

1.2   The cost function

By varying a vector of control variables, θ, the assimilation forces the forward model to create a flow field that agrees with the available data. The control variables may be any independent parameters of the model. The available data is organised as a vector, $\mathbf{d}$, which is related to the control variables by the sampling equation,

$$\mathbf{m}(\theta) + \mathbf{n} = \mathbf{d} \qquad (1.2)$$

where $\mathbf{m}(\theta)$ is the vector of model counterparts of the data, and $\mathbf{n}$ are the errors involved in representing $\mathbf{d}$ by $\mathbf{m}(\theta)$. One can also think of $\mathbf{m}(\theta)$ as the data created by the control variables, or the control vector mapped onto the data space,

The differences between the data and the model counterparts of the data should be reasonably small. This difference is expressed in a least squares form termed the

cost function,

$$J = \frac{1}{2} \sum_k \frac{(m_k(\theta) - d_k)^2}{\sigma_k^2} \qquad (1.3)$$

where d_k is the kth data point, $m_k(\theta)$ is the model counterpart of the kth data point, and σ_k^2 is the expected variance of the observational error in the kth data point, n_k. For real observations, the observational error is comprised of both the difference between the data and their true values due to instrument noise and sampling error, and the difference between the data and their model counterparts due to inadequacies in the model. The assimilation searches for the control variables, θ, that minimize J.

Equation (1.3) can be rewritten in matrix/vector form as

$$J = \frac{1}{2}(\mathbf{m}(\theta) - \mathbf{d})^T \mathbf{R}^{-1}(\mathbf{m}(\theta) - \mathbf{d}) \qquad (1.4)$$

where $\mathbf{R} \equiv < \mathbf{nn}^T >$ is the covariance matrix for the observational errors [1] , $\mathbf{n}$. It is a diagonal matrix with the σ_k^2 down the main diagonal. The vector of residuals, $\mathbf{m}(\theta) - \mathbf{d}$, is called the model/data misfit.

The observations to be used as data for the assimilation are of flow velocity from an array of simulated current meters at various points in the model domain. The eastward and northward components of flow velocity at grid point, (i, j), and time–step t are determined from the streamfunction using center–differences

$$u_{ij}^t = -\left(\frac{\partial \psi}{\partial y}\right)_{ij}^t \equiv \frac{(\psi_{i,j-1}^t - \psi_{i,j+1}^t)}{2\Delta y} \quad , \quad v_{ij}^t = \left(\frac{\partial \psi}{\partial x}\right)_{ij}^t \equiv \frac{(\psi_{i+1,j}^t - \psi_{i-1,j}^t)}{2\Delta x}$$

With this discretization, streamfunction, velocity and vorticity all occupy the same grid–points. Also there are observations of line–averaged flow velocity between two points, to simulate reciprocal travel–times from acoustic tomography. For a sound wave traveling between two acoustic transceivers in a fluid, the difference in travel time going in opposite directions is a measure of the integrated along–path fluid speed (see Chester, 1993, for details). Four simulated transceivers are placed at the points

---

[1]The delimiters $< \ldots >$ denote the expected value of a quantity over a large number of realizations

of a cross shape in the barotropic model domain. The mean zonal flow speed between the west transceiver, W, and the east transceiver, E, at time t, is given by

$$\tau_{WE}^t = -\frac{1}{L} \int_E^W \frac{\partial \psi^t}{\partial y} \Delta x \equiv \frac{1}{L} \sum_{i=i_W}^{i_E} \left(\frac{\psi_{i,j_W-1}^t - \psi_{i,j_W+1}^t}{2\Delta y} \right) \Delta x$$

and the mean meridional flow speed between the south transceiver, S, and the north transceiver, N, at time t, is given by

$$\tau_S^t = \frac{1}{L} \int_N^S \frac{\partial \psi^t}{\partial x} \Delta y \equiv \frac{1}{L} \sum_{i=i_S}^{i_N} \left(\frac{\psi_{i_S+1,j}^t - \psi_{i_S-1,j}^t}{2\Delta x} \right) \Delta y$$

where $L=200\ km$ is the transceiver separation.

The cost function is defined for N_v current meter observations and N_τ tomographic observations as

$$
\begin{aligned}
J &= \frac{1}{2N_v\sigma_v^2} \sum_{k=1}^{N_v} \left(\left[-\left(\frac{\partial \psi}{\partial y}\right)_{i_k,j_k}^{t_k} - u_{i_k,j_k}^{t_k} \right]^2 + \left[\left(\frac{\partial \psi}{\partial x}\right)_{i_k,j_k}^{t_k} - v_{i_k,j_k}^{t_k} \right]^2 \right) \\
&+ \frac{1}{2N_\tau\sigma_\tau^2} \sum_{k=1}^{N_\tau} \left(\left[-\frac{1}{L} \int_W^E \frac{\partial \psi^{t_k}}{\partial y} \Delta x - \tau_{EW}^{t_k} \right]^2 + \left[\frac{1}{L} \int_N^S \frac{\partial \psi^{t_k}}{\partial x} \Delta y - \tau_{SN}^{t_k} \right]^2 \right). \quad (1.5)
\end{aligned}
$$

where $\sigma_v \equiv 4 \times 10^{-2} m/s$ is the *a priori* estimate of the error in the velocity observations, and $\sigma_\tau \equiv 4 \times 10^{-2} m/s$ is the *a priori* estimate of the error in the tomographic observations. This choice of *a priori* error is taken from a rule of thumb that the error in a velocity observation is of the order of 5% of the total variability (Nelson Hogg, personal communication).

In this chapter the control variables are the vorticity initial conditions. The vorticity initial conditions are related to the model counterparts of the data (the spatial derivatives of streamfunction at i_k, j_k, t_k) through the forward model, equation (1.1). When the assimilation is performed so as to minimize the cost function, in theory the cost function could be reduced to zero if the model is perfectly consistent with the data, and the data are noise-free. However, if there are errors in the data or in the model, the aim is to minize the cost function only to the level at which the residuals in (1.5) are of the same order as the observational error. If the errors are

zero, everything is perfect and the final value of J will be zero. The minimization is performed using the adjoint method, details of which are given in the appendix.

As well as the model/data misfit, other terms may be included in the cost function that penalize the mean–square of residuals. Knowledge of the first–order statistics of the control variables can be used in the cost function to improve the minimization. That is, one usually has an *a priori* estimate of the expected value or mean, θ_0, and the covariance of this expected value about the unknown true values of the control variables, $\mathbf{R}_{\theta\theta}$, ie.

$$\mathbf{R}_{\theta\theta} = <(\theta - \theta_0)(\theta - \theta_0)^T>$$

Then the least–squares term

$$\frac{1}{2N_\theta}(\theta - \theta_0)^T \mathbf{R}_{\theta\theta}^{-1}(\theta - \theta_0)$$

is added to the cost function, J, where N_θ is the number of control variables. If the mean and variance of the control variables is totally unknown, one would give the control variables infinite *a priori* variance reflecting the fact that the control variables can assume any value. In this case the above least–squares term is zero. In oceanography one usually has some idea of the first–order statistics of the dynamical variables being used as control variables.

For each experiment in this study, θ_0 is set as the first guess for the control variables, and $\mathbf{R}_{\theta\theta}$ is set as a diagonal matrix with the expected variances of each control variable down the main diagonal. For the experiments presented in this chapter the expected variance of the vorticity initial conditions is determined by averaging over the true flow field. A mean measure of variance is chosen that is the same for all of the vorticity initial conditions. For the experiments of chapter three, where the boundary conditions for streamfunction and vorticity are included in the control vector, the choice of $\mathbf{R}_{\theta\theta}$ will be seen to require more careful consideration.

Also added to the cost function is a mean–square term penalizing the Laplacian of the vorticity initial conditions (the control variables in this chapter), ie.

$$\frac{1}{2N_\theta} \sum_{ij} (\nabla^2 \zeta_{ij}^0)^2 s^{-2}$$

where s is the *a priori* expected value of the mean–square Laplacian of the vorticity field, here evaluated from the true flow field. The effect of minimizing this term is to enforce spatial smoothness (see Thacker, 1988, for more details). Rewriting this smoothness term in matrix/vector form, it can be added to the previous size term, to produce an *a priori* covariance matrix for the control vector, $\mathbf{P_0}$, defined in the cost function by

$$(\theta - \theta_0)^T \mathbf{P_0}^{-1} (\theta - \theta_0) = (\theta - \theta_0)^T \left[\mathbf{R}_{\theta\theta}^{-1} + \mathbf{L}^T \mathbf{S}^{-1} \mathbf{L} \right] (\theta - \theta_0)$$

where $\mathbf{L}$ is the Laplacian operator in matrix form and $\mathbf{S}$ is a diagonal matrix with the value of s along the diagonal.

Thus the cost function consists of three parts: size, smoothness and model/data misfit. In a successful minimization these should all be reduced to order one. The rms variances selected for the weights in the size and smoothness terms, are determined from the true flow field. For real data, one could put bounds on the size and smoothness of streamfunction and potential vorticity, by invoking quasigeostrophy or by studying output from a general circulation model.

1.3 Twin experiments

The objective is now to reconstruct the true ocean state from sparse observations using some assimilation scheme. For the purpose of assessing the success of the assimilation scheme, and to study the spread of information from the observations into regions devoid of data, the twin experiment approach is used here (Ghil & Malanotte–Rizzoli, 1991).

In an identical twin experiment, a control model run provides a simulated ocean state as a true reference ocean, from which simulated observations are taken. The model is then started from some false initial conditions (that are significantly different from the true initial conditions) and integrated forward in time. An assimilation scheme is used to force the so-called false flow field towards the true flow field using the observations. The success of the assimilation scheme in rendering the false flow field to be more like the true flow field can be assessed. Malanotte–Rizzoli and Young (1992), used a primitive–equation model of the Gulf Stream, taking simulated observations from array configurations similar to those used in the SYNOP experiment. Their sequential estimation scheme was able to force the model from a false time–dependent state towards the true state from which the observations had been taken.

In this study so–called fraternal twin experiments are performed, as distinct from identical twin experiments. In identical twin experiments the model used to assimilate data from the true flow field, has the same model parameters as the model used to create the true flow field. That is, domain size, friction, etc. are kept the same. In fraternal twin experiments the model parameters used for the assimilation differ in some way from the those of the true flow field. In the following experiments the domain size of the model used for the assimilation is a smaller sub–domain of the true flow field.

When the domain size of the assimilation is kept as large as the domain size of the true flow field domain, there are a large of number of control variables (initial conditions of vorticity at every interior grid point) and the assimilation runs slowly and requires a lot of memory. Moreover, for an observing array that does not have great spatial coverage relative to the size of the true flow field domain, much of the domain can not be well estimated from the data. In the parlance of control theory, those parts of the domain where the vorticity initial conditions are not well determined from the data are said to be unobservable. The model domain used for the assimilation in the various twin experiments to be presented here, is constructed so as

to enclose the observing array and be wide enough to allow the spread of information from the observations.

Starting from some first guess for the vorticity initial conditions, the adjoint method is used to optimally estimate the vorticity initial conditions that, when integrated forward in time, best fit the observations by minimizing the cost function. The observations from the true flow field are taken only from the observing array in the interior so the boundary values of streamfunction and vorticity are not known. The approach taken in this chapter is to specify the values of streamfunction and vorticity on the boundary by making some *a priori* assumptions about the expected flow field in the region. Moore (1991) estimated vorticity initial conditions from real data using the adjoint method for a quasi–geostrophic model of the Gulf Stream, keeping the open–ocean boundary conditions fixed at values taken from a larger scale model combined with smoothed data. The level of assumed prior knowledge of the boundary conditions for the experiments presented here is much lower than in Moore (1991).

A sponge layer is introduced over several grid points from the boundary into the interior. In the sponge layer the bottom friction coefficient, ϵ_b, is ramped in space such that it goes from a low value in the interior to a high value at the boundary over the space of a few grid points. The purpose of the sponge layer is to decelerate the flow in a layer near the boundaries. It is hoped that this will have the same effect as removing the boundaries of the sub–domain to a greater distance from the observing array, and thus reduce the influence of the specified boundary values on the interior flow field seen by the observing array.

It is desirable that the estimation of the vorticity initial conditions be influenced as much as possible by the observations and less by the specified boundary conditions for streamfunction and vorticity. From the forward model equations, (1.1), one can see that there are three processes by which the boundary conditions may in-

27

fluence the interior fields: (i) advection, (ii) wave propagation, and (iii) the elliptic character of the Poisson equation for streamfunction.

The sponge layer reduces the magnitude of advection in the vicinity of the boundary, so that for the first process the influence of the boundary values of streamfunction and vorticity on the observations of velocity in the interior is reduced. For a short enough assimilation period, the boundary streamfunction and vorticity will not be advected through the observing array, but obviously when the model is integrated long enough all of the interior points will feel the effect of the specified boundary conditions through advection.

For the experiments presented here, beta is deliberately set to zero so that the meandering of the jet is more pronounced (see Flierl *et al*, 1987). Thus there are no planetary waves to spread information through the domain. Using actual data from SYNOP East one would include beta in the model dynamics. Although compared to advection in the vicinity of the jet, planetary waves would probably have little importance in the spread of information.

For the third process, at any time–step the value of streamfunction at any interior point is dependent upon the local value of vorticity and the boundary values of streamfunction (see Morse & Feshbach, p. 696, 1953). Thus perturbations of the boundary values of streamfunction instantaneously affect the streamfunction field throughout the interior. This process, or mechanism, will be seen to be important in the estimation of time–dependent boundary streamfunction in chapters three and four. For the experiments in this chapter where boundary streamfunction is specified ahead of time, and velocity observations are used, this third process does not have much impact on the estimation of the optimal vorticity initial conditions. If the available data were interior streamfunction observations the boundary streamfunction would strongly influence the model counterparts of the observations via this process.

1.4 Results

For the first twin experiment, case A1, an array of thirteen current meters are deployed that span the central part of the jet shown in figure 1.1. This array type was chosen as it has a similar configuration to the central and eastern arrays in the SYNOP project. The model domain for the assimilation covers an 800 x 800 km square that encloses the current meter array. The data consists of eastward velocity, u, and northward velocity, v, recorded at each of the thirteen current meter locations every two days over a 24 day period.

For this case it is assumed that nothing is known about the background values of streamfunction and vorticity in the model domain and outside of the model domain except that there is some zonal character to the flow. Thus streamfunction and vorticity are arbitrarily set to zero on the northern and southern boundaries for all time, and are made periodic on the eastern and western boundaries. The first guess for the vorticity initial conditions is zero at all grid points at the start of the assimilation.

In figure 1.2 snapshots are shown of the streamfunction for the true flow field shown over the sub–domain used for the assimilation (this is a subplot of figure 1.1), and for the streamfunction resulting from the optimally estimated vorticity initial conditions, every eight days. The large amplitude signals in the observations are quite well estimated in the false flow field. The location of the jet as it meanders, is well determined in the vicinity of the observing array. However low amplitude signals in the observations are not well estimated. The flow to the north and south of the jet in the estimated flow field does not resemble the flow in the true flow field.

The assimilation shows some skill at estimating the spatial structure of the flow field downstream of the observing array at later times. This is because the flow that passes through the array is well estimated, and in this highly advective flow, the influence is carried away downstream. In the regions of the false model domain that are devoid of data, the estimates of streamfunction and vorticity produced by the
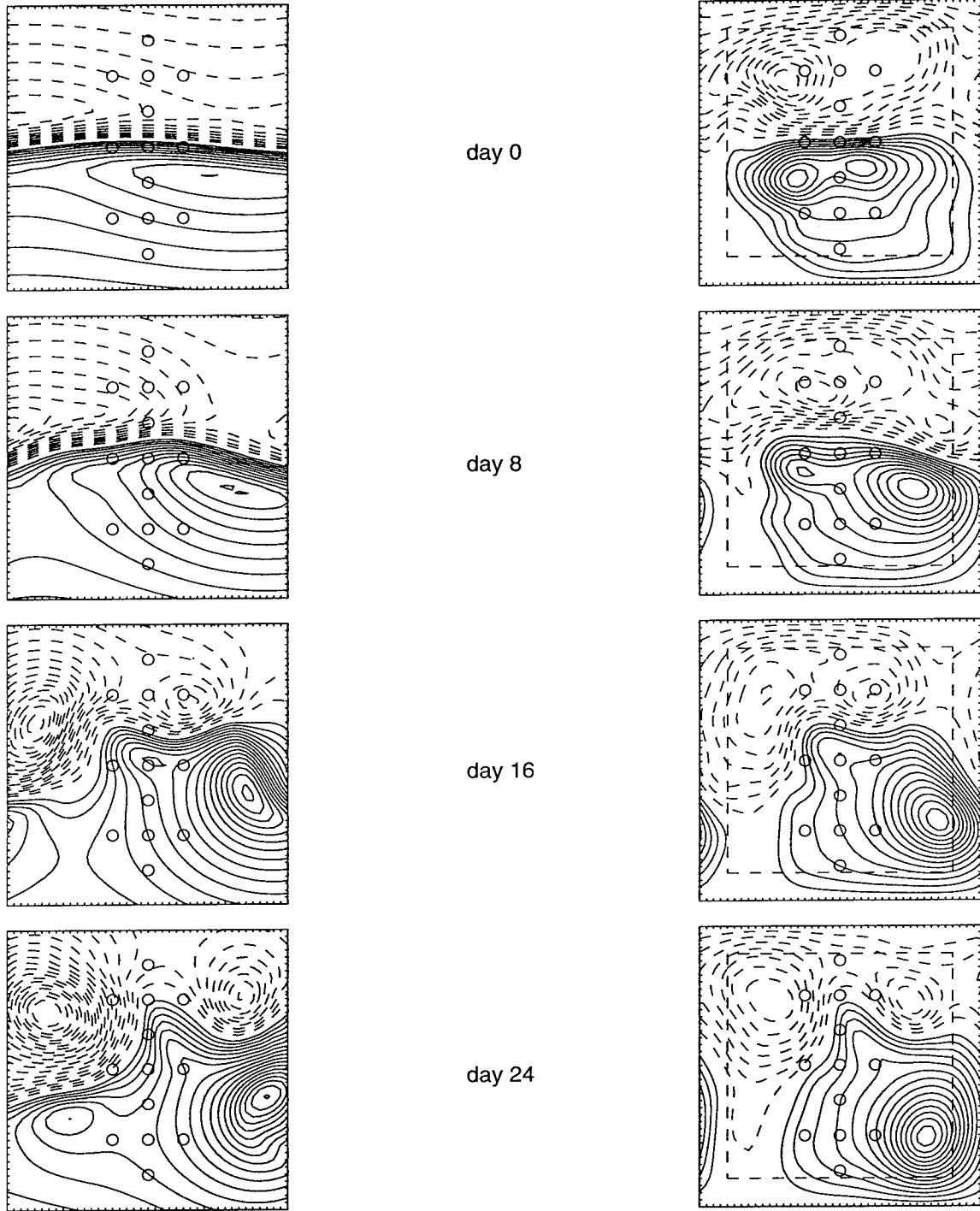
29

Figure 1.2: Streamfunction every two days for (left) the true flow field over the smaller domain, (right) Case A1 : the estimated flow field, the dashed line marks the sponge layer. (C.I.=5000 m²/s)

assimilation are strongly influenced by the specified boundary conditions. The pairs of eddies seen in the true flow field at later times (bottom frames of figure 1.1) can not be well estimated in the false flow field because the imposed boundary conditions of the sub–domain are inconsistent with their corresponding values in the true flow field.

For case B1 an array of five current meters in a cross shape are deployed to the north of the jet. They have the same locations as the top five current meters in the array used in case A1. There are acoustic tomography transceivers at the four outer points of the cross . With this observing array design, the current meters and the tomography can be readily compared within the context of the assimilation. The data consists of u and v recorded at the five current meter locations every two days over a 24 day period, and τ_{WE} and τ_{SN} at the same times. The true flow field over the sub–domain used for this case is shown on the left of figure 1.3. Being situated to the north of the jet, the array does not observe the jet until it swings through as a meander from days 16 to 24.

The sub–domain for this case is 25 by 25 grid points, covering an area of 480 x 480 km. As in case A1, in the absence of any other knowledge, save that there is some zonal character to the flow, the boundary conditions for streamfunction and vorticity are set to zero on the northern and southern edges of the model domain, and are made periodic in the east–west direction, for all time–steps. The first guess for the vorticity initial conditions at the start of the assimilation is zero.

This observing array configuration and sub–domain size are used for the remainder of the twin experiments in this study. The choice of a sub–domain that does not include the jet was motivated by the intention of eventually calculating eddy potential vorticity flux divergences in the southern recirculation gyre. The real data that would be used in an assimilation to calculate the potential vorticity fields, would come from the lower part of the SYNOP East array that is situated in the recircula-

tion. Also, the acoustic tomographic transceivers are situated only in the lower part of the SYNOP East array (Chester, 1993).

In figure 1.3 snapshots are shown of the streamfunction for the true flow field and for the optimally estimated false flow field at eight day intervals. It is apparent that the flow field is not estimated well here. Setting streamfunction and vorticity to zero on the southern boundary for all time is inconsistent with the location of the jet in the true flow field. The assimilation puts an eddy in the sponge layer to the southwest that evolves in time to become the meander event that is observed at later times.

The true and estimated vorticity fields for case B1 are shown in figure 1.4. The lack of resemblance between the true and estimated flow fields is more obvious here, especially at the initial time. By its dynamical nature, vorticity has a shorter length–scale of variability than streamfunction. Thus more convoluted spatial structure is allowed in the estimated vorticity fields. The sponge layer can be seen to be damping the vorticity near the boundaries.

In figure 1.5 the velocity time series are displayed from each of the current meters and from the tomography, for the true flow field and the assimilated flow field for case B1. One can see that the tomographic measurement is indeed an average over the current meters in its path. The strongest signal in the data seen in figure 1.5 is the meander event between day 16 and day 24. This is the best estimated feature of the true flow field. The low amplitude flow field observed at earlier times is not well estimated from the data.

As can be seen in figure 1.3, the estimated initial conditions for streamfunction look quite different from the true conditions. The uniform westward flow over the observing array in the true flow field at the initial time is not well constructed in the estimated flow field. Apart from the imposed boundary conditions, the estimated flow does not resemble the true flow at the initial time because there are no observations at the initial time (the first observations are at day 1).
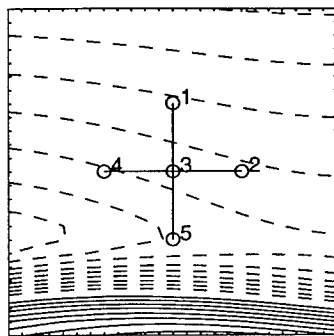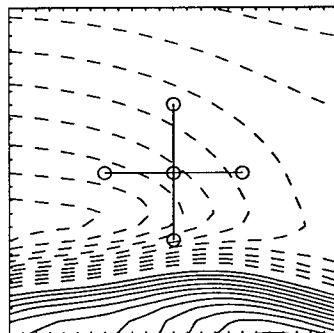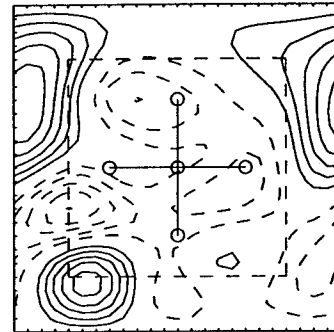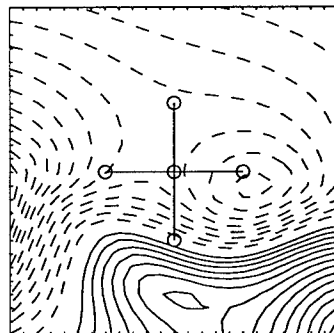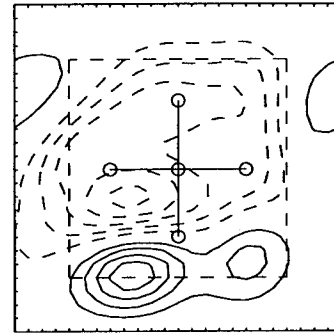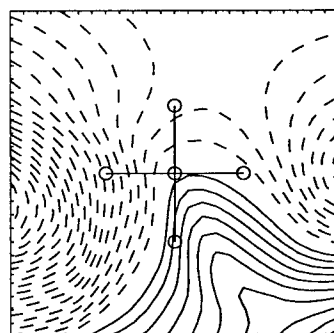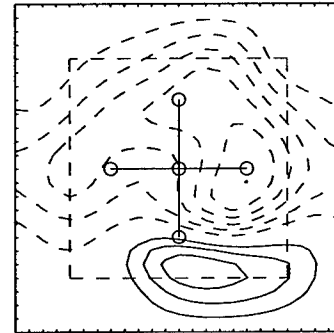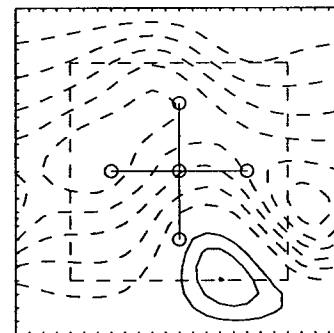
Figure 1.3: Streamfunction every two days for (left) the true flow field over the smaller domain, (right) Case B1: the estimated flow field, the dashed line marks the sponge layer. (C.I.=5000 m^2/s)
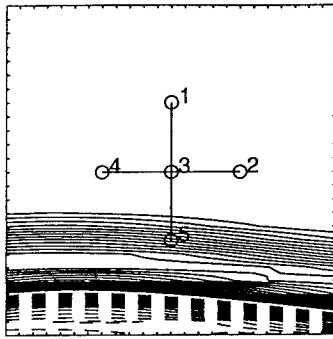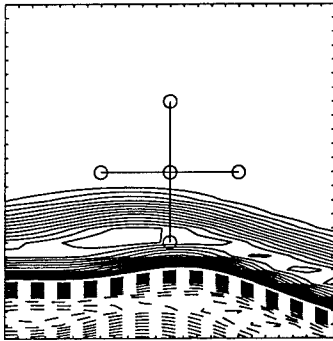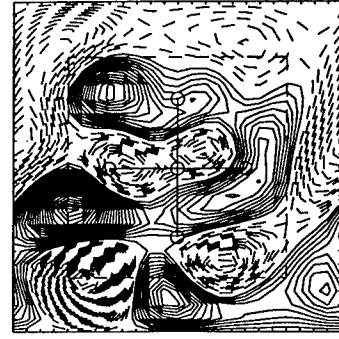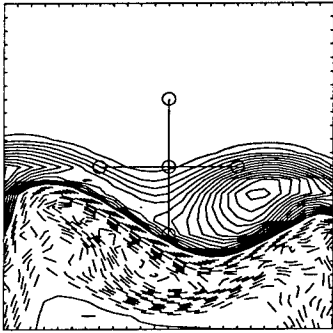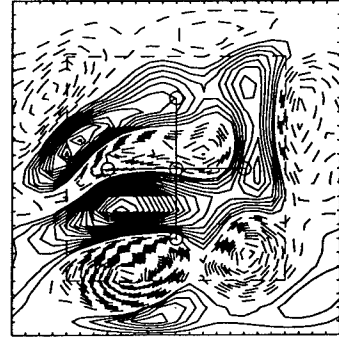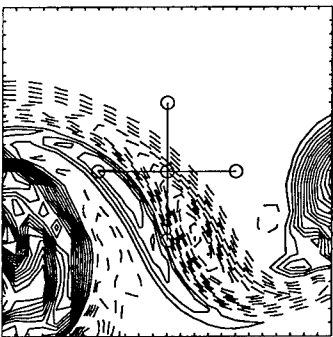
Figure 1.4: Vorticity every two days for (left) the true flow field over the smaller domain, (right) Case B1: the estimated flow field, the dashed line marks the sponge layer. (C.I.= $1 \times 10^{-6} \ s^{-1}$)
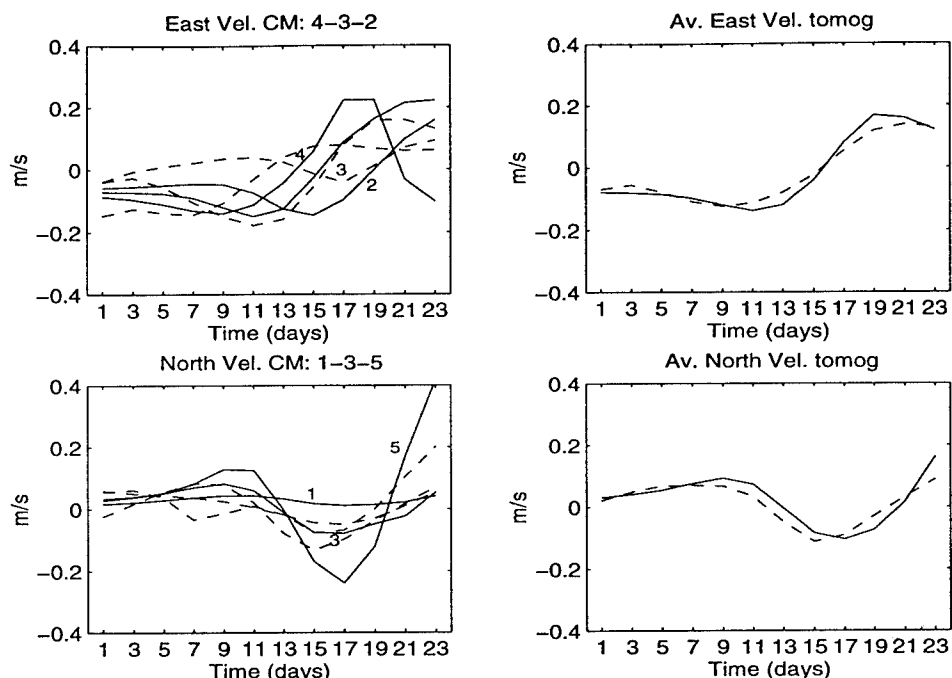
Figure 1.5:   Time series of velocities observed by current meters (left), and tomography (right). True velocities are solid, estimated velocities from case B1 are dashed. The *a priori* observational error is 4 *cm/s*.

Note that the velocity residuals for the optimally estimated flow field are some-what larger than the *a priori* error for the velocity observations, that is, the difference between the solid and dashed curves in figure 1.5 is generally greater than 0.04 *m/sec*. Because the residuals cannot be reduced to the level of the observational error, the model used for this case is assessed as being inconsistent with the observations from the true flow field.

Setting streamfunction and vorticity to zero at all times on the northern and southern boundaries is not a good choice if it is known that there is a meandering jet somewhere to the south. A more informed choice for the boundary values could be made. Case C1 is the same as case B1 but with streamfunction and vorticity on the southern boundary set to *a priori* estimates of their mean values from the true model. This is, in effect, a statement that there is a zonal character to the flow, and that there is a net eastward transport between the northern and southern boundaries.

The true and estimated streamfunction fields are shown in figure 1.6. It is apparent that the assimilation does not do much better with this model configuration. The meander event is again estimated quite well, but the flow field at earlier times is not estimated well in regions far from the array. A net eastward transport is inconsistent with the broad westward flow seen in the true flow field at early times. Also setting streamfunction to any sort of constant on the southern boundary of the sub-domain is not a good choice because in the true flow field the flow crosses this line.

Case D1 is a check that the assimilation scheme performs satisfactorily when the model is made perfectly consistent with the data. The same false model configuration is used as in cases B1 and C1, except that the boundary values of streamfunction and vorticity on all four edges are taken directly from the true flow field, keeping all of their spatial and temporal variation. Not surprisingly this assimilation does best of all, as can be seen in figure 1.7. Note that for this case the CFvN boundary conditions are overspecified in that vorticity is prescribed at outflow boundary points in the forward model integration, so that formally the forward model is ill-posed. This is not a problem as the prescribed vorticity on the boundary is consistent with the vorticity being advected to the boundary from the interior.

The value of the cost function as the iterations of the forward and adjoint models proceed (see appendix) is shown in figure 1.8. The differences among the specified boundary conditions for the twin experiments is summarized in table 1.1. One can see convergence to the minimum for each of the cases. When further iterations do not reduce the value of the cost function significantly, the minimization process stops. A successful minimization is one for which the model/data misfit is reduced to the order of the observational error, at which point the cost function is of order one. Only in cases A1 and D1 is the cost function successfully minimized. Case A1 does better than cases B1 or C1 because its observing array covers the jet at all observing times. The estimated vorticity initial conditions for case A1 can well estimate the flow at

36
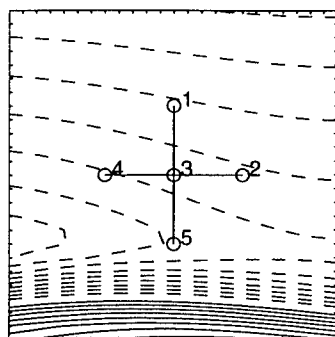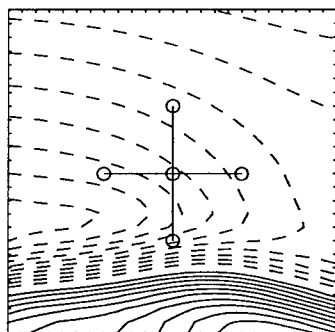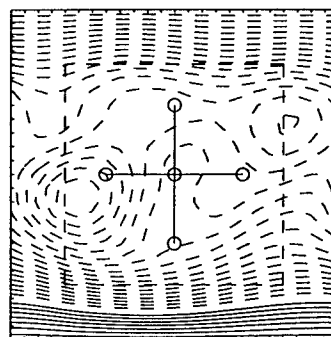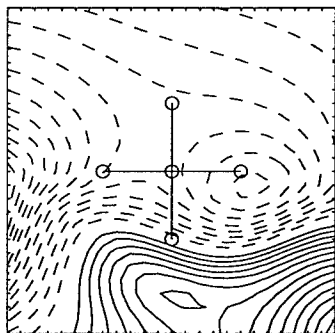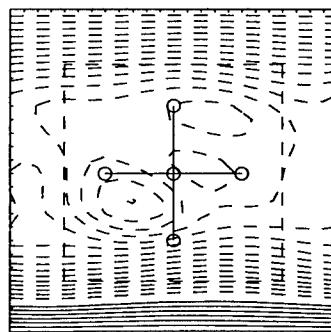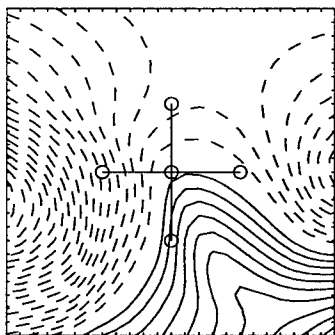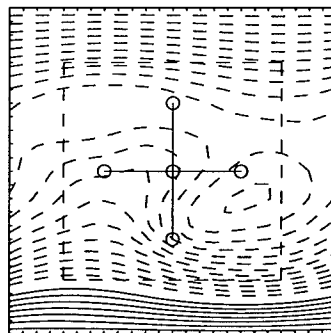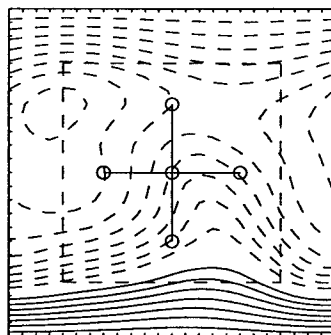
Figure 1.6: Same as figure 1.3 but for case C1 where streamfunction and vorticity on the northern and southern boundaries are kept at their mean values from the true flow field.
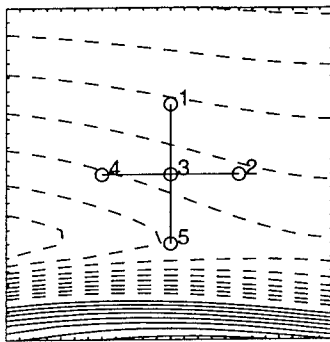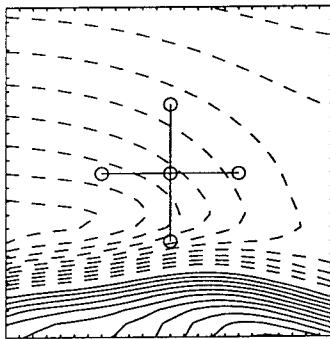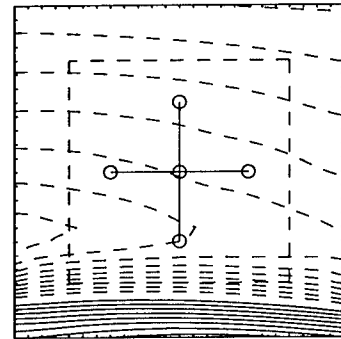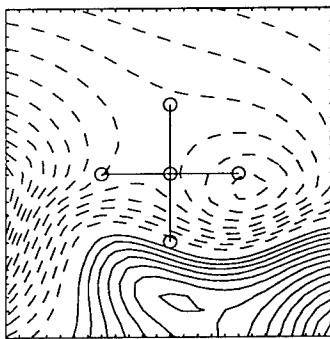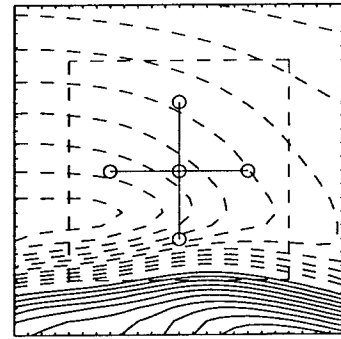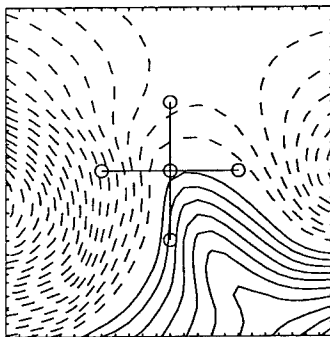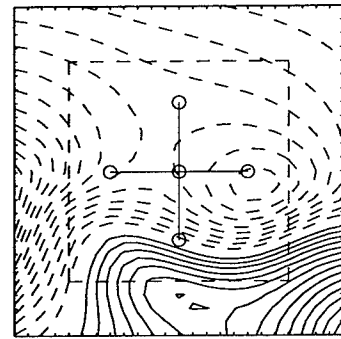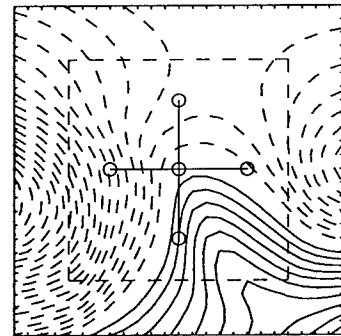
Figure 1.7: Same as figures 1.3 and 1.6 but for case D1 where streamfunction and vorticity on all boundaries keep their true values.
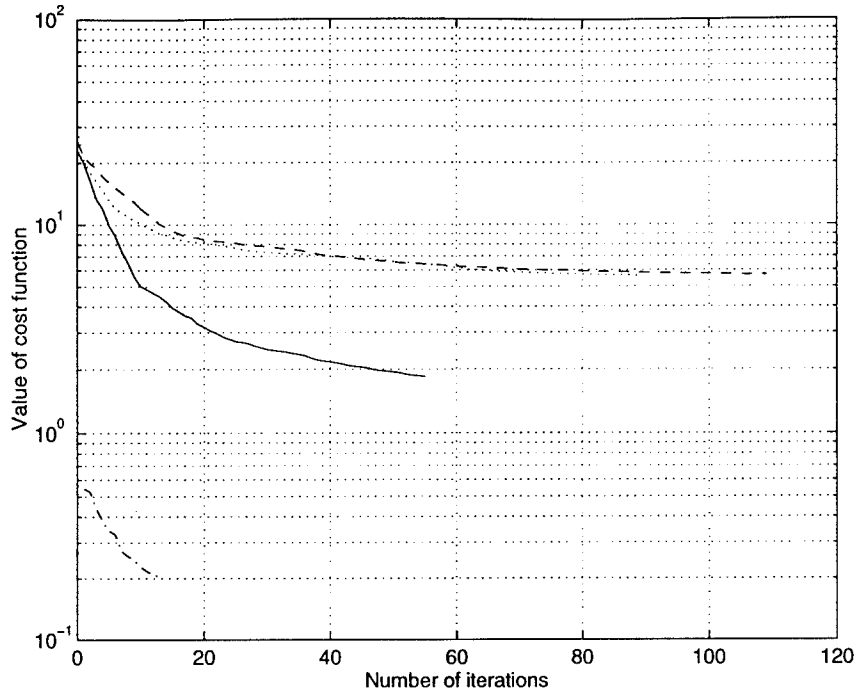
Figure 1.8: Value of cost function vs. iteration for each case: A1 (solid), B1 (dash), C1 (dot), D1 (dotdash).

early times, whereas in cases B1 and C1 the vorticity initial conditions are varied so as to reconstruct the meander event at later times.

Cases B1, C1 and D1, differ only in the choice of boundary conditions; the cost function, the data and the dynamics stay the same. It is apparent from the results of these experiments that the model/data misfit is strongly sensitive to the specified boundary conditions. The inclusion of a sponge layer in cases A1, B1 and C1 does

Experiment	Specified Boundary Conditions
A1	zero at NS, periodic at EW
B1	zero at NS, periodic at EW
C1	mean values from true field at NS, periodic at EW
D1	true values

Table 1.1: The specified boundary conditions for streamfunction and vorticity for each twin experiment.

39

not adequately diminish the influence of the specified boundary conditions on the model/data misfit. One could attempt to specify time–dependent boundary conditions that are more similar to the true boundary conditions. However the intention here is to estimate streamfunction and vorticity fields from available data only, using the dynamics to spread the influence of the data in time and space.

In the true flow field, the fluid in the jet that is observed at day 16, with an average speed of 50 cm/sec, was 700 kilometers (35 grid points) away to the west at day 0. The 480 km x 480 km sub–domain is too small to allow such large distances of fluid travel, over the duration of the assimilation. The results show that a strong signal such as the meander observed by the array at later times is fairly well estimated, but the meander is forced by the specified boundary conditions to be contained within the sub–domain at earlier times. The presence of the meander in the sub–domain at early times is inconsistent with the observed velocities at early times, thus deteriorating the model/data misfit.

Thus it is not fruitful to try to spread information in space and time from the observations, when the specified boundary conditions are having such an adverse effect. The aim is to construct a flow field from the observations that is large enough to capture the energetic scales of motion, while being adequately controlled by the data. Eventually much longer assimilation time periods than are used here will be needed to study the real flow field. It is impractical to lengthen the time periods used in cases A1, B1 and C1 as already the the specified boundary conditions are adversely affecting the model/data misfit for only a 24 day assimilation. For longer periods, where there are many energetic features in the flow, it is necessary to find a better way of treating the open boundary conditions.

Chapter 2

Uncertainty of the fit to data

After a model has been fit to data it is desirable to assess the quality of the fit, that is to make some estimate of the error so as to know what level of confidence to have in the estimates. For what follows it is assumed that one is at the stage of having found the minimum of the cost function with respect to a vector of control variables, and that one is in possession of the gradient of the cost function with respect to the control variables at the minimum.

For a linear model the error covariance matrix of the estimated control variables is given by the inverse of the Hessian matrix of the cost function with respect to the control variables. For a nonlinear model, the errors are also given by the inverse Hessian as long as the cost function approximates a quadratic at the minimum. A separate problem associated with nonlinearity is that the minimum might not be a global minimum.

Thacker (1989) illustrated the equivalence between the inverse Hessian and the error covariance of the control variables, by placing the minimization of the cost function in the probabalistic context of maximum likelihood theory. Here the equivalence is more clearly shown by looking at the minimization of the cost function in terms of the Gauss–Markov theorem.

The importance of the Hessian in the minimization of the cost function is then presented. Two different methods of computing the Hessian are presented, and some error covariance maps for the estimated vorticity initial conditions are shown. Measures of the sensitivity of the model counterparts of the data to perturbations in the estimated vorticity initial conditions are then shown.

In Thacker (1989) the evaluation of the error covariance matrix from the inverse Hessian was presented for weakly nonlinear dynamics. Furthermore, the large size of the Hessian for most oceanographic problem has deterred people from calculating the full error covariance matrix from the inverse Hessian, and previous studies have only calculated the main diagonal elements of the error covariance matrix using finite–differences (Schiller, 1995; Tziperman & Thacker, 1989). Marotzke & Wunsch (1993) discuss the estimation of uncertainties from main diagonal elements of the Hessian using finite–differences for a nonlinear ocean model, and point to the desirability of knowledge of the covariances between control variables. Here for the first time the estimation of the full error covariance matrix from the inverse Hessian when the model dynamics are strongly nonlinear is investigated.

2.1 The Gauss–Markov approach

The minimization of the least–squares cost function, described in section 1.2, may be investigated using the Gauss–Markov theorem (Liebelt, 1967).

The Gauss–Markov approach is as follows: To make an estimate of the control vector, denoted $\hat{\theta}$, that is as close as possible to the unknown true control vector, θ, the $\hat{\theta}$ is sought that minimizes the variance,

$$\hat{\mathbf{P}} = < (\hat{\theta} - \theta)(\hat{\theta} - \theta)^T >, \qquad (2.1)$$

given observations, $\mathbf{d}$, that are related to the control variables by the sampling equation (1.2).

To make the distinction between $\mathbf{P}_0$ and $\widehat{\mathbf{P}}$ clear,

$\boldsymbol{\theta}$ is the unknown true values of the control variables

$\boldsymbol{\theta}_0$ is an *a priori* guess of their expected value

$\hat{\boldsymbol{\theta}}$ is an estimate of the true values using the data $\mathbf{d}$

$\mathbf{P}_0$ is an *a priori* guess of the dispersion of $\boldsymbol{\theta}$ about $\boldsymbol{\theta}_0$

$\widehat{\mathbf{P}}$ is the dispersion of the estimates $\hat{\boldsymbol{\theta}}$ about the true values $\boldsymbol{\theta}$

An explicit expression for the $\hat{\boldsymbol{\theta}}$ that minimize $\widehat{\mathbf{P}}$ is obtained by substituting the form

$$\hat{\boldsymbol{\theta}} = \boldsymbol{\theta}_0 + \mathbf{B}(\mathbf{d} - \mathbf{m}(\boldsymbol{\theta}_0))$$

into (2.1), and solving for the unknown matrix operator, $\mathbf{B}$. Using the sampling equation (1.2) and assuming that the data noise, $\mathbf{n}$, is uncorrelated with the control variables, $\boldsymbol{\theta}$, ie. that $< \mathbf{n}\boldsymbol{\theta}^T > = 0$, we get

$$\widehat{\mathbf{P}} = < (\mathbf{B}[\mathbf{m}(\boldsymbol{\theta}) - \mathbf{m}(\boldsymbol{\theta}_0) + \mathbf{n}] - [\boldsymbol{\theta} - \boldsymbol{\theta}_0])(\mathbf{B}[\mathbf{m}(\boldsymbol{\theta}) - \mathbf{m}(\boldsymbol{\theta}_0) + \mathbf{n}] - [\boldsymbol{\theta} - \boldsymbol{\theta}_0])^T > . \quad (2.2)$$

Assuming that the *a priori* guess for the control variables, $\boldsymbol{\theta}_0$, is sufficiently close to the true control variables, $\boldsymbol{\theta}$, such that $\mathbf{m}(\boldsymbol{\theta})$ is linear in the neighbourhood of $\mathbf{m}(\boldsymbol{\theta})$, then

$$\mathbf{m}(\boldsymbol{\theta}) - \mathbf{m}(\boldsymbol{\theta}_0) = \frac{\partial \mathbf{m}}{\partial \boldsymbol{\theta}}[\boldsymbol{\theta} - \boldsymbol{\theta}_0]$$

and (2.2) becomes

$$\widehat{\mathbf{P}} = \mathbf{B}\left[\frac{\partial \mathbf{m}}{\partial \boldsymbol{\theta}}\mathbf{P}_0\left(\frac{\partial \mathbf{m}}{\partial \boldsymbol{\theta}}\right)^T + \mathbf{R}\right]\mathbf{B}^T - \mathbf{B}\frac{\partial \mathbf{m}}{\partial \boldsymbol{\theta}}\mathbf{P}_0 - \mathbf{P}_0\left(\frac{\partial \mathbf{m}}{\partial \boldsymbol{\theta}}\right)^T\mathbf{B}^T + \mathbf{P}_0$$

which is a quadratic matrix equation in terms of $\mathbf{B}$ that can be written as [1] ,

$$\widehat{\mathbf{P}} = \left[\mathbf{B} - \mathbf{P}_0\left(\frac{\partial \mathbf{m}}{\partial \boldsymbol{\theta}}\right)^T\mathbf{G}^{-1}\right]\mathbf{G}\left[\mathbf{B} - \mathbf{P}_0\left(\frac{\partial \mathbf{m}}{\partial \boldsymbol{\theta}}\right)^T\mathbf{G}^{-1}\right]^T - \mathbf{P}_0\left(\frac{\partial \mathbf{m}}{\partial \boldsymbol{\theta}}\right)^T\mathbf{G}^{-1}\frac{\partial \mathbf{m}}{\partial \boldsymbol{\theta}}\mathbf{P}_0 + \mathbf{P}_0$$

$$(2.3)$$

---

[1] For conformable matrices X, P and Q,
$XPX^T - QX^T - XQ^T = (X - QP^{-1})P(X - QP^{-1})^T - QP^{-1}Q^T.$

43

where $\mathbf{G} \equiv \frac{\partial \mathbf{m}}{\partial \theta} \mathbf{P}_0 \left(\frac{\partial \mathbf{m}}{\partial \theta} \right)^T + \mathbf{R}$. The first term on the right–hand side of (2.3) is positive–definite since $\mathbf{P}_0$ and $\mathbf{R}$ and therefore $\mathbf{G}$ are positive–definite. Hence $\widehat{\mathbf{P}}$ can be minimized with respect to $\mathbf{B}$ when

$$
\begin{aligned}
\mathbf{B} &= \mathbf{P}_0 \left(\frac{\partial \mathbf{m}}{\partial \theta} \right)^T \mathbf{G}^{-1} \\
&= \mathbf{P}_0 \left(\frac{\partial \mathbf{m}}{\partial \theta} \right)^T \left[\frac{\partial \mathbf{m}}{\partial \theta} \mathbf{P}_0 \left(\frac{\partial \mathbf{m}}{\partial \theta} \right)^T + \mathbf{R} \right]^{-1}
\end{aligned}
$$

Hence from (2.3)

$$
\begin{aligned}
\widehat{\mathbf{P}} &= \mathbf{P}_0 - \mathbf{P}_0 \left(\frac{\partial \mathbf{m}}{\partial \theta} \right)^T \left[\frac{\partial \mathbf{m}}{\partial \theta} \mathbf{P}_0 \left(\frac{\partial \mathbf{m}}{\partial \theta} \right)^T + \mathbf{R} \right]^{-1} \frac{\partial \mathbf{m}}{\partial \theta} \mathbf{P}_0 \\
&= \left[\mathbf{P}_0^{-1} + \left(\frac{\partial \mathbf{m}}{\partial \theta} \right)^T \mathbf{R}^{-1} \frac{\partial \mathbf{m}}{\partial \theta} \right]^{-1}
\end{aligned}
\tag{2.4}
$$

using the matrix inversion lemma [2].

The cost function as defined in section 1.2 can be written as

$$
J = \frac{1}{2}(\theta - \theta_0)^T \mathbf{P}_0^{-1}(\theta - \theta_0) + \frac{1}{2}(\mathbf{m}(\theta) - \mathbf{d})^T \mathbf{R}^{-1}(\mathbf{m}(\theta) - \mathbf{d})
\tag{2.5}
$$

then its Hessian is given by

$$
\mathbf{H} = \mathbf{P}_0^{-1} + \left(\frac{\partial \mathbf{m}}{\partial \theta} \right)^T \mathbf{R}^{-1} \frac{\partial \mathbf{m}}{\partial \theta} + \frac{\partial^2 \mathbf{m}}{\partial \theta^2} \mathbf{R}^{-1}(\mathbf{m}(\theta) - \mathbf{d}).
\tag{2.6}
$$

Hence the error covariance matrix of the control variables defined by equation (2.4) is given by the inverse of the Hessian as long as the nonlinear term, the third term on the right hand side of equation (2.6), is negligible, that is

$$
\widehat{\mathbf{P}} = \left(\frac{\partial^2 J}{\partial \theta^2} \right)^{-1}.
$$

The equivalence between the inverse Hessian and the estimated error covariance of the control variables, depends upon the degree of linearity in the model. The

---

[2] $\left(A^T B^{-1} A + C^{-1} \right)^{-1} = C - C A^T \left(A C A^T + B \right)^{-1} A C$ where the inverses exist, see Liebelt (1967) for details.

estimated error covariance of the estimated control variables is well approximated by the inverse Hessian, as long as $\mathbf{m}(\boldsymbol{\theta})$ is linear in the vicinity of the minimum of the cost function, J. Hopefully a nonlinear model may be regarded as linear in a sufficiently small neighborhood of the minimum of the cost function.

2.2 Scaling of the control variables

The Hessian matrix of second derivatives expresses the curvature of the cost function in the vector space spanned by the control variables. A high curvature in a certain direction means that the cost is strongly sensitive to variations in the linear combination of control variables that lie in that direction. For example, for the cases presented in the last chapter a velocity observation at day 1 is strongly sensitive to the vorticity initial conditions at grid points near the current meter location.

Conversely, control variables that have little or no influence on the cost correspond to directions in control–space with very flat curvature. These produce "valleys" in the cost function that can slow down the gradient–search minimization. The eigenvalues of the Hessian matrix associated with these flat directions are very small which can render the Hessian ill–conditioned and difficult to invert. The presence of terms in the cost function expressing the size and smoothness of the control variables, provides some curvature in all directions of control–space, thus rendering the Hessian more well–conditioned.

How the cost function is minimized with respect to the control variables using the adjoint method, is described in detail in the appendix. The limited–memory quasi–Newton method that is used as a minimization algorithm here, constructs an approximation to the Hessian matrix of the cost function at each iteration. The minimization will converge to a minimum in fewer iterations if the Hessian is well–conditioned. For more information on the above points, and the importance of the

Hessian matrix in minimization problems, the reader is referred to Thacker, (1989), and Gill *et al.*, (1981).

By scaling the control variables the Hessian can be rendered well–conditioned. The ideal scaling would be that which transforms the Hessian matrix into the identity matrix. If the form of the Hessian were known beforehand, one could perform the following scaling,

$$
\begin{aligned}
\mathbf{H}^{-1} &= \; <(\hat{\theta} - \theta)(\hat{\theta} - \theta)^T> \\
\mathbf{H}^{\frac{1}{2}}\mathbf{H}^{-1}(\mathbf{H}^{\frac{1}{2}})^T &= \; <\mathbf{H}^{\frac{1}{2}}(\hat{\theta} - \theta)(\hat{\theta} - \theta)^T(\mathbf{H}^{\frac{1}{2}})^T> \\
\mathbf{I} &= \; <(\hat{\mathbf{z}} - \mathbf{z})(\hat{\mathbf{z}} - \mathbf{z})^T>
\end{aligned}
$$

where $\hat{\mathbf{z}} = \mathbf{H}^{\frac{1}{2}}\hat{\theta}$ and $\mathbf{z} = \mathbf{H}^{\frac{1}{2}}\theta$. This scaling can rarely be done as the form of the Hessian is usually not known before the minimization.

From the expression for the Hessian given by equation (2.6), one can see that $\mathbf{P}_0^{-1}$ is an *a priori* estimate for the Hessian. In section 1.2, $\mathbf{P}_0^{-1}$ was defined as the sum of the weighting matrices in the cost function for size and smoothness of the control vector. One would like the scaling to be a vector, so a practical choice for the scaling is for $\mathbf{z} = \mathbf{R}_{\theta\theta}^{-\frac{1}{2}}\theta$. For the experiments of chapter one, $\mathbf{R}_{\theta\theta}$ was a diagonal matrix with the expected variance of the vorticity initial conditions, $<(\zeta_{ij}^0)^2>$ on the main diagonal. Hence the size of the scaled vorticity initial conditions were all of order one. For the experiments of chapter three, we shall see how important the choice of scaling is for the success of the assimilation.

2.3 Computing the error covariance matrix

For many optimization problems in oceanography, computing the Hessian is prohibitive because of its large dimension (e.g., Marotzke & Wunsch, 1993; Schiller, 1995). The Hessian has NxN elements where N is the number of control variables, and can often be too large for inversion using available computing resources. This is

not a problem for the cases presented here where there are O(1000) control variables. One can readily invert the Hessian, as long as it is well–conditioned.

In this section are presented two methods of computing the error covariance matrix given by the inverse Hessian of the cost function (2.5). These methods are applicable when the adjoint method has been used to find the minimum of the cost function.

2.3.1 Finite differences

At the end of the minimization using the adjoint method, one has the optimally estimated control variables, denoted $\hat{\theta}$, and the gradient of the cost function with respect to the control variables at the optimal estimate, $\frac{\partial J}{\partial \theta}(\hat{\theta})$. In a perfect world this latter term goes to zero in the course of the minimization. In practice the minimum is found by iteration, and the minimization stops when the norm of the gradient falls below some small value. The small finite values left in the gradient vector at the end of the minimization correspond to changes in the control variables that cause very minor differences to the estimated flow field (Wang *et al.*, 1992).

To calculate the Hessian matrix of second derivatives, each control variable is perturbed by a small amount, then the gradient of the cost function is calculated using the adjoint model at the perturbed point in N–space. The unperturbed gradient is subtracted from the perturbed gradient, and this difference is divided by the magnitude of the perturbation to give a finite–difference approximation to the Hessian, ie.

$$\mathbf{H} = \frac{1}{\Delta \theta} \left[\frac{\partial J}{\partial \theta}(\hat{\theta} + \Delta \theta) - \frac{\partial J}{\partial \theta}(\hat{\theta}) \right].$$

The ijth element of $\mathbf{H}$ is

$$H_{ij} = \frac{1}{\Delta \theta_j} \left[\frac{\partial J}{\partial \theta_i}(\hat{\theta} + \Delta \theta_j) - \frac{\partial J}{\partial \theta_i}(\hat{\theta}) \right]$$

This requires the gradient to be calculated as many times as there are model parameters, but one can use the existing adjoint model code.

47

Caution must be exercised in determining the correct size of the perturbation so as to minimize truncation error and machine error. These two errors are proportional to the size of the perturbation in opposing ways: (i) If $\Delta\theta$ is too large the finite-difference approximation is poor due to the truncation of the Taylor series, and the error in the approximation is proportional to $O(\Delta\theta)$; (ii) If $\Delta\theta$ is too small the subtraction on the right–hand side of the above equation will be between terms that are the same to a high number of significant figures, and because the computer has a limited number of significant figures available (16 for the double precision FORTRAN used here), accuracy is lost and the error is proportional to $O(\Delta\theta^{-1})$. See Gill $et\ al.$, 1981, for further details.

A variety of perturbation sizes were employed to find the optimal step–length, $\Delta\theta$, for which the computed second derivatives were stable.

The aim is to construct the error covariance matrix given by equation (2.4). Thus a disadvantage of this method is that the computed Hessian will contain the nonlinear term, that is the third term on the right–hand side of equation (2.6). If the size of this nonlinear contribution is significant the inverse of the computed Hessian will not be a good approximation to the error covariance. The first two terms in (2.6) are positive definite and hence well–conditioned; should the third term, which is indefinite, be significant it could render **H** ill–conditioned and not invertible

2.3.2 Sensitivity matrix

This method of computing the Hessian is taken from Thacker (1989). The nonlinear term in the expression for the Hessian (2.6) is ignored in this calculation, as without it the inverse Hessian is equivalent to the error covariance in the estimated control variables. All that is then needed to compute the Hessian is the calculation of the so–called sensitivity matrix $\frac{\partial \mathbf{m}}{\partial \theta}$.

For M data points and N control variables, **m** and **d** are vectors of dimension M, θ has dimension N, and the sensitivity matrix has dimension MxN. Each row of

the sensitivity matrix is a measure of the sensitivity of a particular model counterpart of a datum to variations in all of the control variables. The ijth entry is the gradient of the model counterpart of the jth datum with respect to the ith control variable. In section 2.5 the structure of the sensitivity matrix is explored in more detail. The sensitivity matrix is readily calculated using the forward and adjoint models, by the following procedure:

(i) The cost function J in the adjoint model code is replaced by the model counterpart of the jth datum, $m_j(\boldsymbol{\theta})$.

(ii) The adjoint model is run using the optimal control variables $\hat{\boldsymbol{\theta}}$ previously estimated.

(iii) The Lagrange multipliers then give the gradient of m_j with respect to $\boldsymbol{\theta}$, which is the jth row of the sensitivity matrix.

(i) to (iii) are performed over all M data to compute the sensitivity matrix row by row. The Hessian is then calculated by equation (2.6) without the nonlinear term.

The existing adjoint model code, that was used to find the gradient of the cost function with respect to the vorticity initial conditions, needs to be slightly modified to accommodate the different forcing function in the adjoint equations due to the cost function being defined differently. With this method the adjoint model only needs to be run M times. This is an immediate advantage over the finite–difference method if there are more control variables than data (M<N), as is often the case.

Neglecting the nonlinear term in (2.6) has two benefits. The first is that the inverse Hessian will be equivalent to the control variable error covariance as expressed in equation (2.4), which is the desired quantity. The second is that the first two matrices on the right–hand side of (2.6) are positive–definite whereas the third nonlinear term is not, so the inverse of $\mathbf{H}$ will be well–conditioned.

If the nonlinearities in the model are weak, both of the methods described here should produce the same estimates of the Hessian. However the finite–difference method is more prone to errors arising from the size of the step–length, which could

49

deteriorate the conditioning of its computed Hessian. The difference between the two methods lies in the nonlinear term, which is present in the finite–difference form but neglected in the sensitivity matrix form. The nonlinear term is important only in so far as it can show how bad an assumption of linearity near the minimum may be. In the end, the nonlinear term is ignored when the error covariance matrix is equated with the inverse Hessian.

Another method of computing the Hessian is given by Wang *et al.*, (1992). They construct a second order adjoint model using the tangent–linear formulation of the adjoint model (see Talagrand & Courtier, 1987). Through one iteration of their second order adjoint model, the Lagrange multipliers give the product of the Hessian and a vector of perturbations. Thus through N iterations the Hessian can be constructed column by column. As with the sensitivity matrix method, the forward model is linearized about the optimally estimated control variables. Theoretically, the second order adjoint should give the same results as the sensitivity matrix method, however it takes N iterations instead of M iterations to compute the Hessian. An advantage of the second order adjoint method is that the condition number of the Hessian is available at each iteration, which reflects the convergence rate of the minimization and provides information on the scale of changes being made to the control variables as the minimization progresses (see Navon *et al.*, 1992).

2.4 Estimated uncertainty in the initial conditions

The error covariance matrix of the optimally estimated vorticity initial conditions is estimated for two different experiments; case B1 from chapter one which uses strongly nonlinear dynamics, and the same experiment but using more linear dynamics. The two different experiments are performed so as to investigate the effect that nonlinearity has on the assimilation, in particular on the calculation of the inverse Hessian.

Recall that the error in the vorticity initial conditions as presented here arises only from the model/data misfit terms in the cost function. The boundary values of streamfunction and vorticity are treated as correct in the assimilation, and are not an explicit source of error in the calculation of the error covariance of the vorticity initial conditions. The imposed boundary conditions are of course a source of error in that they prevent the cost function from being minimized to a lower value. Since their values have no dependence on the control variables, they cannot have an estimated uncertainty arising from the estimated uncertainty in the control variables.

2.4.1   Using strongly nonlinear dynamics

For the cases presented in chapter one, the advective acceleration dominates the time evolution of the vorticity field. In fact, $\frac{U}{\beta L^2} = \infty$ since β is set to zero, and $\frac{UT}{L} = 7$, where $U = 1 \; m/s$ is the maximum speed in the jet, $L = 50 \; km$ is its length–scale of variation, and $T = 4 \; days$ is the time–scale. A fluid particle travels 1000 kilometers in 24 days, so much of the flow seen by the observing array originates from outside of the boundaries of the false model domain.

Using the optimal initial conditions estimated in case B1, chapter one, the Hessian is calculated using both of the methods described in the previous section. Both methods produce Hessian matrices that are the same to a high order. The root–mean–square difference between the two Hessian matrices divided by the root–mean–square average of the two Hessian matrices is 0.07. However only the Hessian calculated by the sensitivity matrix method is well–conditioned (low condition number) and hence readily invertible.

The condition number (ratio of the largest eigenvalue to the smallest eigenvalue) of the finite–difference Hessian is very large. This may be due to either the nonlinear contribution from $\frac{\partial^2 \mathbf{m}}{\partial \theta^2}$ multiplied by the residual $(\mathbf{m}(\theta) - \mathbf{d})$, or the truncation error from using finite differences to calculate the second derivative from the first derivative, or both. The former source of ill–conditioning occurs when a datum is a

51
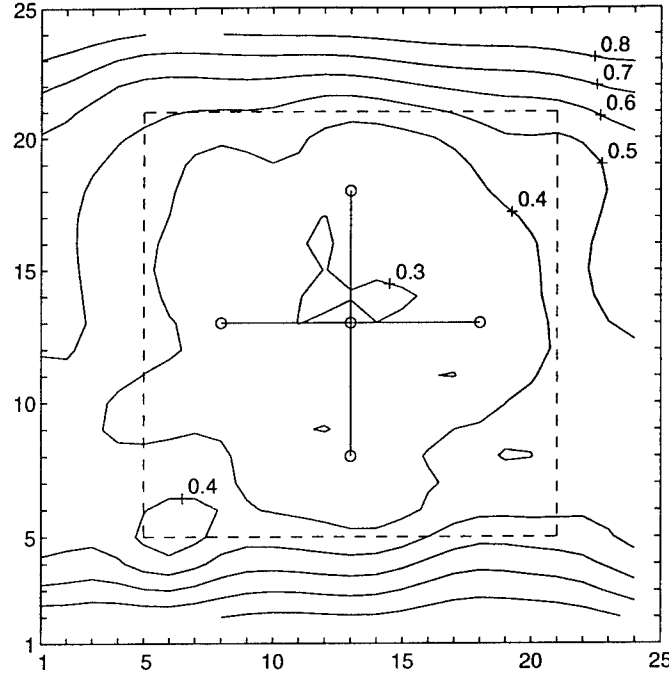
Figure 2.1: Relative error in the estimated vorticity initial conditions for the strongly nonlinear case (B1).

strongly nonlinear function of the control variables, ie. when a velocity observation at some late time depends nonlinearly upon the vorticity initial condition. In this case the shape of the cost function in the vicinity of the minimum need no longer approximate a quadratic, so the Hessian may not have all positive eigenvalues. The latter source of ill–conditioning arises when a control variable, θ_i, has very little influence over any of the data, then $\frac{\partial J}{\partial \theta_i} \approx 0$ and the second derivative of J in the ith direction may be very small. Hence the ith eigenvalue of the Hessian may be very small.

In figure 2.1 is shown the relative error in the estimated vorticity initial conditions, defined by

$$\text{relative error} = \sqrt{\frac{diag\left(\mathbf{H}^{-1}\right)}{|\mathbf{P_0}|}}$$

This ratio of the *a posteriori* to the *a priori* expected variance, is a measure of how well the assimilation of the available data has improved the estimated uncertainty in the vorticity initial conditions.

As one would expect the relative error is lowest in the vicinity of the observation locations. The relative error is slightly lower to the southwest of the array. The observing array mainly sees fluid moving into the array from the southwest, so the model/data misfit is quite sensitive to the vorticity initial conditions to the southwest, which are therefore estimated with greater accuracy.

2.4.2 Using weakly nonlinear dynamics

The dynamics of the flow field are rendered more linear by reducing the size of the ratio of relative vorticity gradient to planetary vorticity gradient. That is, $\frac{U}{\beta L^2} = 0.1$, by setting the maximum speed in the jet to $U = 0.02$ m/s, with $\beta = 1.8 \times 10^{-11}$ $m^{-1}s^{-1}$, and length–scale of variation, $L = 100$ km. A fluid particle travels 40 kilometers in 24 days, which is two grid points. The flow is now sluggish enough to feel the ambient planetary vorticity gradient and the flow can be described by Rossby waves.

An assimilation is performed using the same experimental set–up as for case B1, but with the above changes to U and β and L. In figure 2.2 is shown the true and estimated streamfunction fields (note that a smaller contour interval is used here). For this case the cost function is successfully minimized in many fewer iterations than in the nonlinear cases.

The Hessian is calculated using both of the methods described in the previous section, and with both methods the Hessians are well–conditioned and their inverses are the same. In figure 2.3 is shown the relative error. The relative error is lowest in the vicinity of the observing array, as was found with the nonlinear case. However the low relative error does not extend away for any great distance from the observing array, as it does in the strongly nonlinear case, because the fluid is moving relatively slowly, so that over the time of the assimilation the observing array only sees the fluid that is nearby.
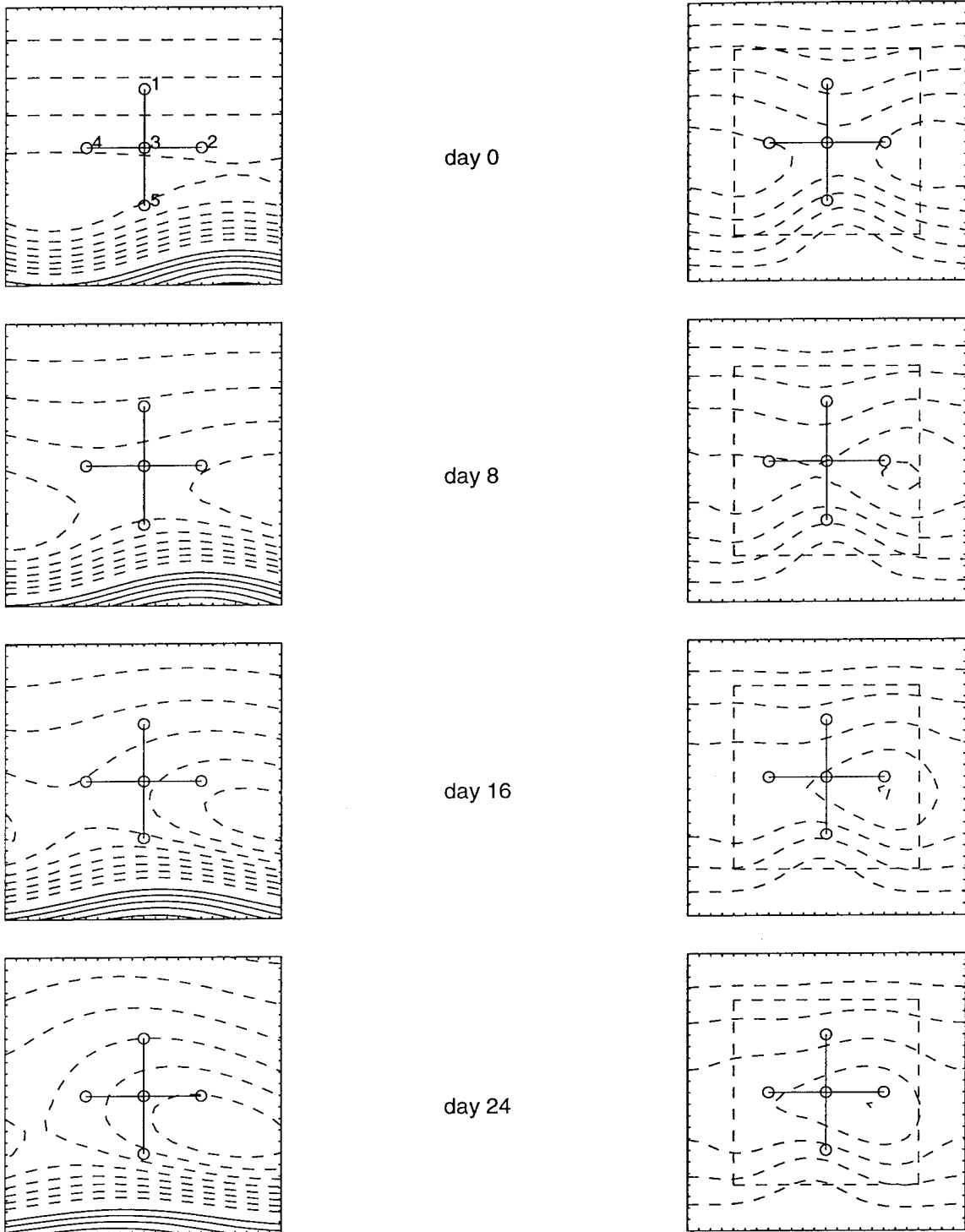
Figure 2.2: Using weakly nonlinear dynamics, the streamfunction every eight days for (left) the true ocean over the smaller domain, (right) the estimated ocean. (C.I.=200 m^2/s)
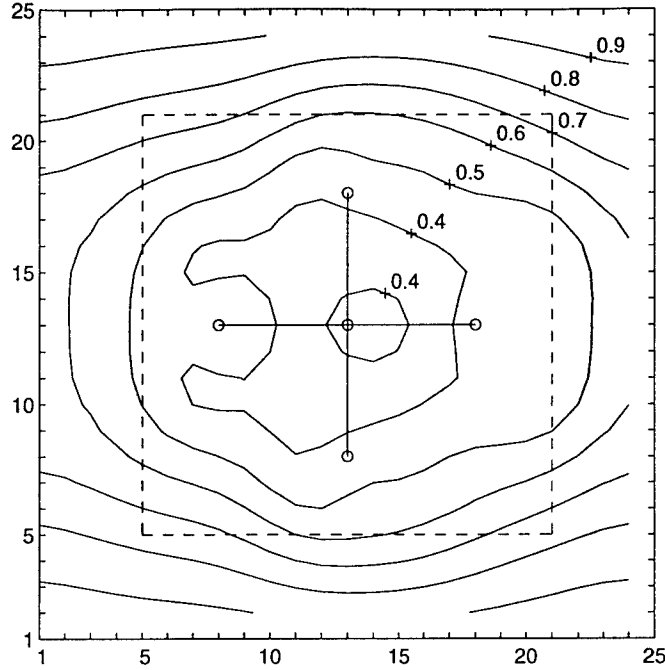
Figure 2.3: Relative error of the initial conditions for the weakly nonlinear case.

In the previous section where strongly nonlinear dynamics are used, the finite–difference Hessian is very similar to the sensitivity matrix Hessian, but ill–conditioned. For linear dynamics the finite–difference Hessian is found to be well–conditioned. Hence the source of ill–conditioning for the finite–difference Hessian in the nonlinear case is probably not due to truncation errors in the finite–difference computation.

These results suggest that even when the flow is strongly nonlinear, the nonlinear term $\frac{\partial^2 \mathbf{m}}{\partial \theta^2} \mathbf{R}^{-1}(\mathbf{m}(\theta) - \mathbf{d})$ in the expression for the Hessian (2.6) is small since the finite–difference Hessian is very similar to the sensitivity matrix Hessian. However it is big enough to ill–condition the finite–difference Hessian. The significant size of the nonlinear term is probably due to the residuals $(\mathbf{m}(\theta) - \mathbf{d})$ not being small. The model/data residuals for the estimated control variables for case B1 are not small as was seen from the true and estimated velocity time series in figure 1.5 and the final size of the cost function shown in figure 1.8.

For both strongly nonlinear dynamics and weakly nonlinear dynamics the relative error goes to one at the boundaries of the model domain. In effect this is a statement that the assimilation of observations cannot improve the *a priori* estimate of the vorticity initial conditions near the boundary, because the boundary values of vorticity are kept fixed.

The relative error maps give only a partial measure of the uncertainty in the estimated vorticity initial conditions. The sources of the errors estimated using the inverse Hessian are the errors in the observations and the *a priori* errors in the vorticity initial conditions, both of which are treated as random statistical errors. However there are also systematic errors in the assimilation that are not included in the estimated error in the vorticity initial conditions. The most important systematic error is the specification of boundary conditions as performed in cases A1, B1 and C1.

It was apparent from the results shown in chapter one that the specified boundary conditions were a source of error in the optimization because they prevented the cost function from being minimized successfully for cases B1 and C1. Hence the relative error maps are to be interpreted carefully. They are the errors in the vorticity initial conditions given a certain set of imposed boundary conditions which are regarded as perfectly known.

2.4.3 Off–diagonal structure

As the full error covariance matrix is calculated here, one can examine its off–diagonal structure. Previous model/data assimilation studies using the adjoint method, have estimated the uncertainties in the control variables by calculating elements of the main diagonal of the Hessian using finite–differences (Schiller, 1995). The inverse of each element is an approximation to the error covariance, assuming that the off–diagonal elements of the Hessian are negligible. The availability of the full covariance matrix allows a comparison to test the validity of this assumption.
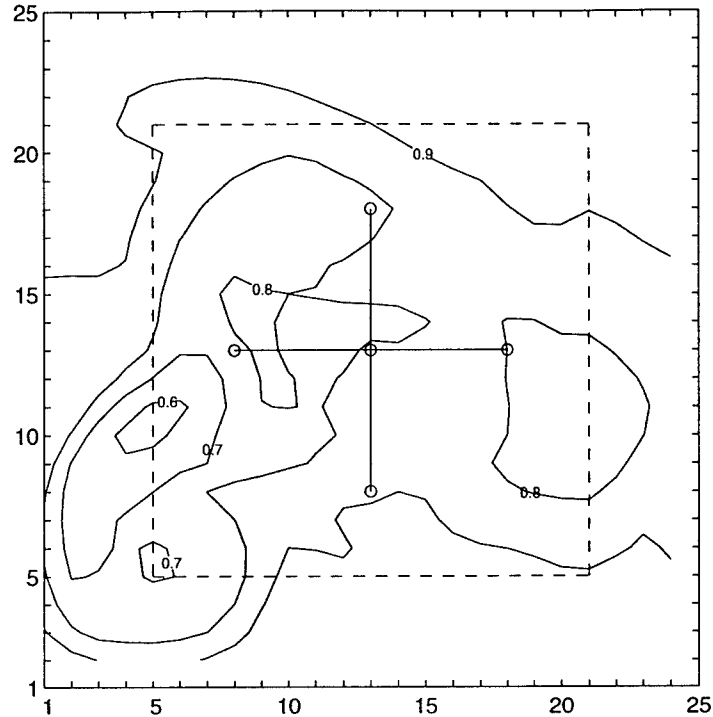
Figure 2.4: Relative error of the vorticity initial conditions for the strongly nonlinear case (B1), where all off–diagonal structure in the Hessian has been removed before inversion.

In figure 2.4 the relative error for the vorticity initial conditions from case B1 is shown, where all off–diagonal structure in the Hessian has been discarded. That is, the error covariance matrix is a diagonal matrix consisting of the inverses of each element of the diagonal of the Hessian. Figure 2.4 may be compared to figure 2.1 where the inverse Hessian kept all of its off–diagonal structure. The relative error is larger over all of the sub-domain in figure 2.4. This result implies that information about spatial correlations among the vorticity initial conditions is lost when the off–diagonal structure is ignored, resulting in larger estimated errors. The strong east–west symmetry seen in 2.1 and not in figure 2.4 is due to the off–diagonal terms from the Laplacian smoothing.

An example of the off–diagonal structure of the error covariance matrix is shown in figure 2.5, so as to illustrate the effect that the assimilation of data has on the estimated covariances among the vorticity initial conditions. The $78th$ column of

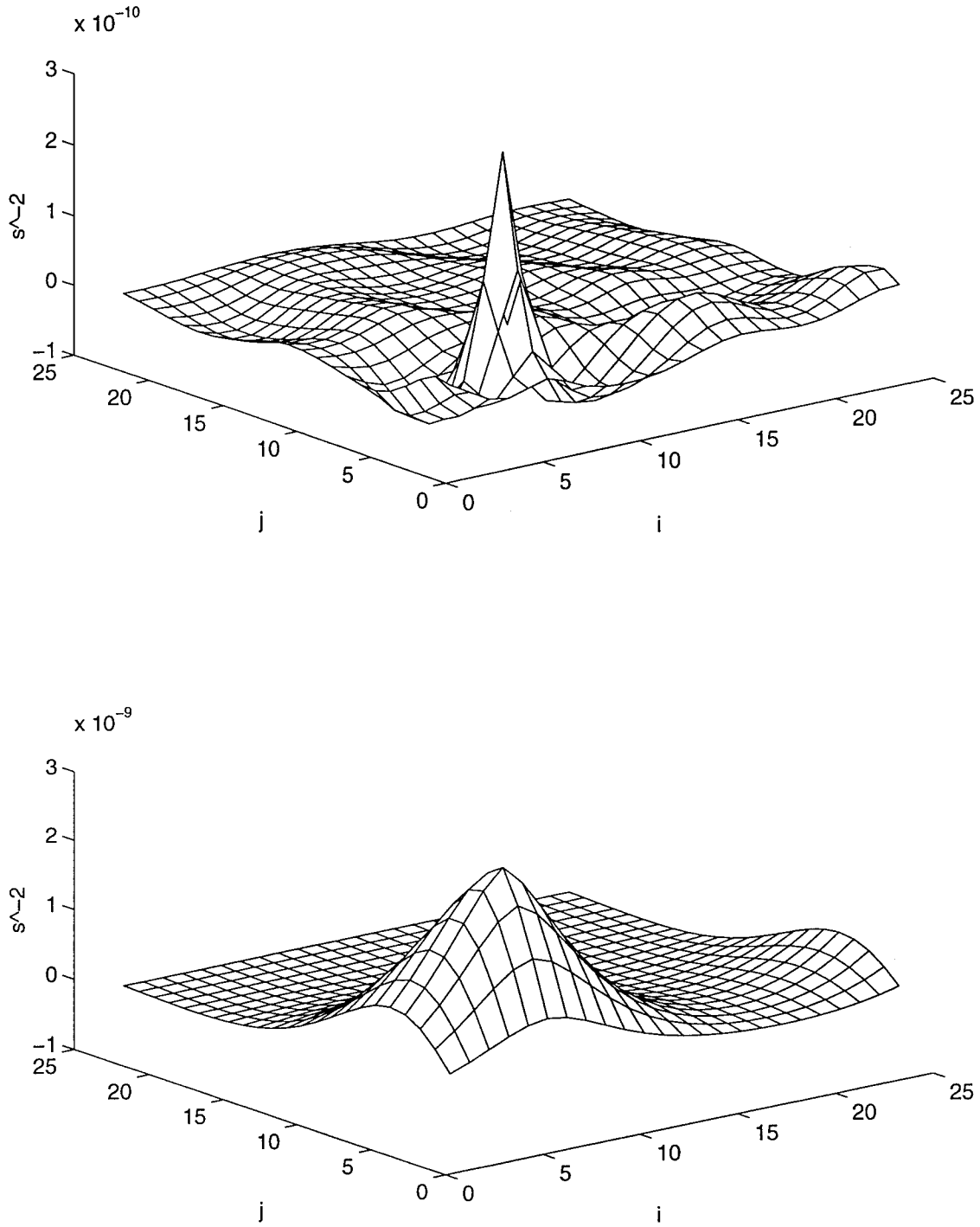Figure 2.5: The 78*th* column of the error covariance matrix for the strongly nonlinear case (B1). The covariance of the inital vorticity at $i = 6$, $j = 5$ with the vorticity at all other grid–points at the initial time is shown. The lower plot shows the *a priori* covariance taken from $\mathbf{P_0}$, the upper plot shows the *a posteriori* estimated covariance. Note the factor of ten difference in the vertical axis.

the error covariance matrix for case B1 is displayed, which corresponds to the initial vorticity at grid–point $i, j = (6, 5)$ located in the south–west of the sub–domain. The *a priori* covariance is compared to the *a posteriori* covariance. The former is the 78*th* column of $\mathbf{P_0}$, and the latter is the 78*th* column of the error covariance matrix calculated using the sensitivity matrix method.

The *a posteriori* covariances between the initial vorticity at grid–point $i, j = (6, 5)$ and all other grid–points is less than ten percent of the *a priori* covariances. The assimilation of data has decreased the size of the spatial covariances among the vorticity initial conditions. Furthermore, the gaussian shape of the smoothing term in the *a priori* covariance (see section 1.2) has been narrowed by the assimilation. There is an inherent length–scale for vorticity contained in the model dynamics that is shorter than the length–scale associated with the Laplacian smoothing in the *a priori* covariance (see figures 1.1 and 1.4). The estimated length–scale of the spatial covariances among the vorticity initial conditions is thus shortened by the action of the model dynamics during the assimilation.

2.5 Sensitivity

An interesting feature of the sensitivity matrix, introduced in section 2.3.2, is that it contains the gradients of the model counterparts of the data with respect to the control variables. For the procedure outlined in section 2.3.2, $m_k(\theta)$ is the model counterpart of the kth observation which could be say, eastward velocity taken at grid–point (i, j) at time t. It is given by

$$m_k(\theta) = \frac{(\psi_{i,j-1}^t - \psi_{i,j+1}^t)}{2dy}$$

Here θ is the vorticity initial conditions, upon which the streamfunction, ψ, depends at future times over the grid, and the subscript k refers to the ordering of the data.

For the calculation of the Hessian, $m_k(\theta)$ replaces equation (1.5) as the definition of the cost function. The same adjoint model equations as before are forced

59

using this cost function, as described in the appendix. The forcing term for the adjoint model equations is $\frac{\partial m_k}{\partial \psi^t_{i,j}}$, which is non–zero at only two points on the model grid,

$$\frac{\partial m_k}{\partial \psi^t_{i,j-1}} = \frac{1}{2dy}$$

$$\frac{\partial m_k}{\partial \psi^t_{i,j+1}} = -\frac{1}{2dy}.$$

Thus the adjoint model runs backward in time forced by an impulse at the location and time of the observation. The forcing term can be interpreted as the sensitivity of the eastward velocity at grid–point (i,j) at time t, to the streamfunction over all the grid at time t.

The adjoint equations propagate the impulses at these two points backward in time. When $t = 0$ is reached the Lagrange multipliers give the gradient of m_k with respect to the vorticity initial conditions, which constitutes the kth row of the sensitivity matrix. One could say that the sensitivity matrix is the Green's function response of the adjoint model to the spatio–temporal distribution of the data.

A particular row of the sensitivity matrix may be displayed to show the sensitivity that a particular model counterpart of a datum has to the vorticity initial conditions. For the weakly nonlinear case, figure 2.6 shows the first row of the sensitivity matrix. This is the sensitivity, with respect to the vorticity initial conditions, of the eastward velocity produced by the forward model at day 1 at current meter location 1, starting from the optimally estimated initial conditions. Since the eastward velocity is taken only two days after the initial time, this datum is most sensitive to the vorticity initial conditions in the immediate vicinity of the current meter location.

For an eastward velocity observation at the same location at a later time, $t = 23$ days, the influence of the vorticity initial conditions upon the observation has spread in space, as shown in figure 2.7. The region of greatest sensitivity is about two grid–points to the east of the current meter location. The slow westward flow in this region has, after 23 days, advected the vorticity initial conditions past the current

t = 1 day

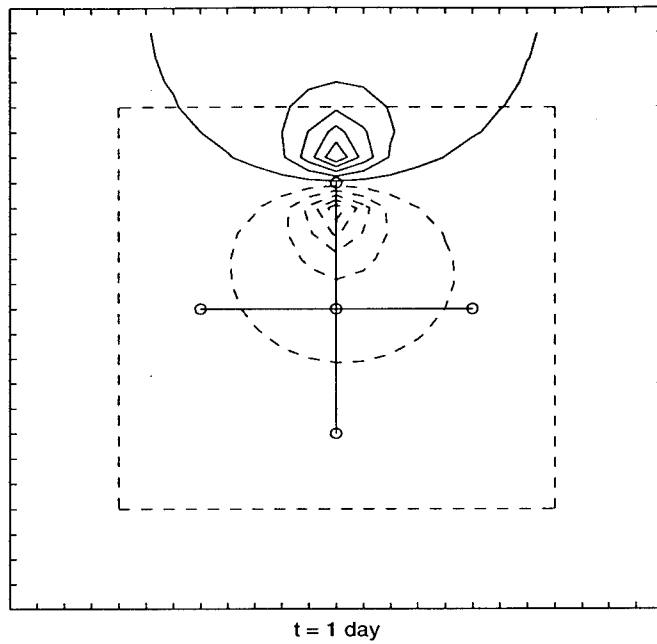Figure 2.6: Sensitivity of the eastward velocity recorded at current meter 1 at day 1 to the vorticity initial conditions for the weakly nonlinear case. (row 1 of the sensitivity matrix).
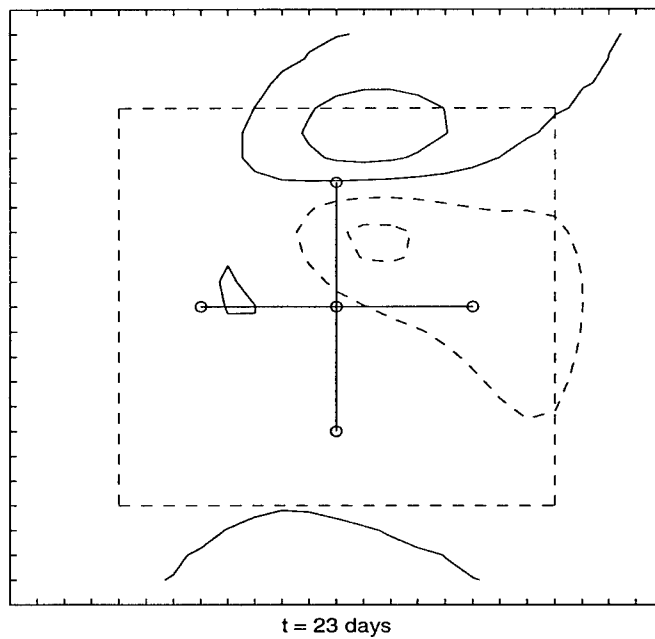

t = 23 days

Figure 2.7: Sensitivity of the eastward velocity recorded at current meter 1 at day 23 to the vorticity initial conditions for the weakly nonlinear case. (row 133 of the sensitivity matrix).

61

meter location. Also the pattern of the sensitivity away from the current meter location is indicative of the spread of information by Rossby waves. The average flow speed at this location is 0.3 cm/s, but the phase speed of a barotropic Rossby wave is about 7 cm/s in this setting. This is the phase speed for a wavelength of 400 km, which is approximately the wavelength of the flow seen in figure 2.2. In 23 days such a wave travels 145 km, about seven grid points, which can be seen in figure 2.7 as the range of influence of the estimated vorticity initial conditions on the datum.

For the strongly nonlinear case the picture is more convoluted. As can be seen in figure 1.3 the optimally estimated flow field is quite turbulent relative to the weakly nonlinear case. In figures 2.8 and 2.9 the sensitivities of the eastward velocity from current meter 1 at 1 day and at 23 days to the vorticity initial conditions are shown. Similar to the weakly nonlinear case, the datum at 1 day is most sensitive to the vorticity initial conditions in its immediate vicinity, but at 23 days the picture is quite different. The strong advective accelerations vigorously stir the initial vorticity field, causing the influence of the vorticity initial conditions upon the observed velocity to spread rapidly throughout the model domain.

t = 1 day

Figure 2.8: Sensitivity of the eastward velocity recorded at current meter 1 at day 1 to the vorticity initial conditions for the strongly nonlinear case. (row 1 of the sensitivity matrix).
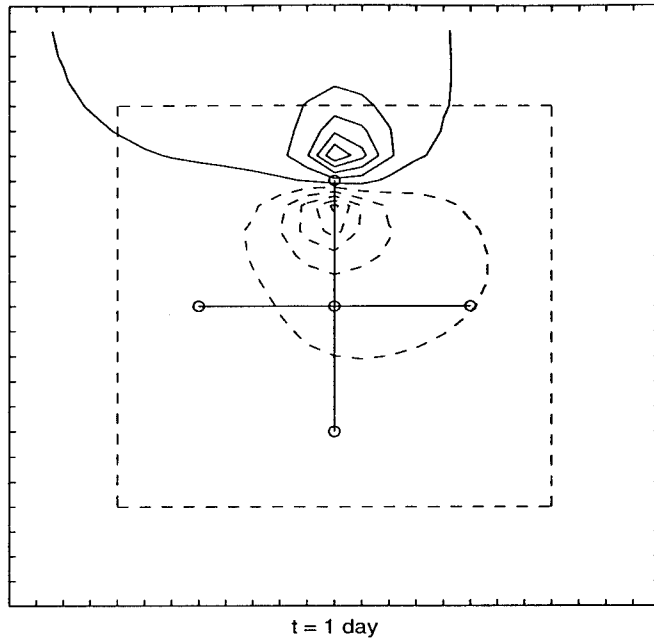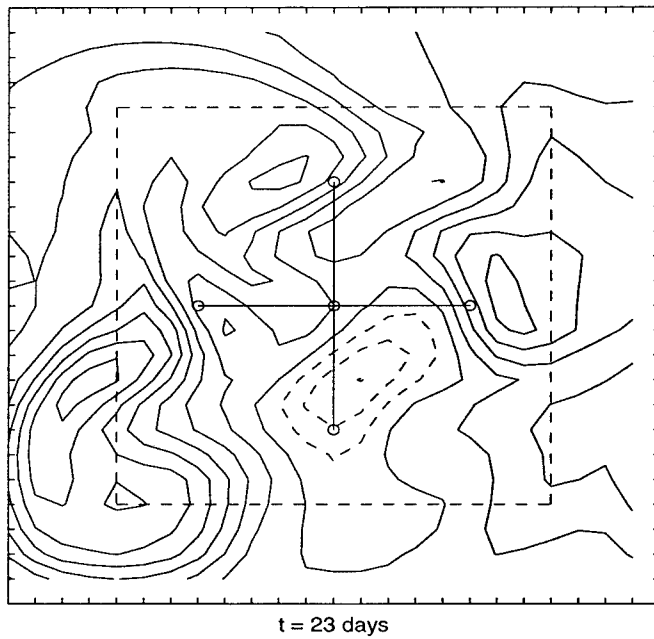

t = 23 days

Figure 2.9: Sensitivity of the eastward velocity recorded at current meter 1 at day 23 to the vorticity initial conditions for the strongly nonlinear case. (row 133 of the sensitivity matrix).

63

Chapter 3

Optimal estimation of boundary conditions

The results of the twin experiments performed in chapter one showed that the estimated flow field throughout the interior is strongly influenced by the specified boundary conditions. Much of the flow observed in the true flow field originates far from the observing array, from a distance that is much greater than the distance from the observing array to the boundaries of the sub–domain. Given a considerable lack of knowledge about the true time–dependent values of streamfunction and vorticity around the boundaries of the sub–domain, it becomes necessary to include the boundary conditions in the control variables.

The twin experiments of chapter one are now further developed to include the estimation of boundary conditions as well as initial conditions. The control variables are now the time–dependent boundary values of streamfunction and vorticity, and the initial values of vorticity at interior points of the model domain. This set of variables is sufficient to integrate the flow field forward in time (as was mentioned in chapter one). That is, all values of streamfunction and vorticity in space and time are determined by the control vector. In the experiments of chapter one, only the initial conditions were used as control variables, and the boundary values were imposed and

not varied in the course of the assimilation. The imposed values were based upon any *a priori* knowledge of the true flow field. Given a lack of *a priori* knowledge, the assimilation experiments are improved by including the boundary values as control variables.

In order to use the adjoint method to find the optimal control variables that minimize a cost function, expressions are needed for the gradient of the cost function with respect to the control variables. The gradient with respect to the initial vorticity conditions was used in chapter one. Here the gradient with respect to the boundary conditions is also needed. The expressions for all the cost function gradients are formulated in the appendix.

An optimal estimation of open boundary conditions using the adjoint method has been performed by Seiler (1993). A three–layer quasigeostrophic model of a mid–latitude jet was used to simulate the Gulf Stream. For the optimization the initial conditions were treated as known, and the control variables were the boundary values of streamfunction and vorticity in each of the three layers over a 36 day period. The assimilation scheme and the twin experiment configurations used here are very similar to those she used. Apart from the fact that she assimilated simulated altimeter data, the main differences between this study and Seiler (1993) are:

(i) Barotropic versus three–layers in the vertical; most of the energetic flow in Seiler's model occurs in the upper two layers, the flow in the bottom layer is quite weak. Hence, in terms of quasigeostrophic dynamics, much of the variability of the flow field in the three–layer model is occurring on the scale of the baroclinic radius of deformation which is much shorter than the width of the model domain. In the barotropic model used here, all of the variability is in the barotropic mode which has an effectively infinite radius of deformation. Hence the streamfunction on the boundary of the barotropic model instantly feels any change in vorticity anywhere else in the domain. This will be seen to have a significant effect on the gradient of the cost function with respect to boundary streamfunction.

(ii) Seiler kept the initial conditions fixed (assumed to be known perfectly), and expanded the time–dependent boundary values of streamfunction and vorticity in a Fourier sine series. The coefficients in the series were used as control variables. Here the initial vorticity conditions are treated as unknown and are included in the control vector along with the boundary values. This is clearly a more realistic approach as it reduces the number of *a priori* assumptions about the flow field. When the choice of first guess for the initial and boundary conditions is made along with their expected size and smoothness, *a priori* assumptions are indeed made but they are modified during the optimization.

The novel results of this chapter are the successful estimation of initial conditions together with time–dependent boundary conditions. The assimilation is able to create temporal variation at the boundaries that causes interior flow patterns that well match the strong signals in the interior velocity observations. The assimilation performs well even when noise is added to the observations and the first guess for the control variables. In Seiler (1993) the first guess was chosen to be ten percent different from the true values of the control variables. Here all of the choices of first guess are much further from their true values.

Several case studies are presented here, showing some successful results and illustrating the problems associated with the estimation of boundary conditions. The quality of the estimated control variables for each experiment, in terms of a comparison with the true values and their sensitivity to the data, is presented in the next chapter.

3.1   Boundary values as control variables

A first problem that arises when boundary values of streamfunction and vorticity are used as control variables in a time–dependent assimilation is their large number. For a 24 day assimilation period with $\Delta t = 1$ hour and with 25 grid points along each

k	1	2	3	4	5	6	7	8	9	10	11	12
Period	24.00	12.00	8.00	6.00	4.79	4.00	3.42	3.00	2.67	2.38	2.17	2.00

Table 3.1: Periods in days of the expansion coefficients for the boundary values in equation 3.1 for truncation $K = 12$, for a 24 day assimilation period.

edge of the model domain, there are $110,784$ values of streamfunction and vorticity to be estimated. Such a large number of variables is not necessary to describe the flow field adequately because there is a high temporal correlation in both streamfunction and vorticity at short time–scales. Advantage is taken of this correlation to reduce the number of degrees of freedom in the model that is used for the assimilation.

The time series of streamfunction and vorticity at each point on the boundary, here denoted q_t, are each expanded in a Fourier series with a linear trend,

$$
\begin{aligned}
q_t &= \frac{1}{\sqrt{T}} \Re \left\{ \sum_{k=-K}^{K} \phi_k \exp \frac{i 2\pi kt}{T} \right\} \\
&= \frac{a_0}{\sqrt{T}} + \frac{2}{\sqrt{T}} \sum_{k=1}^{K} \left[a_k \cos \left(\frac{2\pi kt}{T} \right) - b_k \sin \left(\frac{2\pi kt}{T} \right) \right] + c \frac{t}{T}
\end{aligned}
\tag{3.1}
$$

for $t = 0, \ldots, T$, and where $\phi_k = a_k + i b_k$. Thus the time series is represented by a DC component, a_0, K cosine and sine coefficients, a_k and b_k, and a linear trend coefficient, c. This expansion, without the cosine terms, is the same as that used by Seiler (1993).

The linear trend is removed from the boundary time–series before the Fourier series is taken, so as to render the time–series continuous at the beginning and the end of the assimilation period. By doing so there is less demand for high–frequency energy in the Fourier series, so the series can be truncated at a lower cut–off, K. The number of control variables needed to adequately describe the boundary time series is substantially reduced by truncating the series. By truncating the series the assimilation period may be lengthened without increasing the number of control variables, with the trade–off that high frequency motions are filtered out at the boundaries, which can introduce errors.

The forward model is run for 24 days with different truncations to assess the effect that the boundary expansion has on the interior flow field. In figure 3.1 the error is shown in the streamfunction and vorticity fields in the interior as a function of time when the minimum periods allowed for in the expansion are $1(K = 24)$, $2(K = 12)$, $3(K = 8)$ and $4(K = 6)$ days where $T = 577$ (24 days). The error is defined as the rms difference between the interior streamfunction field of the model run with a truncated Fourier series and the model run with the full temporal variability of the boundary values, normalized by the rms variability of the model run with the full temporal variability. The error increases as K decreases. The error stays well below one percent for $K = 12$, and this is the truncation used for the twin experiments in this chapter. With this truncation the minimum period of variability of the boundary values is two days, and the number of control variables representing the boundary values of streamfunction and vorticity is reduced from $110,784$ to $5,521$.

The control variables are now the expansion coefficients $\{a_0, a_1, \ldots, a_K, b_0, b_1, \ldots, b_K, c\}$ from (3.1) for streamfunction and vorticity at each boundary point. These, along with the vorticity initial conditions at interior points, are assembled into one control vector. The period corresponding to each expansion coefficient is shown in table 3.1.

3.2 Scaling of time-dependence

With boundary streamfunction and vorticity in the frequency domain rather than the time domain, the scaling of the control variables for the optimization algorithm requires careful consideration. In section 2.2 it was shown how control variables should be scaled so as to render the Hessian well–conditioned during the minimization. A practical choice of scaling is the square root of the *a priori* expected size variances for each control variable. If the control variables were kept as time series of streamfunction and vorticity on the boundary, the scaling would simply be the expected sizes
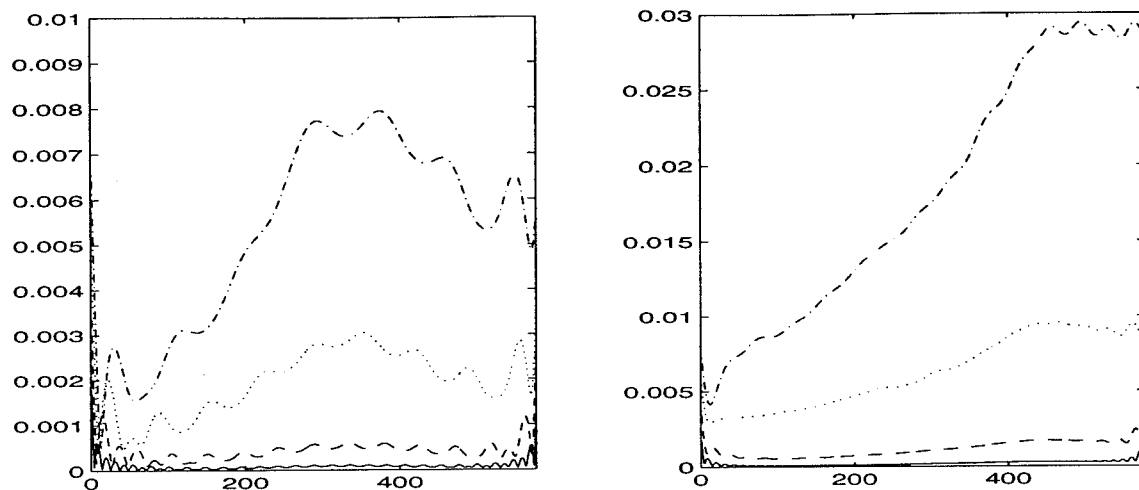
Figure 3.1: Growth of errors for (left) streamfunction and (right) vorticity when variability with periods < 1 day (solid), < 2 days (dash), < 3 days (dot) and < 4 days (dot–dash) is filtered from the boundary values.

of streamfunction and vorticity. In the frequency domain the expected sizes of the Fourier coefficients for a typical time series may vary by several orders of magnitude.

Seiler (1993) chose the scale vector by taking a typical forward model integration, expanding the boundary values of streamfunction and vorticity by (3.1), then taking the rms values of the coefficients. It is apparent from the behavior of the dynamics used in the forward model as presented in chapter one, that there is little energy at high frequencies in the true flow field. Hence the rms scaling has a somewhat red character.

As in the experiments in chapter one, terms are included in the cost function expressing the size and smoothness of the boundary values of streamfunction and vorticity. Without these terms the optimization produces estimates that can be arbitrarily large and noisy. The inclusion of these terms supposes that one has some *a priori* estimate of the rms size and smoothness of the streamfunction and vorticity fields. The useful function of the size and smoothness terms is to lend some curvature to the cost function in regions devoid of data (Thacker, 1988). The cost function is deemed adequately minimized when the residual variances in the size, smoothness

69

Experiment	Scaling	First Guess	Sampling Interval (no. time steps)	Observational Noise
A2	rms	zero	48	no
B2	flat	zero	48	no
C2	flat	persist true i.c.	48	no
D2	flat	persist true i.c.	1	no
E2	flat	perturb 25 %	1	no
F2	flat	persist true i.c.	48	yes
G2	flat	persist obj. map i.c.	48	yes

Table 3.2: Parameters used for the optimization for each experiment, the meaning of the entries is explained further in the text.

and model/data misfit terms are of the same order as their *a priori* variances. When this is the case, the value of the cost function is of order unity.

Twin experiments are run using the same model parameters and observing array as those used in cases B1 and C1 in chapter one, except that now the expansion coefficients of the boundary values of streamfunction and vorticity are included in the control variables. Table 3.2 shows the differences among the twin experiments presented in this chapter.

The performance of the optimization for each experiment is shown in figure 3.2. Plotted is the value of the cost function versus number of iterations. The details of an iteration of the adjoint method are presented in section A.2 of the appendix. One iteration may contain several calls to the forward and adjoint models, before a new minimum is found. For the minimization routine used in all of these experiments, the L–BFGS limited–memory quasi–Newton method, the minimization stops when the norm of the gradient vector falls below a certain value (see appendix, page 144). With this method, approximations to the Hessian are calculated at each iteration so that the new minimum in the downhill direction can be determined. At the start of the minimization the Hessian of the cost function is initialized as the identity matrix, then as the minimization proceeds the Hessian matrix is reconstructed including the non–diagonal terms.
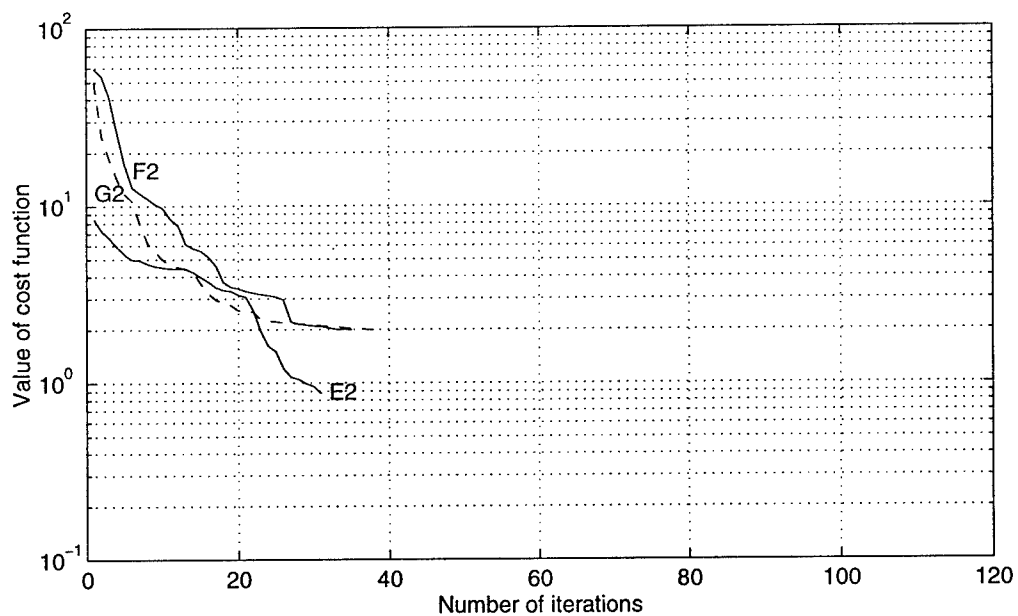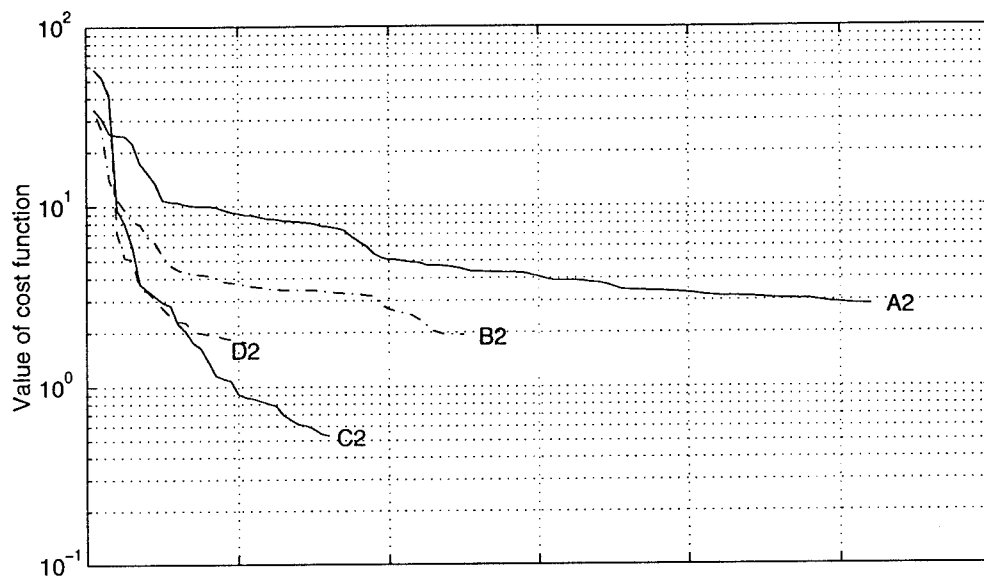
Figure 3.2: Performance of the minimization for each experiment, the value of the cost function versus iteration is plotted for each experiment. Two frames are used so that each curve may be clearly seen.

It was seen in chapter two that when the dynamics are strongly nonlinear, the form of the Hessian may depend upon the value of the control vector (see equation 2.6). That is, the shape of the cost function may show large departures from a paraboloid, in which case the curvature is not constant in control space. After a number of iterations the minimization may stop because according to the reconstructed curvature of the cost function (the Hessian), it cannot proceed downhill anymore, even if the norm of the gradient is still large. When this happens the minimization is restarted at the last position of the control vector, with the Hessian re-initialized to the identity matrix. In figure 3.2, the sharp changes in direction seen in the minimization curves correspond to points where the minimization is restarted.

<u>Case A2</u>: Assuming no prior knowledge of the initial and boundary conditions save an estimate of their expected variance and smoothness, the choice of first guess for all of the control variables is zero. The scale vector for this case is chosen as the rms of the initial and boundary conditions from a typical model run, as was done by Seiler (1993).

The optimization reduces the cost function adequately (see figure 3.2) although requiring far more iterations than the other cases. In figure 3.3 the streamfunction in the model domain as a function of time is shown, both for the true flow field from which the observations were taken, and for the flow field arising from the optimally estimated control variables for case A2. One can see that the estimated flow resembles the true flow only in the vicinity of the observing array. In the course of the optimization the model/data misfit at the array does not need to force the boundary streamfunction and vorticity values very far from their first guess values of zero.

In the upper plot of figure 3.4 the magnitude of the scale vector is plotted, as well as the absolute value of the estimated control vector at the end of the minimization. The scale vector and the control vector are ordered in the following manner: the first 529 elements are the vorticity initial conditions at all interior points, the next $2,496$ are the expansion coefficients for streamfunction along each of the four
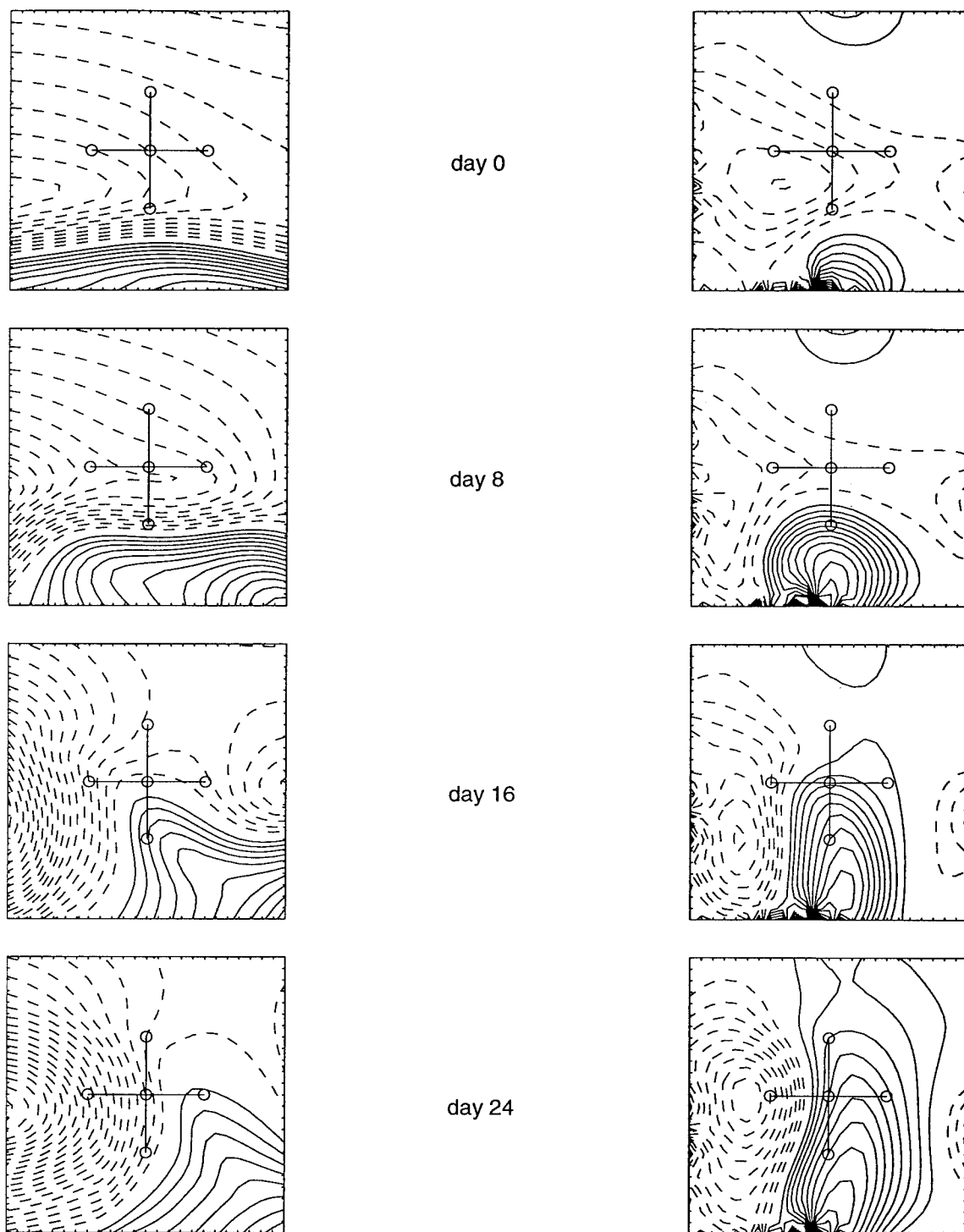
Figure 3.3:   Streamfunction every 8 days for (left) the true flow field and (right) the estimated flow field for experiment A2 which starts from a zero first guess, with the rms of the true boundary conditions used for scaling. (C.I.=5000 m^2/s)

Figure 3.4: Scale vector (solid) and absolute value of the estimated control vector (dots) for experiment A2. Top: all control variables (see text), and Bottom: a portion consisting of the expansion coefficients for streamfunction at points along the western boundary.

74

boundaries and the last 2,496 are the expansion coefficients for vorticity along each of the four boundaries.
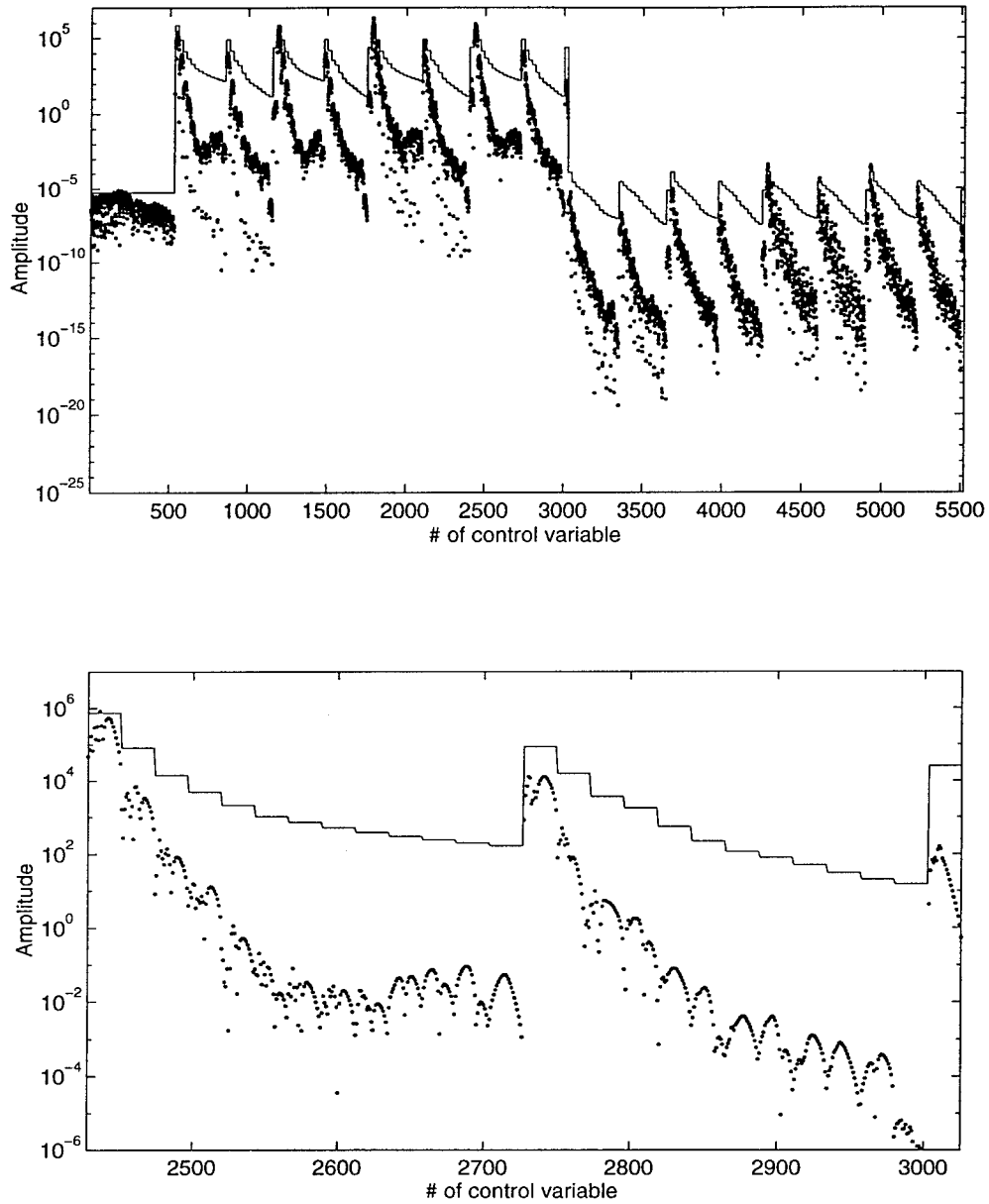
In the lower plot of figure 3.4 is shown a blow–up of a portion of the upper plot. Shown here are the estimated expansion coefficents and their scale for the streamfunction along the western boundary. Here the first 23 points correspond to the values of a_0 at the 23 grid points along the western boundary. The next 23 points are the values of a_1 along the western boundary and so on. [1].

The red frequency dependence of the rms scaling is also apparent in the estimated expansion coefficients shown in figure 3.4. In fact there appears to be more redness in the estimated expansion coefficients than in the scaling. As can be seen, the DC components (a_0) of streamfunction and vorticity at boundary points are the only control variables whose magnitudes are of the same order as their scale. The magnitudes of the sine and cosine coefficients (a_k and b_k) and of the linear trend coefficient (c), all fall well below their scales, in some cases by many orders of magnitude.

The control variables that are given the larger a priori variances, and hence the larger scales, are preferentially varied by the minimization algorithm during the search for the minimum of the cost function. The smaller the a priori variance for a control variable the more it is constrained to its a priori value. This can be seen in the estimated expansion coefficients for streamfunction and vorticity on all boundaries. The low–frequency expansion coefficients have larger a priori variances than the high–frequency expansion coefficients, and all expansion coefficients are given an a priori size of zero. Thus the estimated boundary conditions are comprised almost entirely of low frequencies. The high frequency motions present in the true boundary conditions are not captured in the estimated boundary conditions.

Various experiments were performed using different forms of frequency dependence to construct the a priori variances of the expansion coefficients (such as f^{-2},

---

[1]For these experiments, the model domain has $n = 25$ points in the zonal direction, and $m = 25$ points in the meridional directions. The corner points are included in the northern and southern boundaries for the organization of the control vector

f^{-1}, e^{-f/f_0}). It was found that the rms scaling used in the above experiment, the solid line in figure 3.4, is approximately proportional to *frequency*$^{-2}$. This particular scaling arises naturally out of quasigeostrophic turbulence.

To get temporal variability in the estimated boundary conditions of the same order as the temporal variability in the true boundary conditions, it was found necessary to use a "flat" scaling that is constant with respect to frequency. All of the other frequency dependencies produce boundary estimates that are nearly time–invariant. In fact the flat scaling is a more sensible choice than the rms scaling as it is a statement that one has no reason to weight one frequency higher or lower relative to another frequency. Furthermore the rms scaling chosen in case A2 can only be used in the context of twin experiments where one is in possession of the spectral density of the true flow field. For real data this sort of information is not available and a flat scaling is more appropriate.

Case B2: The parameters for this experiment are all the same as those used in case A2, except that a flat scaling is used where all expansion coefficients are given the same *a priori* variance as that of the DC components. Although the optimization performs well in that the cost function is adequately minimized (see figure 3.2), the estimated flow field does not seem to resemble the true flow field at all even in the vicinity of the observing array, as can be seen in figure 3.5 where the true and estimated streamfunction fields are displayed.

In figure 3.6 is shown the scale vector and estimated control vector. The control variables that have been shifted significantly from zero relative to their scales are: the vorticity initial conditions, the low–frequency expansion coefficients on the southern and western boundaries, and the high–frequency expansion coefficients. One can see from figure 3.6 that the flat scaling has allowed the optimization to create variability at high frequencies.
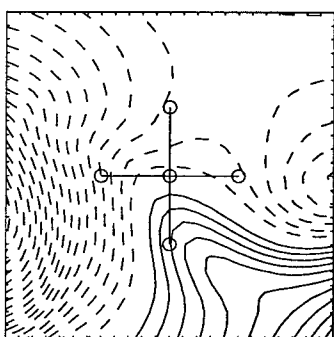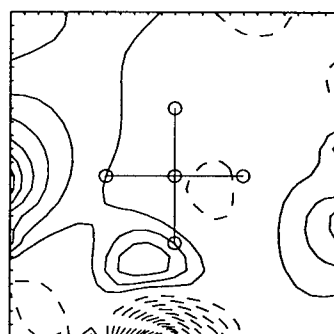
The model/data misfit at the data sampling times (day 1, day 3,..., day 23) is small as the cost function is well minimized. However at time–steps other than
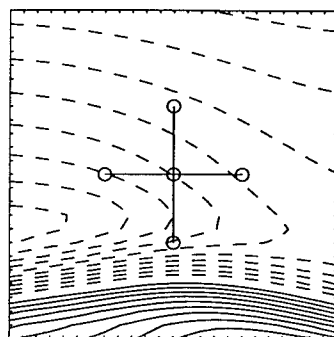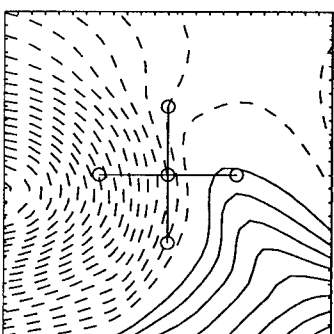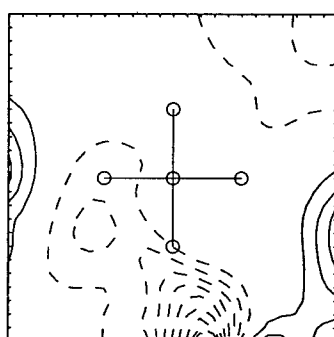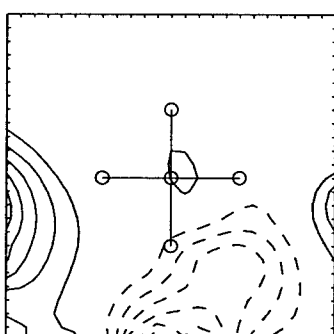
day 0
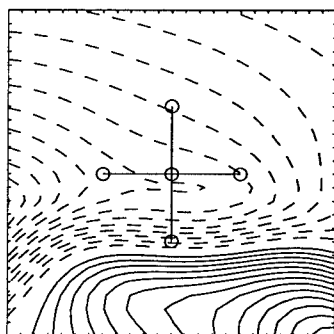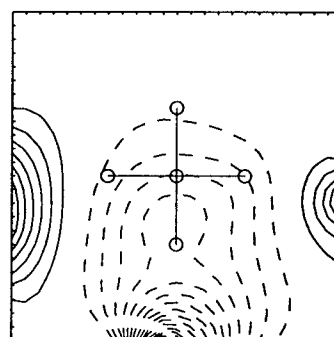
day 8

day 16

day 24

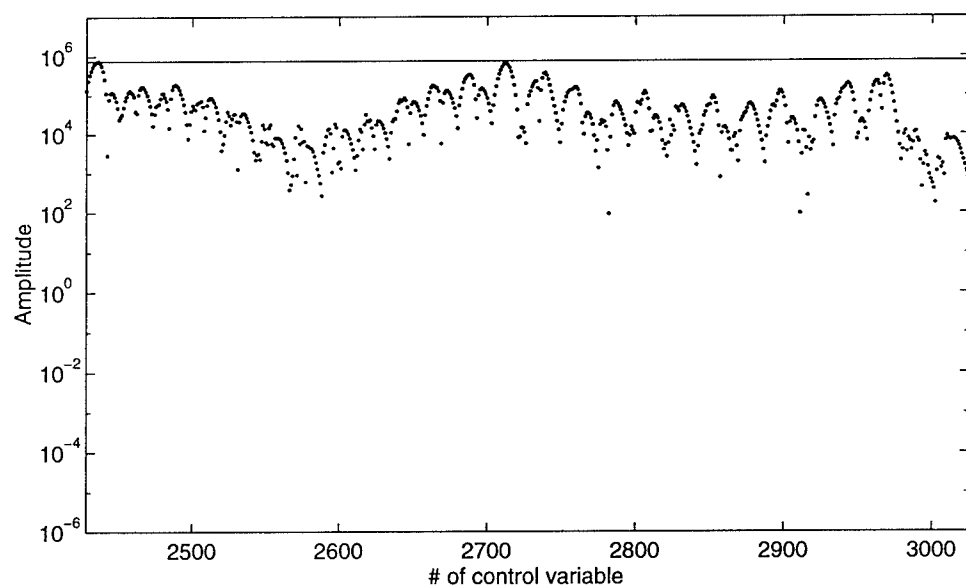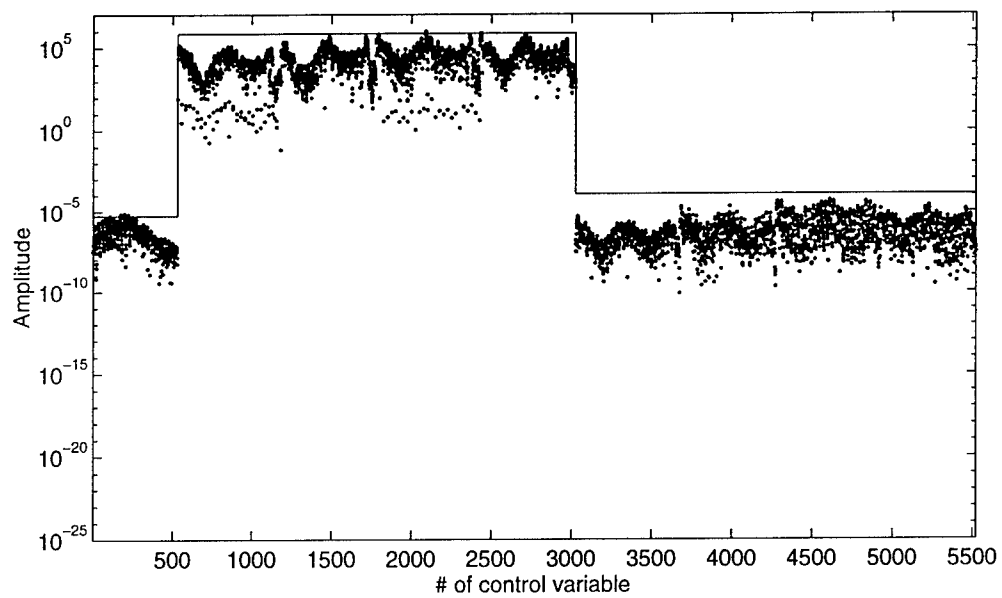Figure 3.5: Same as figure 3.3 but for case B2 which uses a flat scaling.

Figure 3.6: Same as figure 3.4 but for case B2 which uses a flat scaling

the data sampling times, the estimated flow field can be radically different from the true flow field as the estimated high–frequency expansion coefficients have large amplitudes. Since all of the expansion coefficients for boundary streamfunction and vorticity have the same scale, and are zero at the beginning of the optimization, the optimization can efficiently minimize the cost function by varying equally the high and low frequency expansion coefficients. Between successive data sampling times the large amplitudes in the high frequencies can make the estimated flow markedly different from the true flow, which has little variability at high frequencies. This is why the snapshots of the estimated streamfunction field at day 0, day 8, day 16 and day 24 displayed in figure 3.5, do not resemble the true streamfunction fields.

Note that the amplitudes of the estimated control variables are in general much smaller than their scales. Due to the choice of zero as a first guess, most of the control variables have not been moved very far from zero, relative to the scale. This can be seen in figure 3.5 where the estimated streamfunction throughout the sub–domain has a much smaller amplitude than the true streamfunction.

For both case A2 and case B2 the values of streamfunction and vorticity at the corner points of the domain are not shifted much from their *a priori* values of zero, compared to other points on the boundary. This can be seen in figures 3.3 and 3.5 where the estimated streamfunction goes to zero in each of the four corners of the model domain. This is due to the finite–difference formulation of the equations governing streamfunction and vorticity. The five–point Laplacian relating streamfunction to vorticity, and the nine–point Arakawa Jacobian in the prognostic equation, enable streamfunction at all boundary points to feel the presence of vorticity in the interior, except at the corner points. At the corners, streamfunction and vorticity are affected by interior values only through the nine–point Arakawa Jacobian, since the five–point Laplacian does not include the corner points.

Hence the estimates of streamfunction and vorticity at the corners are more dependent on the first guess of the flow field in the vicinity of the corners. For the

zero first guess cases there is no advection on the boundaries at the start of the minimization, so it is difficult for the corner values to change through information being spread by the Jacobian. Better results could be obtained by starting the optimization with a more informed first guess for the control variables.

3.3 Choice of first guess

For an optimization problem with nonlinear constraints, it is possible for the optimal solution to be dependent upon the first guess for the control variables (Gill *et al.*, 1981). For a linear problem it is generally possible to find the global minimum of the cost function, at which the optimally estimated control variables do not depend on their first guess. Nonlinearity can cause the presence of multiple local minima in the cost function. In any gradient–search algorithm the local minimum found depends upon where the search was started from.

The first guess for the control variables that is passed to the minimization routine should thus be chosen to be as close as possible to the true values, on the basis of any *a priori* information available. Using the same approach as in chapter one, experiments are run using first guesses for the control variables that differ in the amount of *a priori* information available. Optimizations with the following first guesses were performed:

(i) zero for all initial and boundary conditions (A2 & B2)

(ii) persistence in time of true initial conditions (C2, D2 & F2)

(iii) true initial and boundary conditions randomly perturbed by 25% (E2)

(iv) persistence in time of objectively mapped initial conditions (G2)

The scaling used for the experiments in this section is the flat scaling used in case B2: a constant value for all streamfunction variables and a constant value for all vorticity variables, that is, no frequency dependence.

3.3.1 Persistence

<u>Case C2</u>: The first guess for the control variables is persistence in time of the true initial conditions. That is, there is no temporal variation in the boundary values of streamfunction and vorticity. Hence the first guess for all expansion coefficients is zero except for the DC components which have their true values. This experiment simulates the realistic situation of having a hydrographic survey at the start of a mooring time series. The optimization performs well compared to the other experiments. The cost is minimized to a lower value, in fewer iterations, than in any other experiment as can be seen in figure 3.2. In figure 3.7 is shown the time series of each of the observed velocities together with the velocities at the same locations produced by the estimated control variables. The fit is quite good in that the residuals between the observed and assimilated velocities in general fall well below the *a priori* velocity error of 4 *cm/sec*.

In figure 3.8 the true and estimated streamfunction fields are shown. By creating temporal variation in the boundary values of streamfunction in the southwest corner, the optimization is able to cause a meander to swing through the array and match the observed velocities. The true and estimated vorticity fields are shown in figure 3.9. In spite of the persistence in time of the vorticity field at the start of the optimization, the assimilation forces the vorticity to have temporal variations at the boundaries, resulting in the good agreement seen between the true and estimated fields at later times.

The estimated control vector and scale vector are shown in figure 3.10. The estimated DC components and the vorticity initial conditions have amplitudes of the order of their scale, as one would expect since they were given their true values as the first guess. The other expansion coefficients are of similar magnitude to those estimated in case B2, except that there is slightly less energy in the 12 day coefficients.

There is however some two–day periodicity in the estimated boundary streamfunction. In figure 3.11 the mean is shown of the estimated streamfunction on the

81
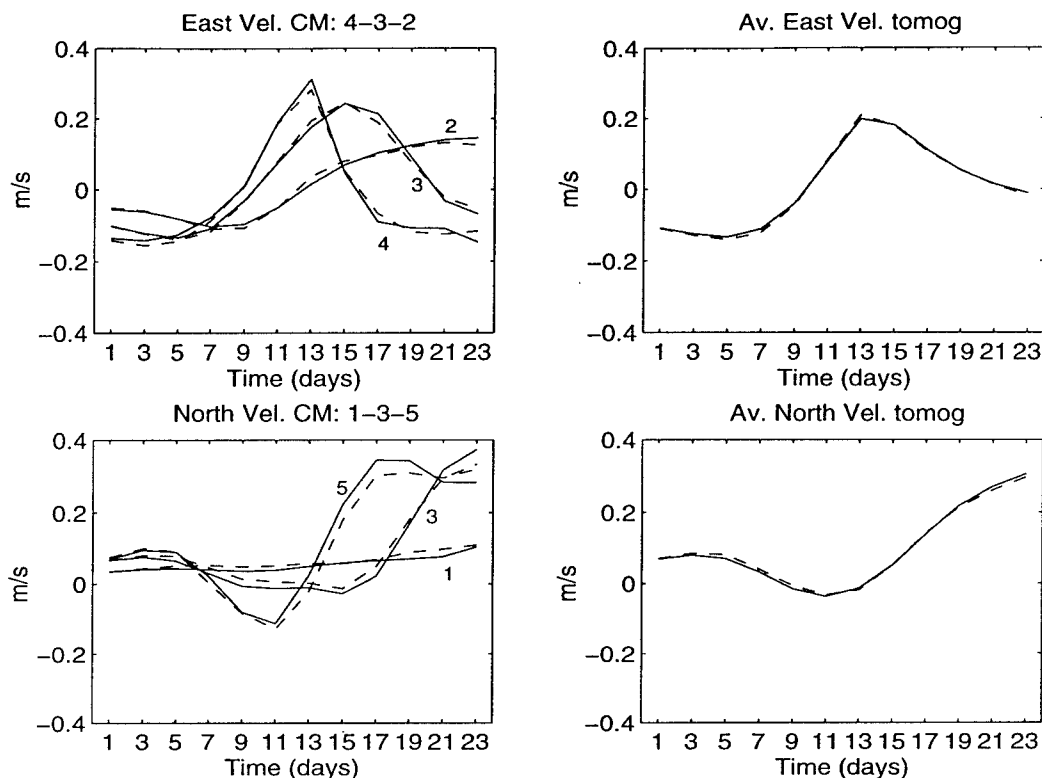
Figure 3.7: Time series of observed velocities (solid) and assimilated velocities (dashed) at the five current meters (left) and between the two pairs of tomographic transceivers (right) for case C2, *a priori* error is 4 cm/sec.

western boundary as a function of time, as well as the mean of the estimated vorticity on the western boundary as a function of time. The "wiggliness" displayed by the streamfunction, and not by the vorticity, is due to the two–day periodicity in the data sampling. The process by which the data sampling period becomes energetic in the estimated boundary streamfunction is explained in the appendix, and further discussed in section 4.3. Essentially it is a consequence of the ellipticity of the Poisson equation for streamfunction.

In an attempt to estimate boundary conditions that resemble more the true boundary conditions, observations of velocity are given at every time-step. In a real assimilation sparsely sampled observations can be interpolated onto every time-step with quite successful results, because for this and many other ocean models the
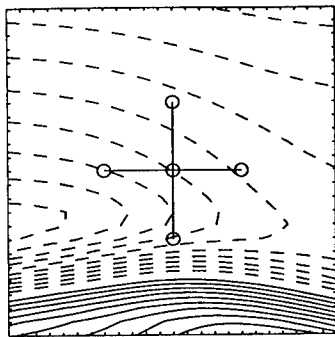
day 0
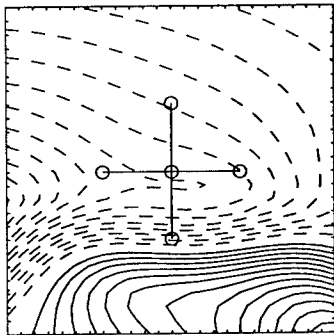
day 8
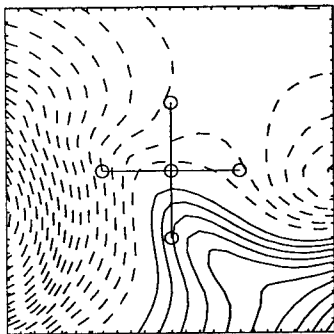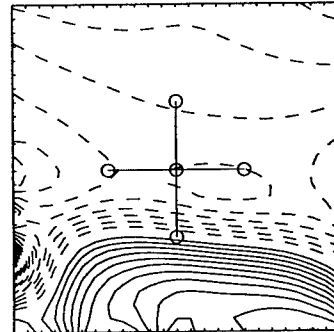
day 16

day 24
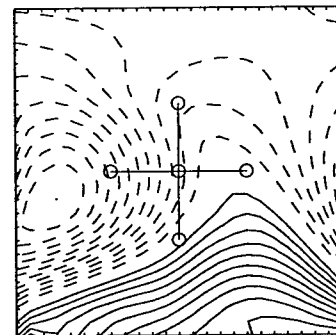
Figure 3.8: Same as figure 3.5 but for case C2 which uses persistence in time of the true initial conditions as the first guess.

83
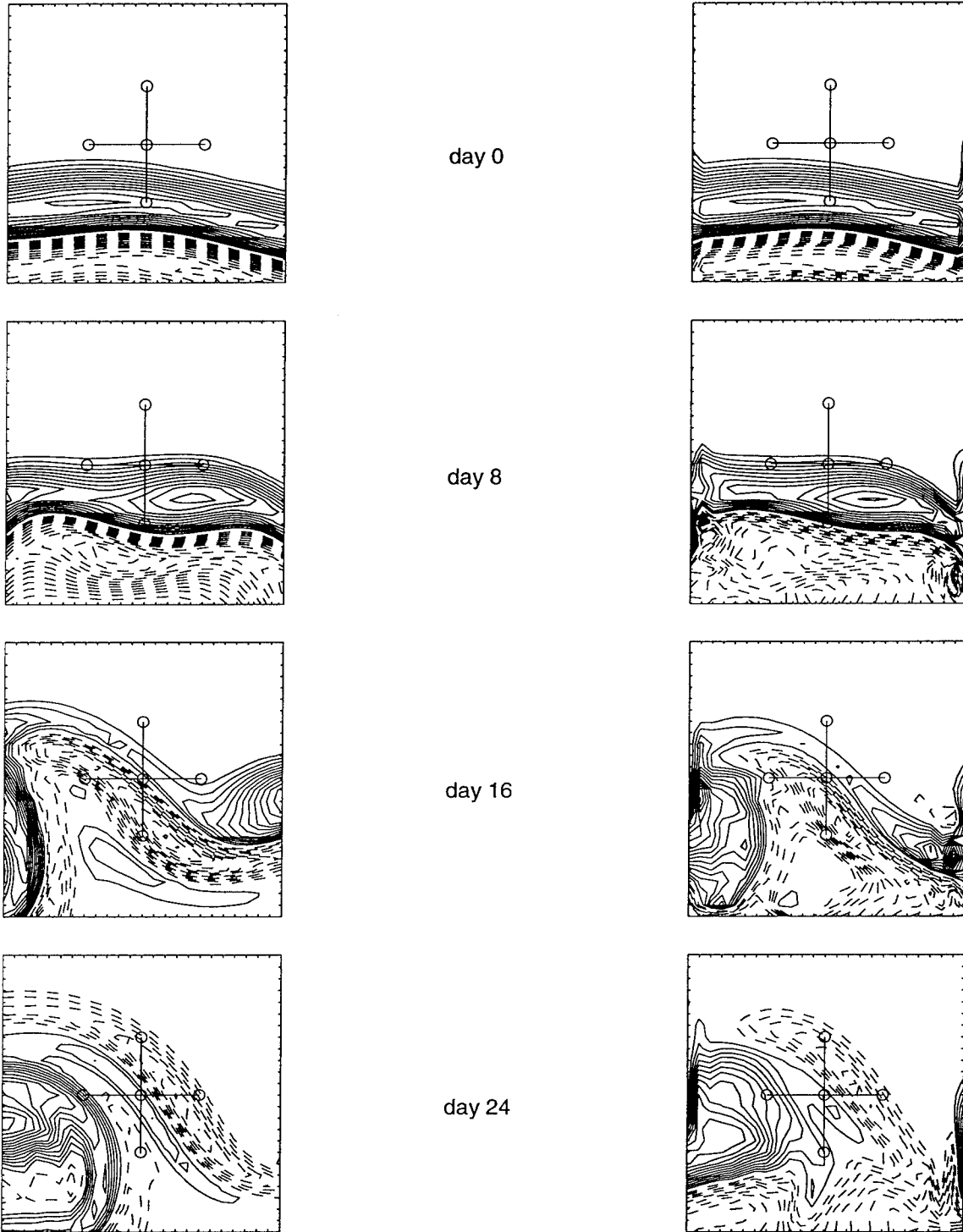
Figure 3.9: Vorticity every 8 days for (left) the true flow field and (right) the estimated flow field for experiment C2 which uses persistence in time of the true initial conditions as the first guess for the control variables. (C.I.= 10^{-6} s^{-1})
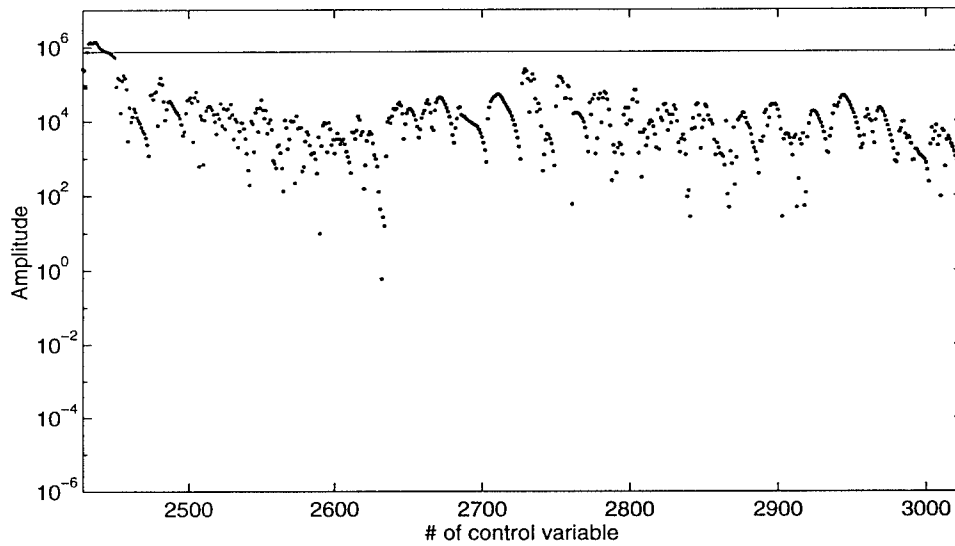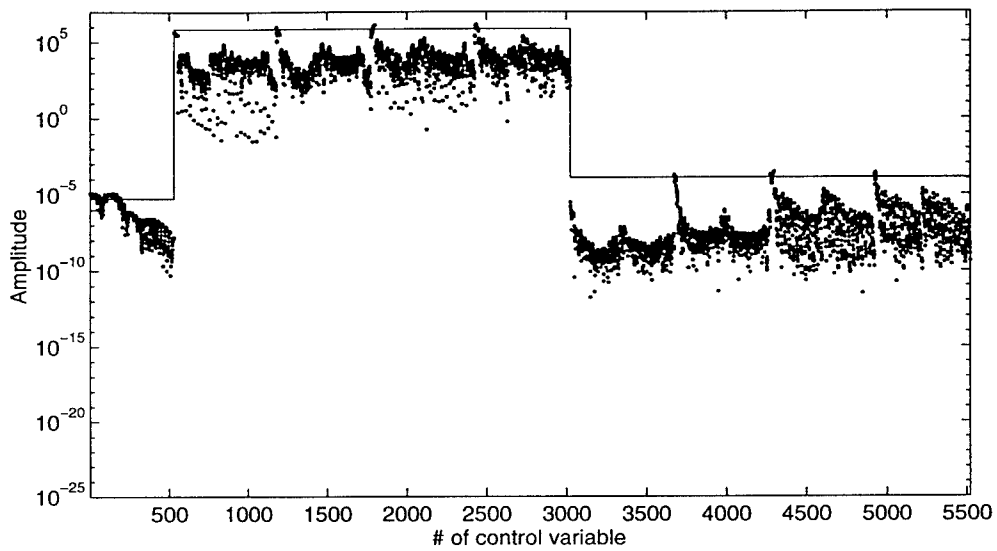
Figure 3.10: Same as figure 3.6 but for case C2 which uses persistence in time of the true initial conditions as the first guess.

Figure 3.11: The mean streamfunction (Top) and mean vorticity (Bottom) on the western boundary as a function of time, taken from the estimated control variables for case C2.

variability of interest is at time scales much longer than two days. The disadvantage of doing this is that the number of data points increases and strictly they can no longer be treated as independent of each other. This has important consequences for the error estimation in the next chapter.

<u>Case D2</u>: The same first guess and scaling for the control variables are used as in case C2, but here there are observations supplied at every time–step. The optimization performs well (see figure 3.2), and the minimization is very similar to that of case C2.

For this case the optimization finds a minimum in fewer iterations than in case C2 (see figure 3.2). The high–frequency components of the gradient vector have much less amplitude in case D2, because the forcing in the adjoint equations is smoother in time. Hence in the course of the minimization the norm of the gradient vector is smaller, and the minimization stops sooner, than in case C2. This result indicates that the contours of the cost function (in the space spanned by the control vector) are smoother when there is data at every time–step compared to data at every 48th time–step.

The estimated streamfunction field for case D2 shown in figure 3.12 looks very similar to the estimated streamfunction field for case C2 shown in figure 3.8. The scale vector and estimated control vector for case D2 are shown in figure 3.13. Note that there is little variability in the estimated high–frequency expansion coefficients. The frequency dependence of the magnitudes of the estimated expansion coefficients has a red character, which is desirable as the spectral density of the true boundary conditions is red.

The final value of the cost function is higher than in case C2, yet still less than one. The cost function is minimized to a smaller value in case C2 because there is less data for the same number of control variables. Hence there are relatively more degrees of freedom in fitting the control variables to the data in case C2.

day 0

day 8

day 16

day 24
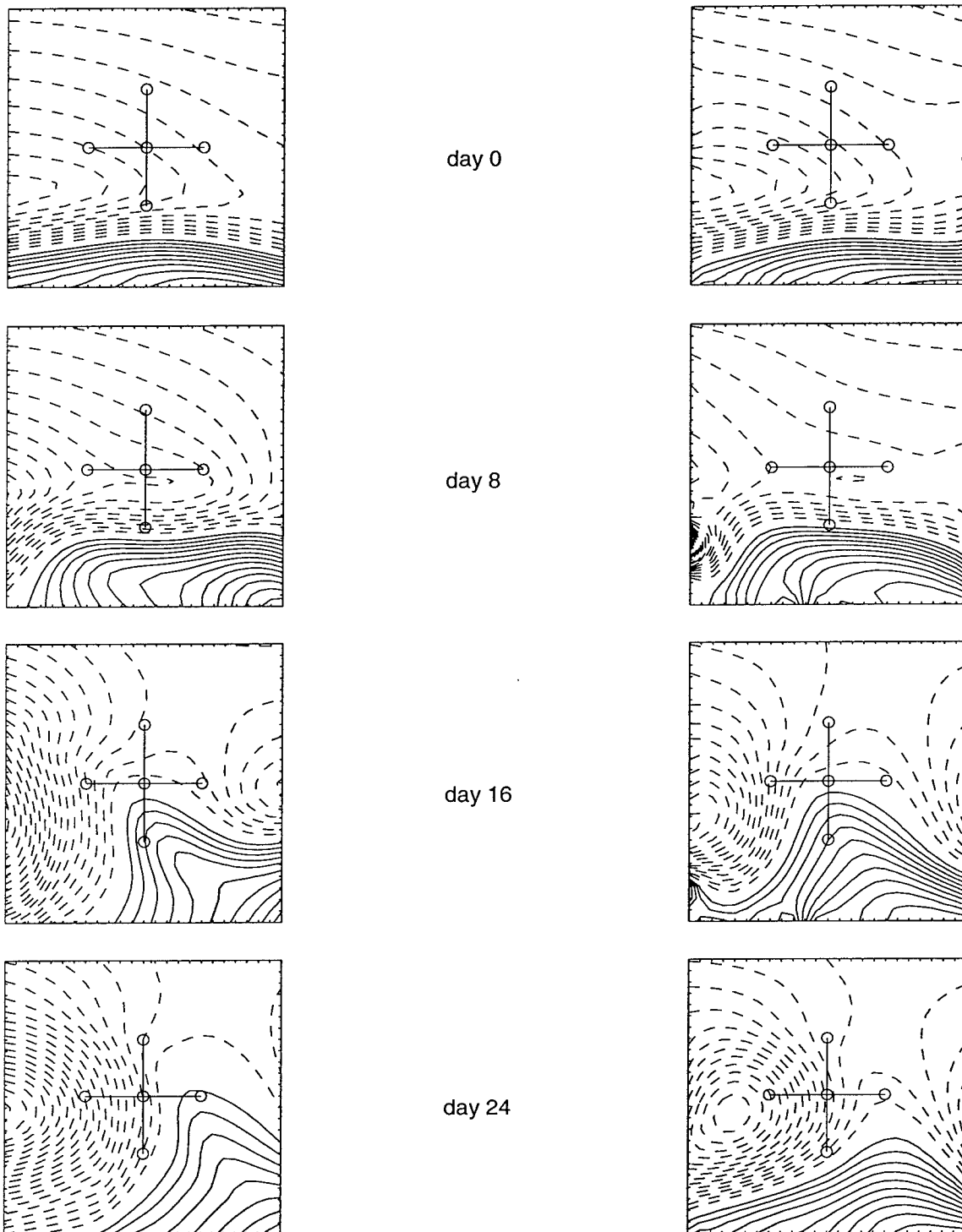
Figure 3.12: Same as figure 3.8 but for case D2 which has data at every time–step instead of every 48 time–steps.
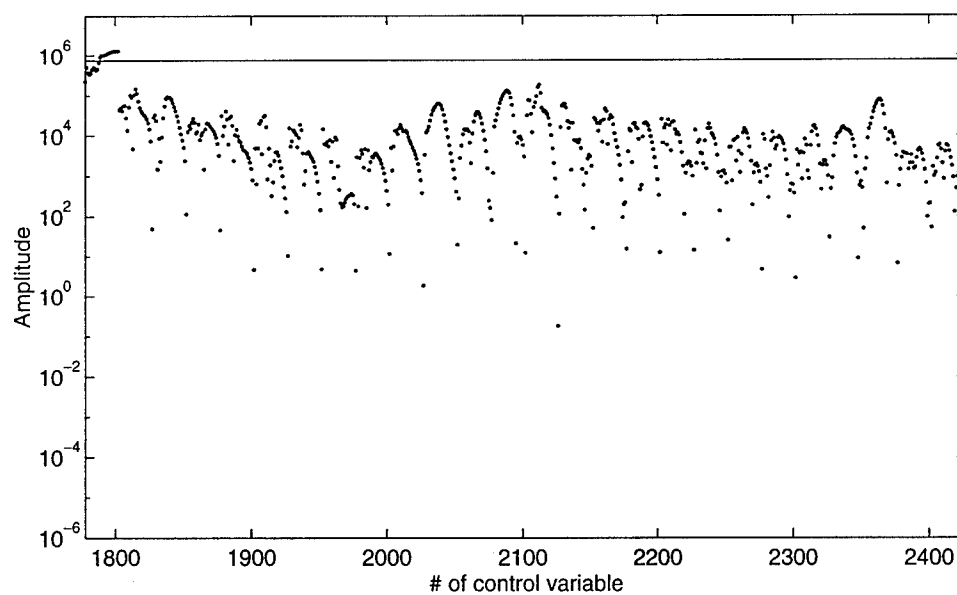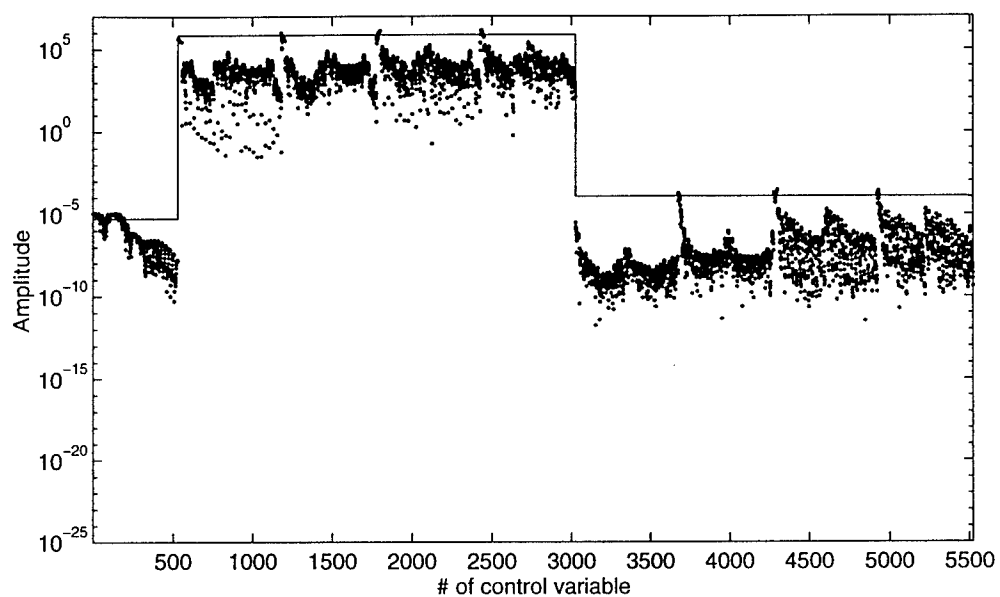
Figure 3.13: Same as figure 3.10 but for case D2 which has data at every time–step instead of every 48 time–steps.

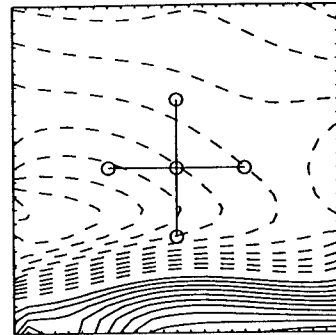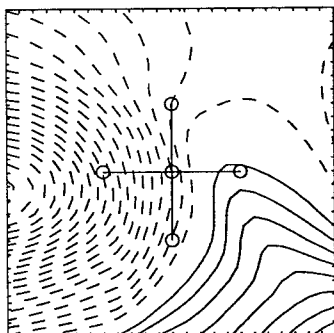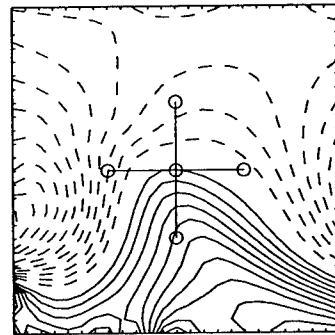In figure 3.14 the mean is shown of the estimated streamfunction on the western boundary as a function of time, as well as the mean of the estimated vorticity on the western boundary as a function of time, for comparison with figure 3.11.

As it can be seen, the two–day variability in the estimated boundary streamfunction is not present for case D2. The estimated boundary streamfunction jumps at observation times. For case C2 these jumps are at day 1, day 3,..., day 23. For case D2 there are no jumps as every time–step is an observation time. At grid–points where the model equations are evaluated, jumps in the streamfunction field at the observation times are smoothed in time by the dynamics itself. In the finite–difference formulation of the forward and adjoint model equations used here, the model equations are not evaluated directly at the boundary points. Hence the jumps in the boundary streamfunction are not smoothed in time by the dynamics acting as an interpolater. This phenomenon is further discussed in section 4.3, and is explained in in terms of the adjoint model equations in the appendix.

The estimated boundary vorticity is not sensitive to the sampling interval of the data. The boundary vorticity only influences the model counterparts of the data by being advected through the interior by the prognostic vorticity equation. Unlike the boundary streamfunction, the boundary vorticity does not influence the model/data misfit instantaneously at observation times. The mean of the estimated boundary vorticity as a function of time is shown to be quite similar in both case C2 and D2 as the data provide the same information.

3.3.2   Adding noise

In the two experiments of the last section, the vorticity initial conditions and the velocity observations were assumed to be perfectly known. In this section noise is added to the first guess and then to the velocity observations, so as to render the experimental set–up more realistic.
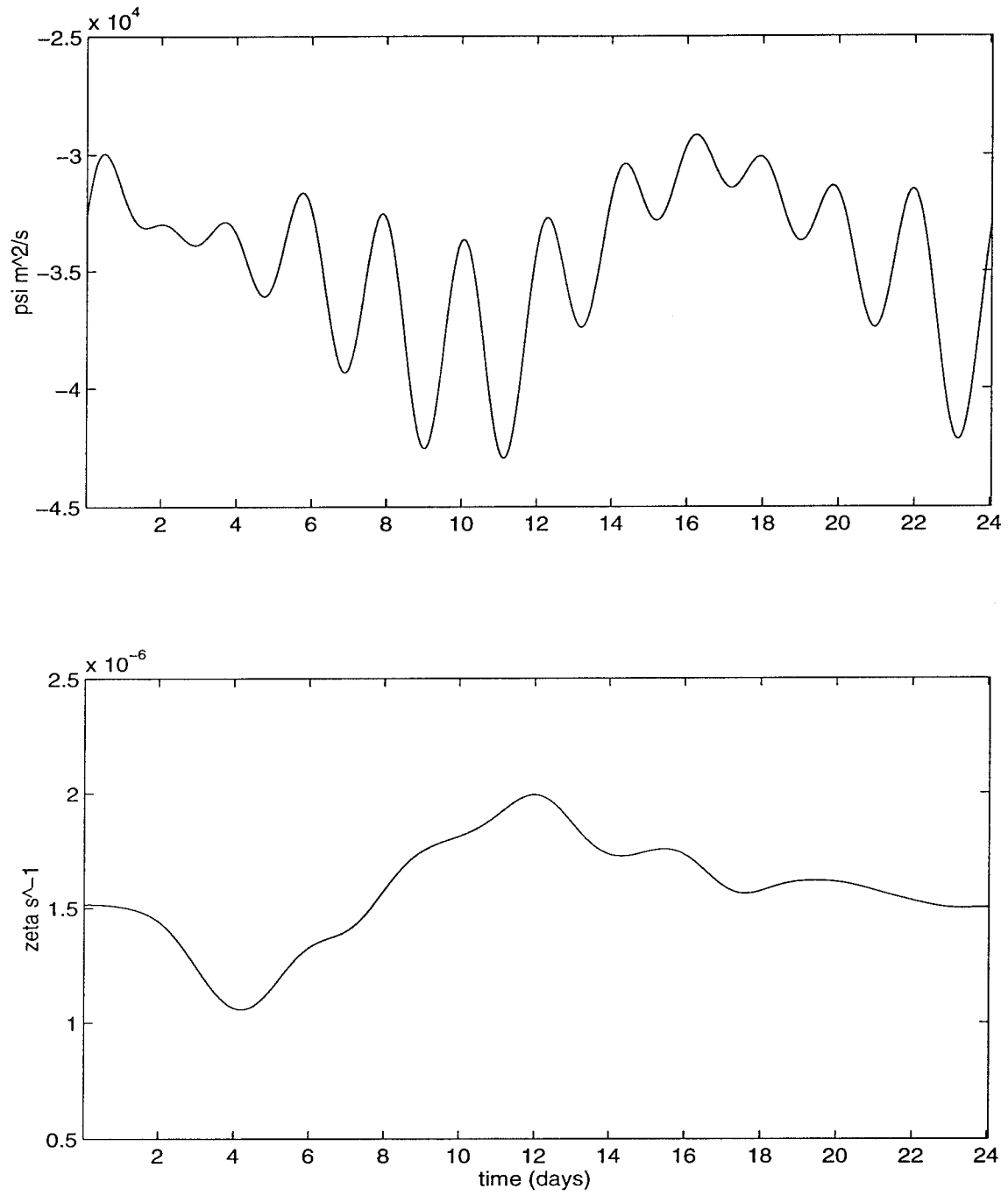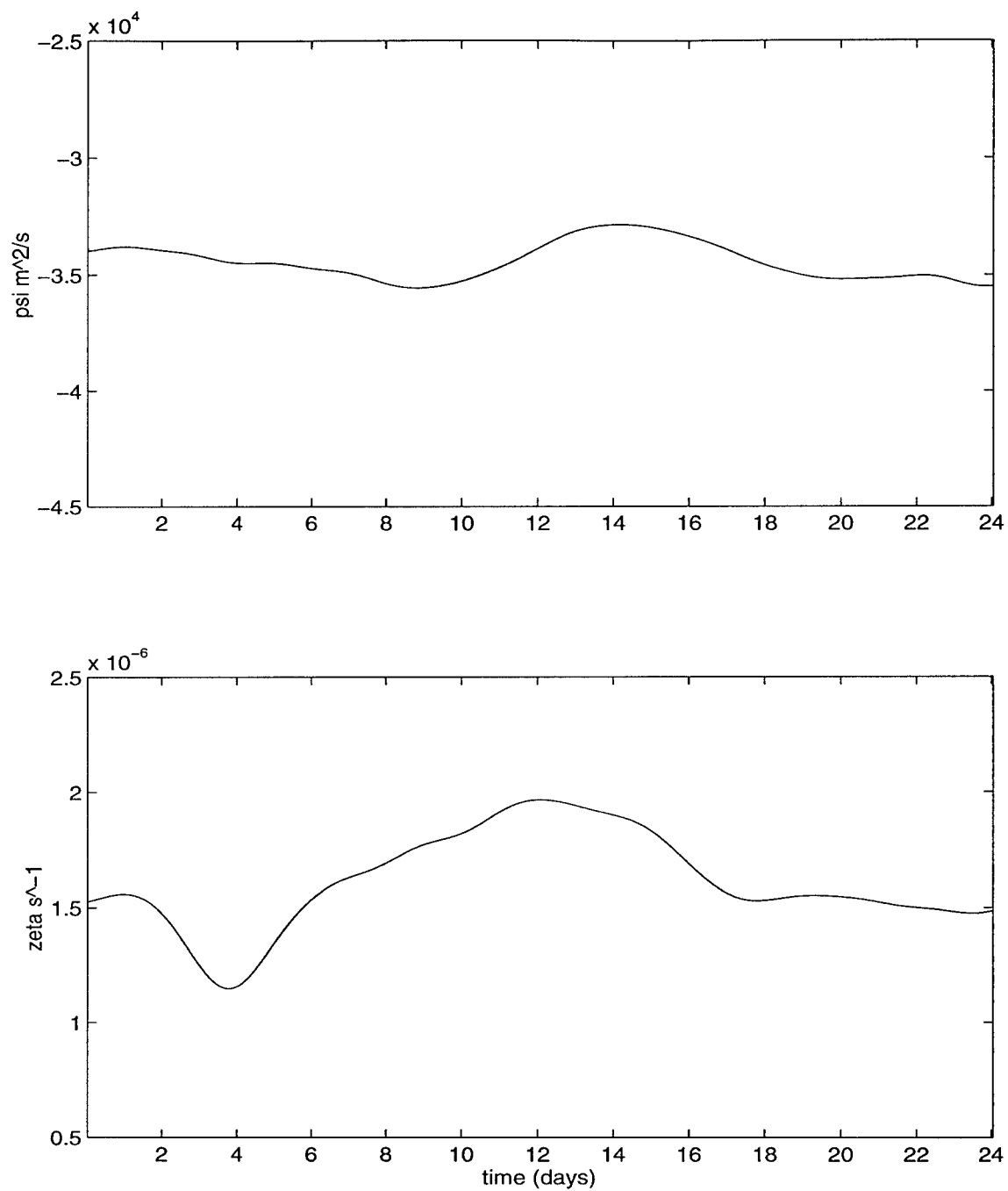
Figure 3.14: The mean streamfunction (Top) and mean vorticity (Bottom) on the western boundary as a function of time, taken from the estimated control variables for case D2.

91

<u>Case E2</u>: Here the first guess for the control variables is chosen by randomly perturbing the true initial and boundary conditions by 25 percent. This is similar to how first guesses for the control variables were chosen by Seiler (1993). More than for any other experiment presented here, the first guess for the initial and boundary conditions is closest to their true values. Although in case C2 persistence of the true initial conditions was used as a first guess, that first guess did not contain any of the temporal variability associated with the meander event.

The optimization minimizes the cost function well, in much the same manner as case C2 and case D2, as shown in figure 3.2. Note that the final values of the cost function for cases D2 and E2 are larger than the final value of the cost function for case C2. When the data is sampled at every time–step (D2 and E2), the mean–square residual of the model/data misfit tends to be larger than when the data is sampled at every 48th time–step.

The estimated streamfunction field well resembles the true streamfunction field as can be seen in figure 3.15. Figure 3.16 shows an example of how the optimization changes the values of the control variables away from their first guess to be more similar to the values of the true control variables. Plotted is the streamfunction and vorticity at $t = 0$ along the western boundary. One can see that the first guess (dotted) has been varied towards the true values (solid) in the course of the optimization, resulting in the estimate (dotdash) when the minimum is found. This is probably due to the smoothness term in the cost function, which penalizes the second derivative of streamfunction and vorticity around the boundary.

Randomly perturbing the true values of the control variables by 25 percent as a choice of first guess is not generally useful. This type of first guess can only be used in the context of twin experiments where the true values are known. Case E2 is presented here as a connection to Seiler's study. Also, case E2 shows how the adjoint method can force the control variables towards their true values when the optimization is started near the true values. This may seem an obvious point, but in

92
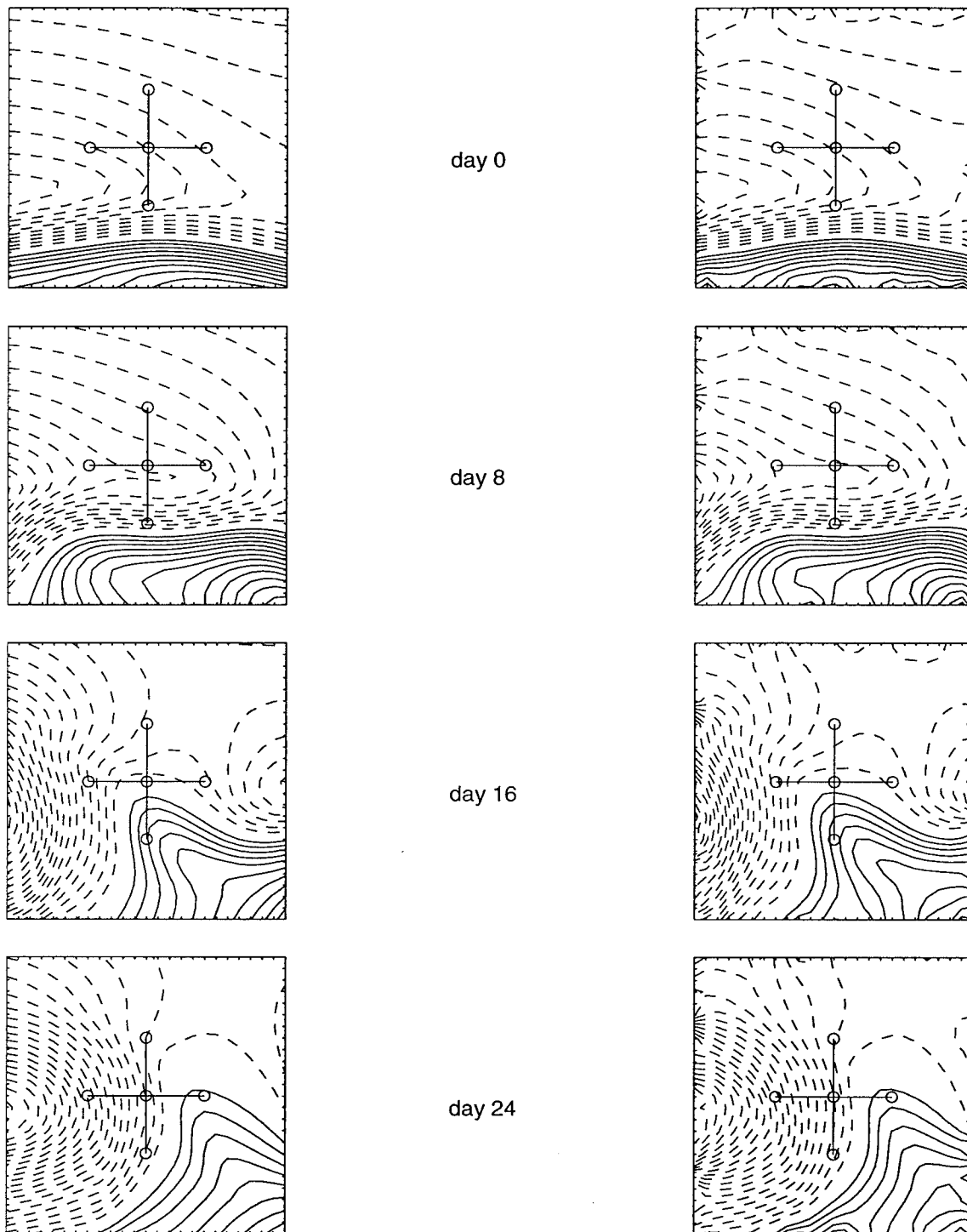
Figure 3.15: Same as figure 3.12 but for case E2 which uses the true initial and boundary conditions randomly perturbed by 25 percent as the first guess.
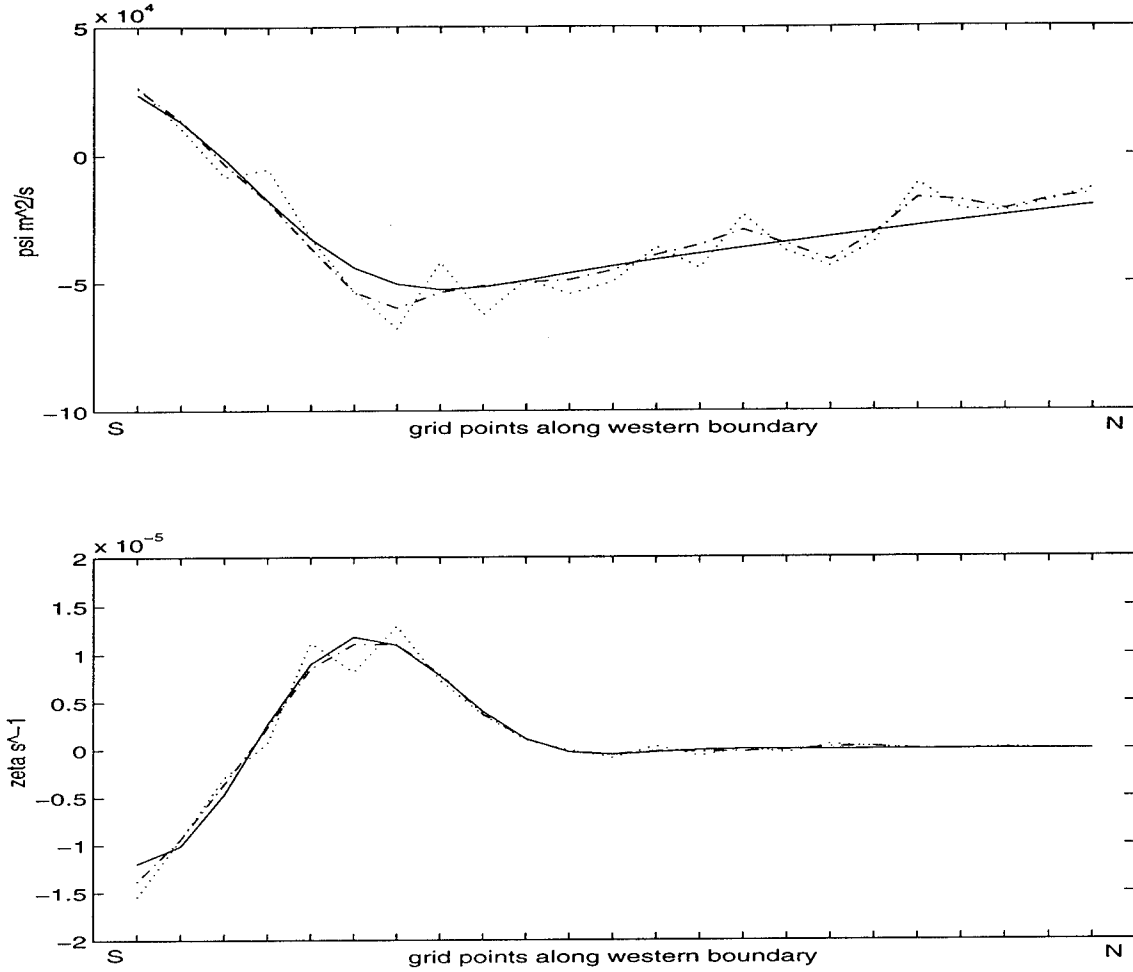
Figure 3.16: Case E2, plotted are values of (top) streamfunction and (bottom) vorticity along the western boundary at t=0, north is to the left, (solid) True, (dotted) First guess and (dotdash) optimal estimate.

all of the other cases the control variables are not forced towards their true values. The optimization in each case finds the local minimum nearest to where minimization is started from.

Case F2: This case keeps all the same experimental parameters as for case C2, except that noise is added to the observations. The observational noise is taken from a normally distributed random number generator with a standard deviation of 4 cm/s, which is the *a priori* error in all of the velocity observations in this study.

The estimated flow field is very similar to the estimated flow field for case C2 shown in figure 3.8. The cost function is well minimized (see figure 3.2) although not to as low a value as in case C2 where perfect observations of the true flow field were available. The velocity time–series at the observing array are shown in figure 3.17. The true velocities (solid), the estimated velocities (dashed), and the noisy observed velocities (dotted) are plotted together, in separate frames for each current meter and the tomography. An errorbar of 4 cm/s is located in the upper right corner of each frame. The optimization has successfully reduced the size of the residuals between the estimated and true velocity curves to the order of the *a priori* error.

3.3.3   Simulated hydrography

For a model/data assimilation using real data, a first guess for the initial and boundary conditions would be constructed from a hydrographic survey or from climatology. For these choices of first guess, the streamfunction and vorticity values from the survey or climatology need to be mapped onto the grid–points of the model sub–domain. Case G2: To simulate the scenario where one has sparse observations of temperature and salinity from a hydrographic survey, sparse observations are taken of the true streamfunction field at the initial time. These streamfunction observations are then objectively mapped onto the grid–points of the model sub–domain, and the initial vorticity is calculated from the mapped streamfunction field.

Objective mapping, or objective analysis, is a common means of interpolating irregularly spaced data onto a regular grid. Bretherton *et al.* (1976) give details of this method, which is based upon Gauss–Markov theory. Hogg (1993, 1994) applied objective mapping to the SYNOP East dataset to spatially interpolate temperature, salinity and velocity observations taken at the observing array.

The locations at which observations of streamfunction are taken are shown in figure 3.18, along with the objectively mapped streamfunction field over the model sub–domain. The observing locations are 100 km (five grid–points) apart. An
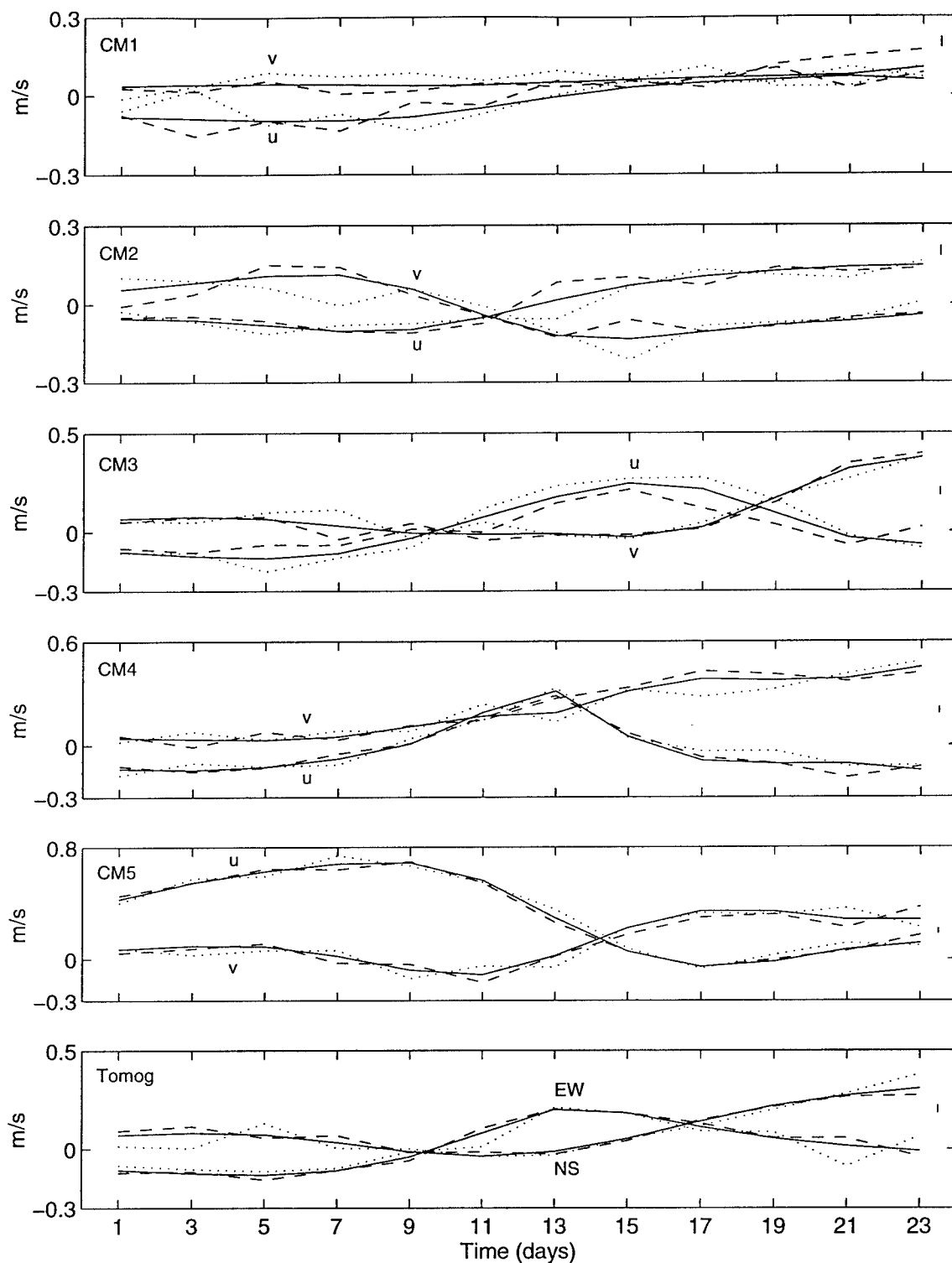
Figure 3.17: Time–series of eastward velocity, u, and northward velocity, v, at the five current meters and the east–west and north–south tomographic averages. (Solid) True velocities, (Dashed) estimated velocities and (Dotted) true velocities with noise added, for case F2 are shown. An errorbar of 4 cm/s is located on the right–hand side of each frame.

96
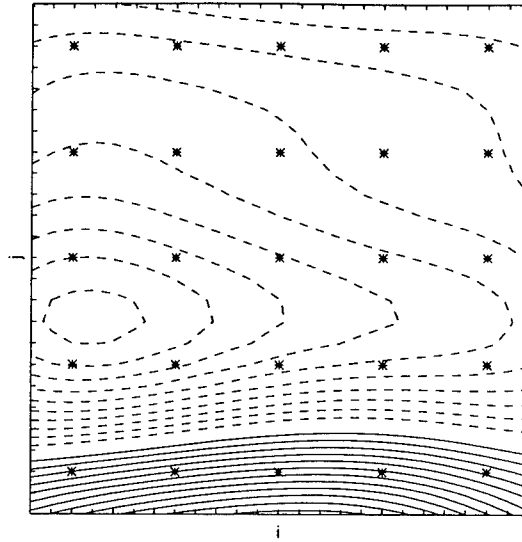
Figure 3.18: The objectively mapped streamfunction field used as a first guess for the initial conditions for case G2 (C.I.=5000 m^2/s). The observing locations are marked by asterisks.

isotropic gaussian spatial covariance function with a length–scale of 200 km is used in the objective mapping, and the uncertainty in the streamfunction observations is assumed to be ten percent of the total rms variability of the streamfunction field. These parameters are of great importance to the mapping. Here they are given rather arbitrary values, but for a real model/data assimilation more informed choices could be made (Hogg, 1993). The resemblance of the mapped streamfunction field to the true streamfunction field may be seen in the upper left frame of figure 3.19.

The vorticity field is calculated from the mapped streamfunction to provide the first guess for the vorticity initial conditions for this experiment. Persistence in time of the boundary values of the mapped streamfunction and vorticity is used as the first guess for the boundary conditions.

An important issue that arises at this stage is the choice of *a priori* covariance matrix for the control variables, which sets the scaling for the control variables in the optimization. The objective mapping produces expected error covariance maps for both streamfunction and vorticity, and these could be used to assign *a priori*

97

covariances to the vorticity initial conditions. The expected error covariances for the vorticity field that are calculated from the expected error covariances for the mapped streamfunction are very large, even when the error in the streamfunction field is relatively small, because the errors are magnified by the Laplacian relating streamfunction to vorticity. For large *a priori* variances in the initial and boundary vorticity, the optimization may estimate large vorticity values that cause the forward model to become numerically unstable.

For this experiment the *a priori* covariances for the control variables are initialized to the same values as in case C2. The objective mapping is used to construct streamfunction and vorticity fields to be used as a first guess for the initial and boundary conditions, and the error covariance estimates from the objective mapping are not utilised. Further experiments would investigate the applicability of the objective mapping error covariances to a time–dependent model/data assimilation. It is not clear at this stage how one would select the *a priori* covariances for the time–dependent boundary conditions. A main purpose of this study is to examine the improvement that assimilation of interior data with strongly nonlinear dynamics gives to estimated boundary conditions, so a simple form for their *a priori* covariances is chosen as a first step.

The true and estimated streamfunction fields are shown in figure 3.19, and the minimization of the cost function performs very similarly to case F2 (see figure 3.2). As with the other experiments in this chapter the optimization is able to vary the boundary streamfunction and vorticity away from persistence and to cause a meander to swing through the observing array. The good performance of this experiment bodes well for the assimilation of the SYNOP Eastern Array velocities, with the first guess for the control variables taken from the initial hydrographic survey.

The results of this chapter show that for the experimental setup used here there are many local minima of the cost function, that depend upon the first guess
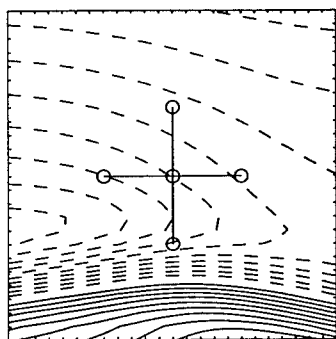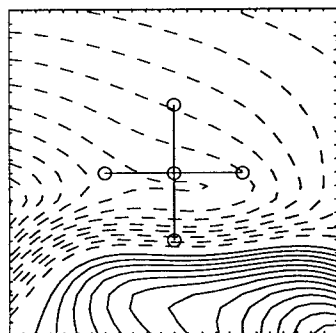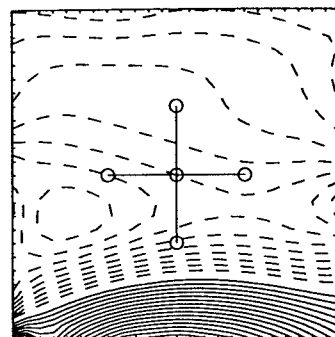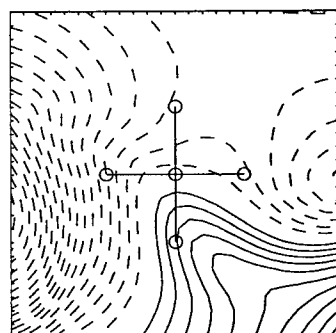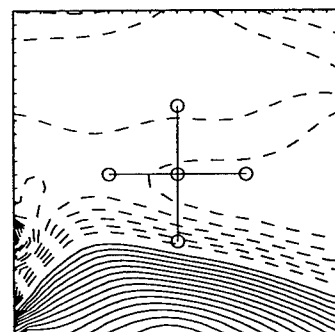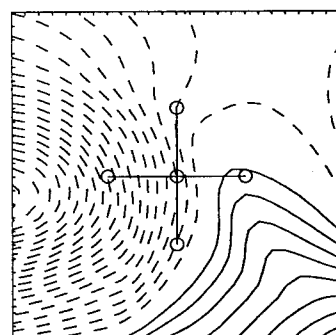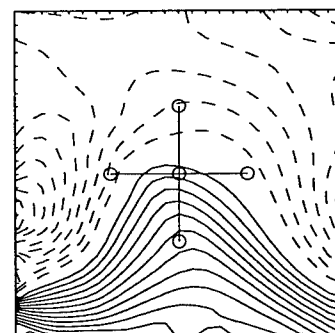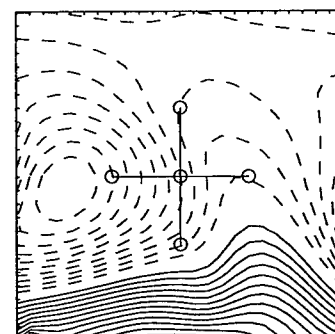
Figure 3.19:   Same as figure 3.8 but for case G2 for which there is noise added to the velocity observations, and the first guess for the vorticity initial conditions is taken from an objective mapping of a simulated hydrographic survey of streamfunction.

99

for the control variables. Further comparisons between the cases will be presented in the next chapter.

For actual observations, case G2 is the most likely scenario that would be used to assimilate data into a model. In the real world, one is likely to have a snapshot of the ocean state from a hydrographic survey followed by time–dependent sparse observations such as mooring time series, as in the SYNOP Eastern Array dataset. Case C2 may be regarded as the most successful of the twin experiments in the sense that the cost function is minimized to the smallest value, the first guess and scaling are chosen using reasonable and realistic assumptions, and the data is sparse in space and time.

Chapter 4

Quality of the estimated boundary conditions

The quality of the fit of the estimated control variables to the velocity observations is examined in this chapter. First the residuals of the state variables and control variables with their true values are presented, in the context of the twin experiments. Then the results of case C2 are used to calculate the sensitivity and Hessian matrices. The sensitivity matrix is used to investigate the sensitivity of the estimated control variables to the observations. The processes by which information is spread during the optimization are discussed. The estimated error variances for the control variables are calculated from the inverse Hessian using the sensitivity matrix method that was described in chapter two. Finally, error maps for the interior streamfunction and vorticity fields are constructed.

The novel results of this chapter are the estimation of errors for streamfunction and vorticity, at all boundary points and all interior points at all times, when the dynamics are strongly nonlinear.

4.1 Comparison with true values

The use of twin experiments allows a comparison of any feature of the estimated flow field with that of the true flow field. Some measures of the difference between the true flow field and the estimated flow field are now presented. The error measures are expressed in terms of a normalized rms residual.

When these error measures are of order one, the mean–square residual between the estimates and their true values is of the same order as the variance in the true values, indicating that the estimates are as close to the true values as would be any other realization of the flow field. When the normalized rms residual is less than one, one can say that the estimates are probably closer to the true values than some other realization of the flow field. In the following expressions, ψ_{ij}^t, ζ_{ij}^t are the true values and $\hat{\psi}_{ij}^t$, $\hat{\zeta}_{ij}^t$ are the estimated values of the streamfunction and vorticity respectively. The total streamfunction error:

$$\mathcal{E}_{Ts} = \left[\frac{\sum_{i,j,t} \left(\hat{\psi}_{ij}^t - \psi_{ij}^t \right)^2}{\sum_{i,j,t} \left(\psi_{ij}^t \right)^2} \right]^{\frac{1}{2}}$$

where the summation is over all interior points $(i = 2, \ldots, n - 1$ and $j = 2, \ldots, m - 1$) and for all $t = 0, \ldots, T$.

The total vorticity error

$$\mathcal{E}_{Tv} = \left[\frac{\sum_{i,j,t} \left(\hat{\zeta}_{ij}^t - \zeta_{ij}^t \right)^2}{\sum_{i,j,t} \left(\zeta_{ij}^t \right)^2} \right]^{\frac{1}{2}}$$

where the summation is over all interior points and for all $t = 1, \ldots, T$.

The boundary streamfunction error

$$\mathcal{E}_{bs} = \left[\frac{\sum_{b,t} \left(\hat{\psi}_b^t - \psi_b^t \right)^2}{\sum_{b,t} (\psi_b^t)^2} \right]^{\frac{1}{2}}$$

The boundary vorticity error

$$\mathcal{E}_{bv} = \left[\frac{\sum_{b,t} \left(\hat{\zeta}_b^t - \zeta_b^t \right)^2}{\sum_{b,t} (\zeta_b^t)^2} \right]^{\frac{1}{2}}$$

Experiment	$\mathcal{E}_{T_s}$	$\mathcal{E}_{Tv}$	$\mathcal{E}_{bs}$	$\mathcal{E}_{bv}$	$\mathcal{E}_{iv}$
A2	0.79 (1.00)	1.31 (1.00)	0.81 (1.00)	1.09 (1.00)	0.91 (1.00)
B2	0.96 (1.00)	1.05 (1.00)	0.99 (1.00)	1.03 (1.00)	0.97 (1.00)
C2	0.36 (0.64)	0.63 (0.96)	0.43 (0.41)	1.03 (1.07)	0.02 (0.00)
D2	0.33 (0.64)	0.69 (0.96)	0.43 (0.41)	1.04 (1.07)	0.01 (0.00)
E2	0.06 (0.21)	0.21 (0.44)	0.11 (0.18)	0.20 (0.29)	0.26 (0.26)
F2	0.46 (0.64)	0.68 (0.96)	0.62 (0.41)	1.05 (1.07)	0.03 (0.00)
G2	0.53 (0.89)	0.82 (1.18)	0.66 (0.61)	0.95 (1.02)	0.66 (0.66)

Table 4.1:   Error measures. The values in parentheses are the error measures for the streamfunction and vorticity fields resulting from the first guess for the control variables.

where the summation is over the points along all four boundaries and over all time–steps.

The initial vorticity error

$$\mathcal{E}_{iv} = \left[\frac{\sum_{i,j} \left(\hat{\zeta}_{ij}^0 - \zeta_{ij}^0 \right)^2}{\sum_{i,j} \left(\zeta_{ij}^0 \right)^2} \right]^{\frac{1}{2}}$$

where the summation is over all interior points.

These error measures are displayed in table 4.1, for the experiments of chapter three. $\mathcal{E}_{bs}$, $\mathcal{E}_{bv}$ and $\mathcal{E}_{iv}$ are all measures of the error in the estimated control variables relative to the true control variables. $\mathcal{E}_{T_s}$ and $\mathcal{E}_{Tv}$ are called measures of error in the estimated state variables relative to their true values. State variables are model variables, not included in the control vector, whose values depend on the control variables. Shown in parentheses are the error measures at the start of the assimilation. These are the errors in the flow field resulting from the first guess for the control variables.

The streamfunction errors are all less than the vorticity errors. One reason for this is that the streamfunction field is more readily adjusted during the assimilation than the vorticity field, due to the ellipticity of the Poisson equation (this point is illustrated further in the next section). Another reason for the streamfunction errors being lower than the vorticity errors is that the vorticity field has shorter length scales of variability compared to the streamfunction field (see figure 1.1). The fine structure of the estimated vorticity field, as one moves away from the observing array, may differ substantially from that of the true vorticity field.

The total errors and the boundary and initial errors for case A2 and case B2 are all of order one, indicating that the estimated streamfunction and vorticity fields throughout the domain are not at all similar to the true fields. This was already glimpsed in the streamfunction snapshots in figures 3.3 and 3.5. Although the cost function is minimized to a sufficiently low value, so that the velocity error at the observing array is of the order of the *a priori* error, the similarity between the estimated and true flow fields decreases as one moves away from the observing array. Zero was the first guess for all of the control variables for both of these cases. This is obviously a poor choice, so it is hardly surprising that the residuals are of the order of the true variability.

For cases C2 and D2, where persistence in time of the true initial conditions is used as a first guess, the total errors are improved somewhat but the boundary errors are of the order of the boundary errors for the first guess. The first guess for these cases has a stationary jet entering the domain through the southwest corner, and leaving through the southeast corner. The boundary values of streamfunction and vorticity near the inflow may be varied effectively in the optimization in order that the velocities observed downstream of the inflow, at the observing array, agree well with the true velocities. Thus information from the model/data misfit at the array is spread through some of the domain, somewhat reducing the total errors from their first guess values. The estimated boundary values are changed away from their

first guess mainly in the vicinity of the inflow, and they are not forced to resemble the true values elsewhere around the boundary. This last point is illustrated further in the next section when the sensitivity matrix is examined.

For all cases the error in the estimated vorticity initial conditions does not decrease from the error for the first guess. As was found in chapter one, the optimization preferentially fits the strongest signals in the observations which, in the experiments presented here, is the meander event that swings through the observing array at later times. The time–dependent boundary values have more influence on the meander event than do the initial conditions, hence the optimization preferentially varies the boundary conditions.

The total errors for each case as a function of time are shown in figure 4.1. The strong two–day periodicity in the estimates from cases B2, C2, F2 and G2 is readily apparent. Also apparent is the increase in error with time for cases C2 and D2, as the flow field evolves away from the initial conditions (which are given their true values at the start of the optimization).

The only difference between the experimental set–up for case C2 and case D2 is that in case D2 there is data at every time–step whereas case C2 has data at every 48th time–step. One would thus expect lower error measures for case D2 as there is more data available. From the error measures shown in table 4.1 and figure 4.1, it can be seen that the only significant difference between the two cases is that the total streamfunction error for case D2 does not contain the two–day variability seen in case C2. The availability of the extra data does not improve the assimilation because: (i) Most of the variability in the true field and in the velocity observations is at periods greater than two days (see figure 3.7), so sampling the true field every hour instead of every two days does not supply more information in the optimization. (ii) The extra data points in case D2 are taken at the same locations of the data points in case C2. The temporal and spatial coverage of the data is effectively the same in both cases, thus their error measures are similar.

105
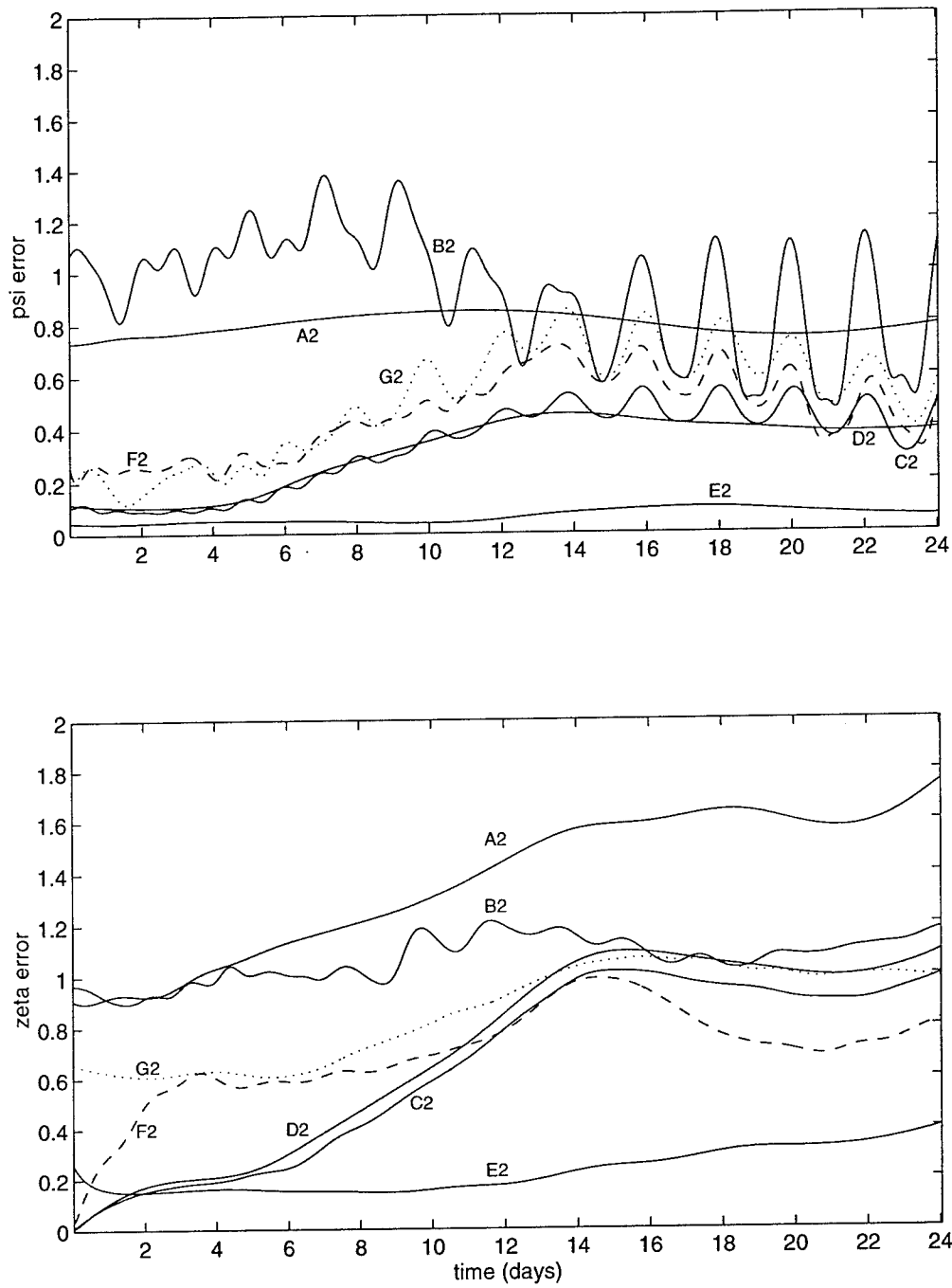
Figure 4.1: Total errors for each experiment as a function of time, (top) $\mathcal{E}_{Ts}$ and (bottom) $\mathcal{E}_{Tv}$.

For case E2, one can see from table 4.1 that the optimization is able to force the flow field towards its true values throughout the sub-domain. The effect of adding noise to the velocity observations slightly increases all of the error measures as can be seen by comparing case F2 to case C2. Using an objectively mapped streamfunction field to construct the first guess does not adversely affect the error measures. Comparing case G2 to case F2 in table 4.1, one can see that the total error measures are reduced by approximately the same proportion from their first guess values.

4.2 Sensitivity

The gradient of the model counterpart of a datum with respect to the estimated boundary and initial conditions, can be calculated via the sensitivity matrix. This procedure was presented in section 2.5 for the estimated initial conditions. Sensitivities for individual data points are now calculated using the estimated boundary and initial conditions from twin experiment C2.

As in section 2.5 the sensitivities are illustrated for two representative data points. The first is the eastward velocity at current meter 3 (at the center of the array) at day 5 (time–step 120), the second is also the eastward velocity at the same location but fourteen days later at day 19 (time–step 456). These two examples are chosen to show how the influence of the model/data misfit on the control variables changes, from early times to later times in the assimilation period.

In figures 4.2, 4.3 and 4.4 are shown the sensitivities of the first data point to the vorticity initial conditions, the vorticity boundary conditions and the streamfunction boundary conditions respectively. Figures 4.5, 4.6 and 4.7 are the same, but for the second data point. The contour interval is the same in all of the figures in this section. In these figures the sensitivity with respect to the scaled control variables is

Figure 4.2: Sensitivity to the vorticity initial conditions, of the eastward velocity recorded at current meter 3 (center) at day 5.

displayed, ie. boundary streamfunction, boundary vorticity and initial vorticity are all of order one.

Comparing figures 4.2 and 4.3, it is apparent that the datum at day 5 is more sensitive to the vorticity initial conditions than to the vorticity boundary conditions, which is to be expected early on in the assimilation period. The velocity at current meter 3 at five days is of the order of 10 cm/s, both in the true flow field and in the estimated flow field (see the velocity time series in figure 3.7) which suggests that information from the model/data misfit is advected approximately two grid points in five days in the adjoint model. One can see from figure 4.2 that the velocity observation at the central current meter is most sensitive to the vorticity initial conditions about two grid points away to the south–southwest. This is in agreement with the estimated flow field at $t = 0$ shown in figure 3.8.

Also, one can see (from figure 3.8) that the inflowing velocities at the southern end of the western boundary at early times are quite high. The maximum flow speed in the jet is of the order of 1 m/s. In five days, information can be advected approximatedly twenty grid points by the flow emanating from the western boundary,

NORTH

EAST

WEST

SOUTH
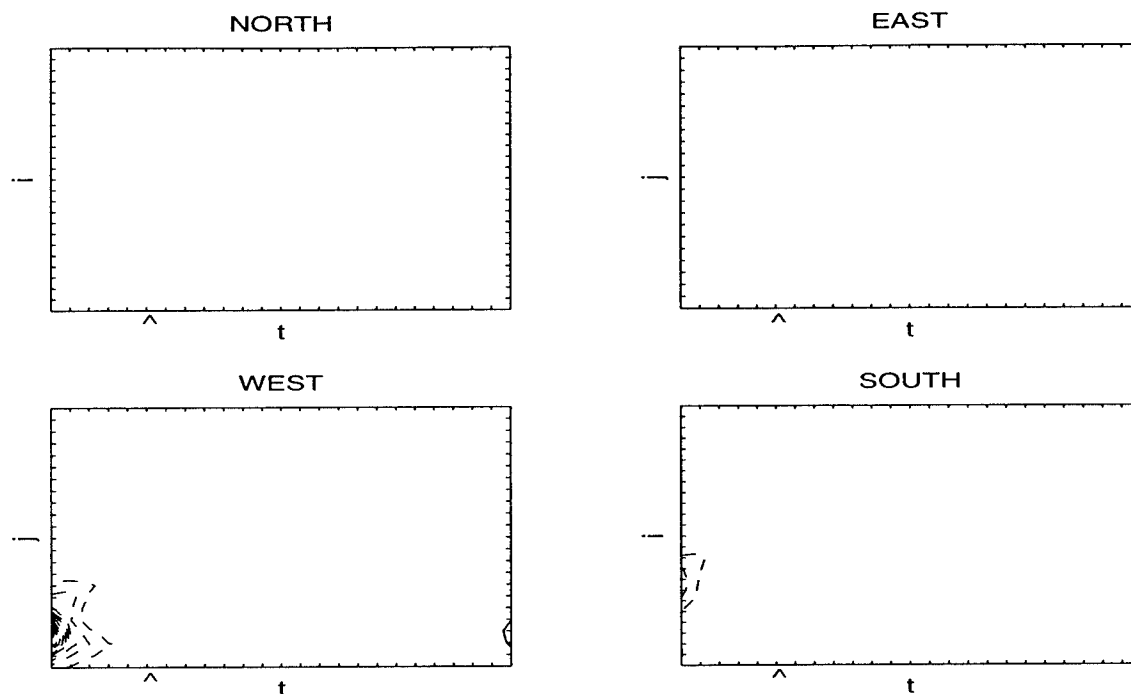
Figure 4.3: Sensitivity to the vorticity boundary conditions, of the eastward velocity recorded at current meter 3 (center) at day 5. The abscissa of each plot is time marked in days, the ordinate of each plot is distance along the boundary marked at every grid point.

NORTH

EAST

WEST

SOUTH
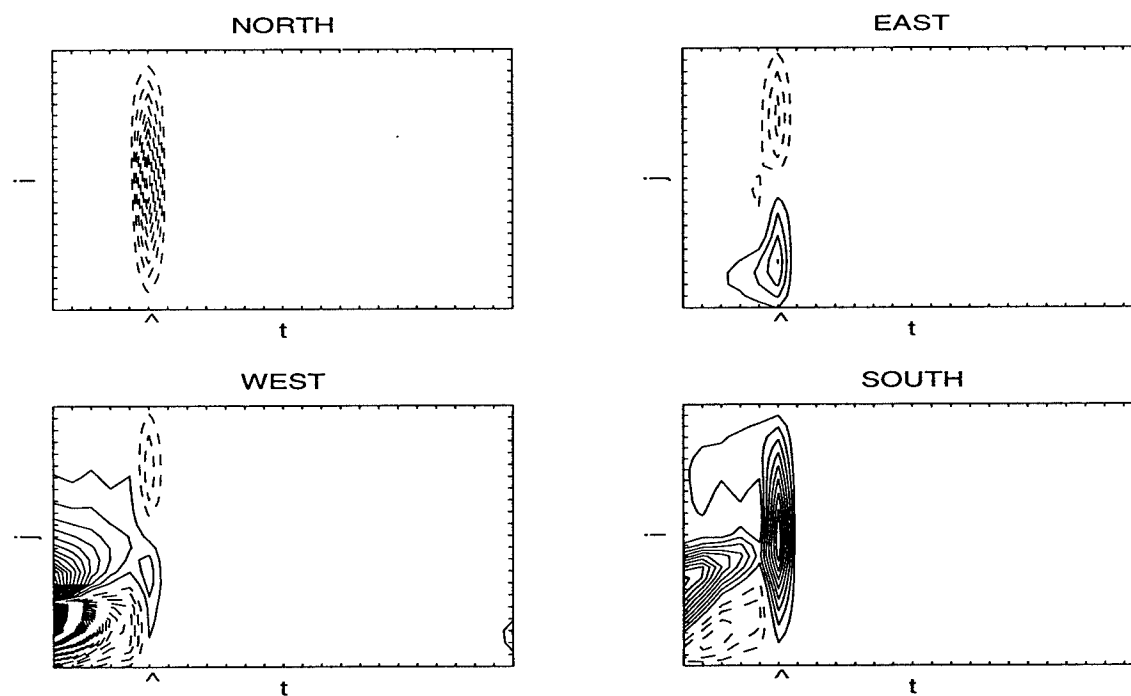
Figure 4.4: Same as figure 4.3 but for the streamfunction boundary conditions.

109
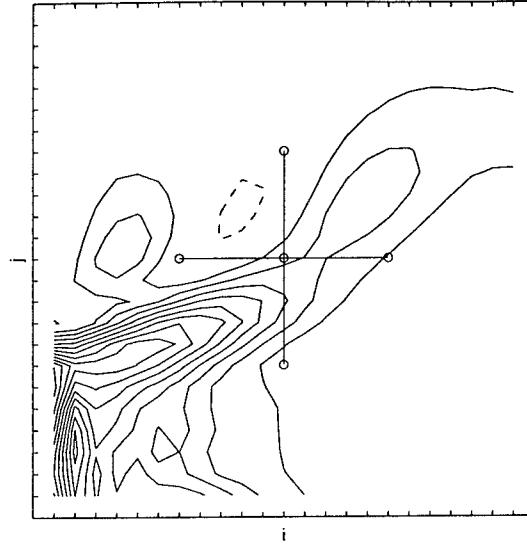
Figure 4.5: Sensitivity to the vorticity initial conditions, of the eastward velocity recorded at current meter 3 (center) at day 19.

which is greater than the distance from the observing location to the boundary inflow. Hence the datum at day 5 displays some sensitivity to streamfunction and vorticity at earlier times on the western boundary.

From the sensitivity plots for the second data point at 19 days, we can see that this datum is more sensitive to the boundary streamfunction and boundary vorticity than to the initial vorticity. At this later time, the flow observed by the central current meter is almost all entering the model domain at times later than $t = 0$.

In the plots of the sensitivity of the data to the estimated streamfunction boundary conditions (figures 4.4 and 4.7), there are peaks in sensitivity along all boundaries at the observation times (the observation times are indicated by check marks on the horizontal axes). The instantaneous sensitivity of the velocity at an interior point to all boundary values of streamfunction, is explained in the appendix in terms of the adjoint model equations and the Lagrange multipliers. This phenomenon can also be understood in terms of the forward model. If the streamfunction is perturbed anywhere on the boundary at some time, the perturbation is felt throughout the interior streamfunction field at the same time, since the total streamfunction field
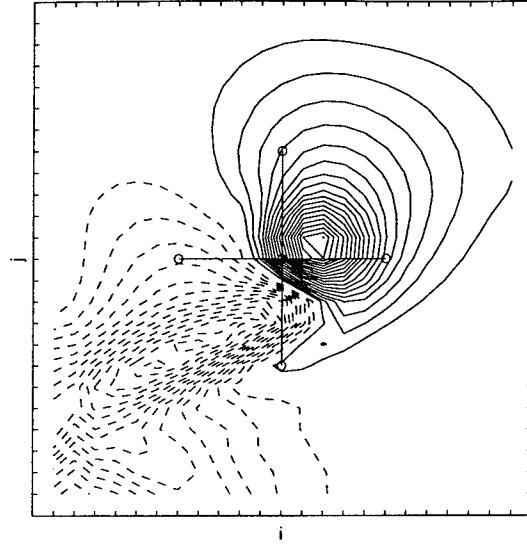
110
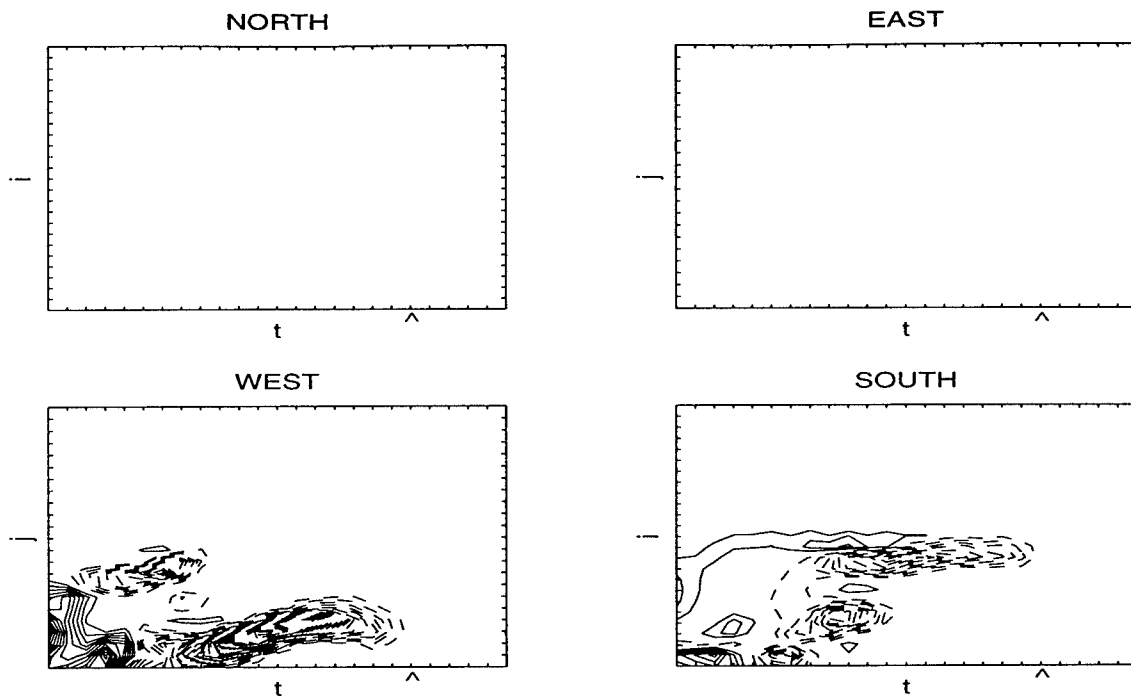
Figure 4.6: Sensitivity to the vorticity boundary conditions, of the eastward velocity recorded at current meter 3 (center) at day 19. The abscissa of each plot is time marked in days, the ordinate of each plot is distance along the boundary marked at every grid point.

must still satisfy the Poisson equation at that time. This point is further discussed in the next section.

Both data points presented here appear to be more sensitive to the boundary streamfunction at earlier times, than to the boundary vorticity at earlier times. By varying the boundary streamfunction at times earlier to the observation time, the entire streamfunction field can be varied at earlier times. Thus the streamfunction that is observed at a current meter can readily be changed by varying the boundary streamfunction at the observation time and at earlier times. Apart from the instantaneous responses to the boundary streamfunction, both data points are relatively insensitive to conditions on the northern and eastern boundaries.

These sensitivity plots for case C2 show that the observations produced by the estimated ocean are most sensitive to streamfunction and vorticity on the southwest part of the boundary at early times. The model counterparts of the data are forced
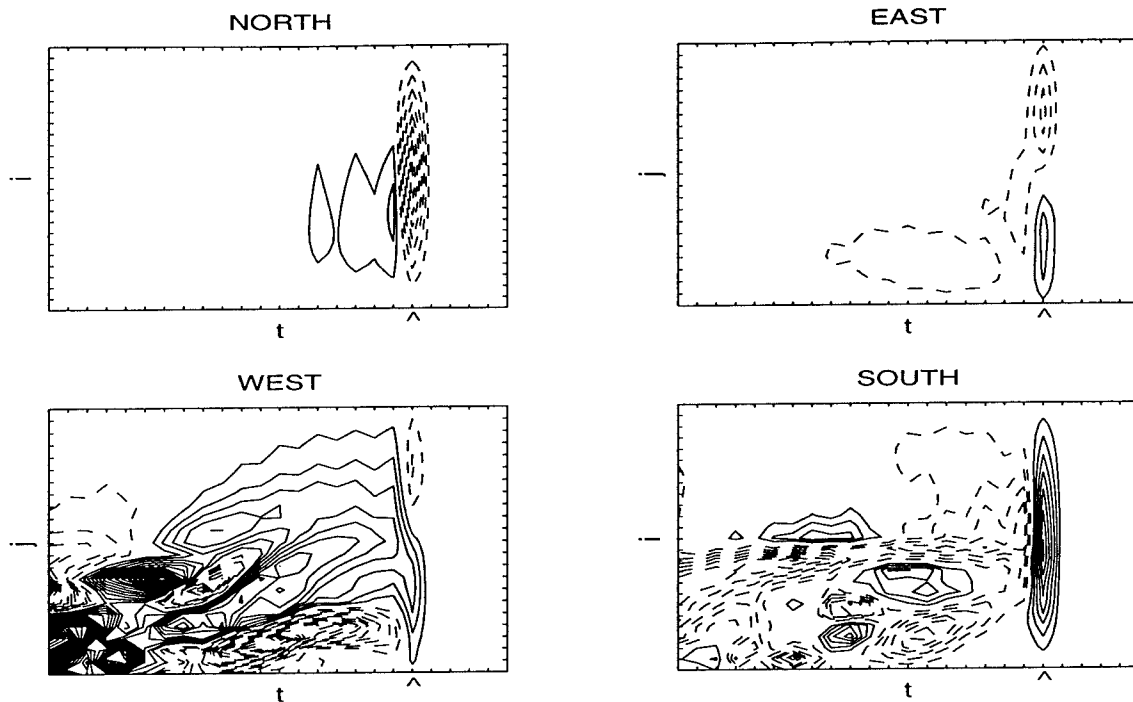
Figure 4.7: Same as figure 4.6 but for the streamfunction boundary conditions.

towards the true data, during the optimization, by varying the streamfunction and vorticity on the southwest part of the boundary, where the jet enters the model domain.

4.3 The spread of information

The communication of information, from the boundary conditions to the model counterparts of the data in the forward model, and conversely from the model/data misfit to the boundary gradients in the adjoint model, appears to occur by two distinct processes contained in the dynamical model.

Information can be advected. The conservation of vorticity along streamlines (albeit with some dissipation) allows boundary vorticity at inflow points to influence the interior flow field. Examination of the sensitivity plots in figures 4.3 and 4.6, together with the snapshots of estimated streamfunction and vorticity, figures 3.8

and 3.9 for case C2, shows that advection of vorticity along streamlines is how the south–west boundary vorticity at earlier times is influencing the model counterparts of the current meter data at later times. The values of streamfunction on the south–west boundary also strongly influence the current meter data, as can be seen from figures 4.4 and 4.7. The boundary streamfunction sets the location and speed of the inflow and outflow as the streamfunction field gives the advective velocities. The model counterparts of the data are thus more sensitive to the boundary values of streamfunction than to the boundary values of vorticity, at the south–west inflow points.

Information can be spread instantaneously. This process, which has been touched upon several times so far in this study, is a consequence of the ellipticity of the Poisson equation that relates streamfunction to vorticity.

On page 143 in the appendix it is explained how observations of streamfunction[1] cause instantaneous jumps in the cost function gradient for the boundary streamfunction at the observation times. The estimated boundary streamfunction itself then exhibits these jumps at the observation times. The gradient for boundary vorticity does not respond instantaneously to the intermittent observations, so the estimated boundary vorticity is smooth in time. Moreover, because streamfunction and vorticity at the boundary grid–points are not forced to obey the model equations, the spikes in the boundary streamfunction are not smoothed in time by the dynamics. This phenomenon is clearly seen in the sensitivity plots shown in the previous section.

In section 3.3, a comparison was made between case C2 and case D2. The only difference between these two experiments is that C2 had data available at every 48th time–step whereas D2 had data available at every time–step. It was seen that the periodicity of the data sampling appears in the temporal behavior of the estimated boundary streamfunction, but not in the estimated boundary vorticity (compare fig-

---

[1]The velocity observations are explicit functions of the streamfunction at neighboring points, see equation (1.5)

113

ure 3.11 for case C2 with figure 3.14 for case D2). Note that because the boundary streamfunction is expanded in a Fourier series with a minimum period of two days, the spikes at the observation times for case C2 become a wave with a two day period. Hence for cases B2 and C2 (which both used flat scaling and two–day data sampling) there is a strong two–day periodicity in the estimated boundary streamfunction. This is apparent in the residual error measures for streamfunction plotted in figure 4.1.

For the estimated streamfunction fields from case C2, the two–day periodicity is strongest at the boundaries and diminishes as one moves away from there as the model equations act as a smoother in the interior. In figure 4.8 time series of true and estimated streamfunction are shown at four grid–points from the western boundary to the centre of the domain. The two–day variability is strongest at the boundary and diminishes for grid–points farther from the boundary.

It appears therefore that the model dynamics is performing well as a dynamical interpolater between observation times for the interior streamfunction field, but not so for the boundary streamfunction as the equations are not directly evaluated at boundary points. The dynamics produces motions with periods much longer than two days, so the interior streamfunction is smoothed between observation times. The boundary streamfunction is in a sense decoupled from the interior dynamics, so the spikes in the temporal behavior are not smoothed.

4.4   Estimated errors in the boundary conditions

Using the sensitivity matrix method of section 2.3.2, the Hessian of the cost function with respect to the control variables is calculated and inverted to produce the estimated error variance of the control variables at the minimum, and hence the estimated error in the initial conditions and the boundary conditions.

For the experiments of chapter three the control vector has $5,521$ elements, hence the Hessian matrix has $5,521 \times 5,521 = 30,481,441$ elements. For a matrix
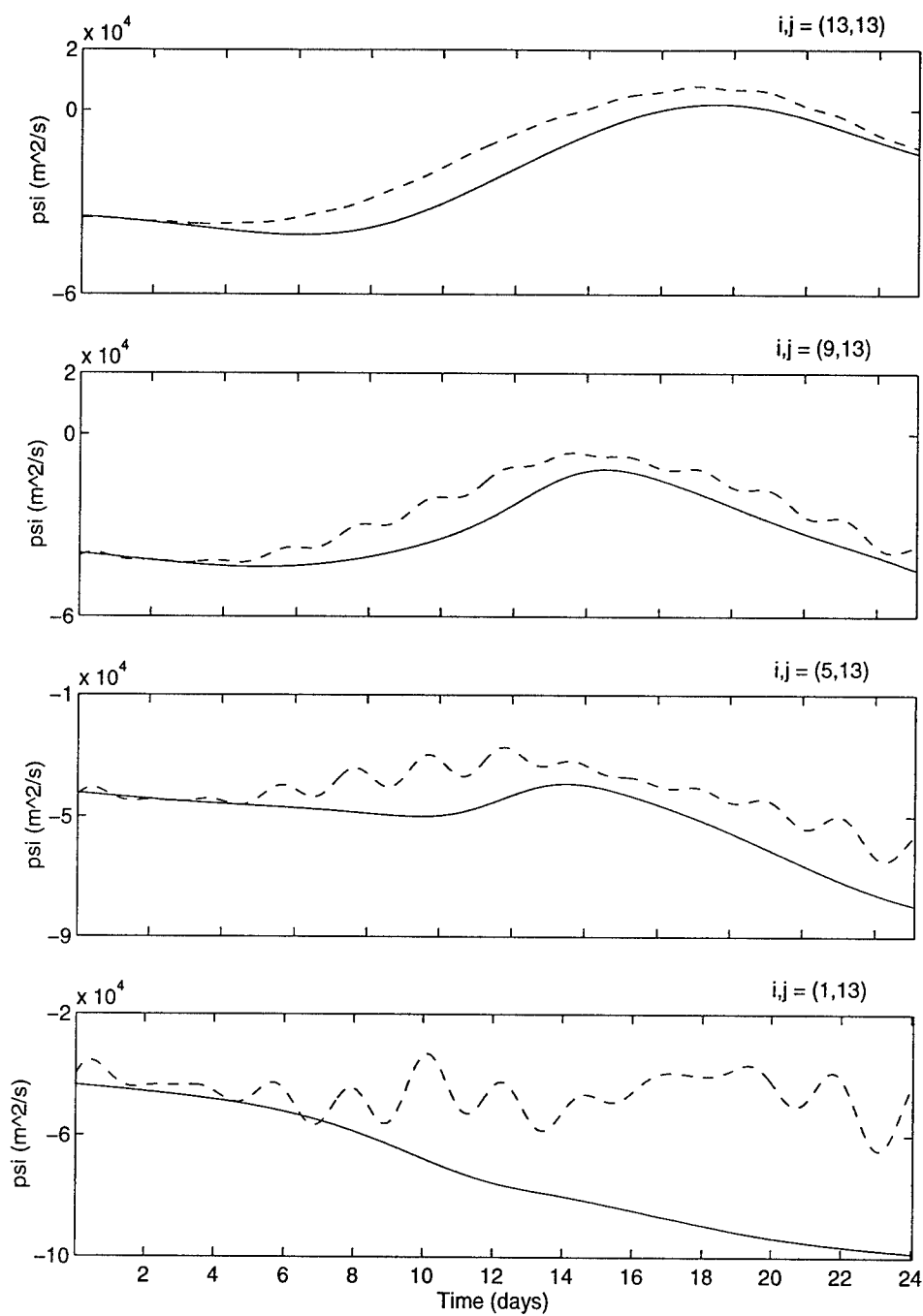
Figure 4.8: Time series of streamfunction taken at four grid–points from the western boundary (bottom panel) to the centre of the domain (top panel), (Solid) True (Dashed) Estimated for case C2.

of this size it is unfeasible to perform the same tests comparing the finite–difference Hessian to the Hessian calculated using the sensitivity matrix, as was done in chapter two.

Advantage is taken of the fact that the Hessian produced by the sensitivity matrix method is by definition symmetric and positive–definite. Only the upper triangular part of the Hessian then needs to be calculated, then the matrix is Cholesky factorized and inverted. These operations were performed on the Cray YMP at NCAR.

The expression for the estimated relative error in the control variables was presented in section 2.4. It is defined as

$$\text{relative error} = \sqrt{\frac{diag\left(\mathbf{H}^{-1}\right)}{|\mathbf{P_0}|}}$$

where $\mathbf{H}^{-1}$ is the inverse of the Hessian matrix, and $\mathbf{P_0}$ is the *a priori* covariance matrix for the control variables.

Recall that the control variables are the vorticity initial conditions plus the expansion coefficients from equation 3.1 for boundary streamfunction and vorticity. The expansion coefficients are converted back to time–series by a linear transformation. The same linear transformation is used to convert the estimated error covariances for the expansion coefficients, into error covariance time–series for boundary streamfunction and vorticity.

Estimated boundary and initial conditions whose values have been changed by the optimization from their first guess, have relative errors less than one. The lower the relative error the more influence an initial or boundary value has on the model/data misfit, and due to the presence of data it is known with more certainty than before.

The estimated relative errors shown here are for the estimated control variables from case C2. In figure 4.9 is shown the estimated relative error in the vorticity initial conditions, figure 4.10 shows the estimated relative error in the vorticity boundary
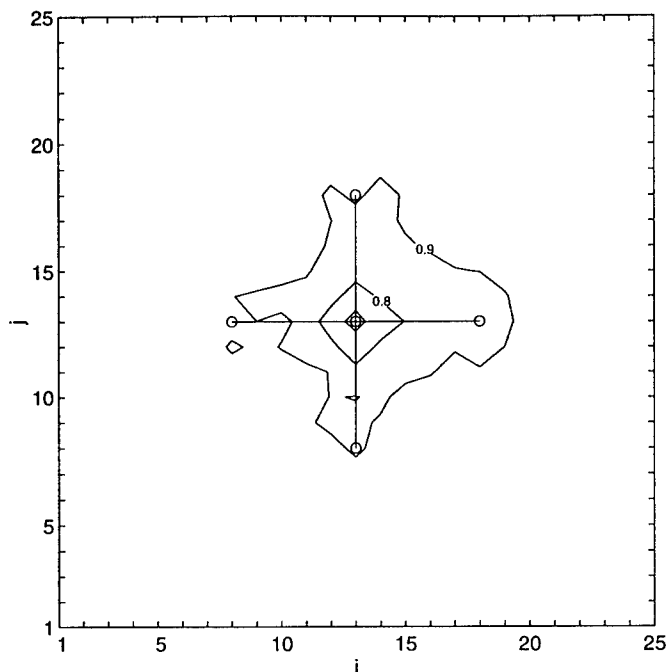
Figure 4.9:   Estimated relative error in the vorticity initial conditions for case C from chapter three. This figure may be compared to figures 2.3 and 2.1.

conditions, and figure 4.11 shows the estimated relative error in the streamfunction boundary conditions.

The first guess for the vorticity initial conditions in this case (C2) is the true initial conditions. Consequently the optimization does not change the vorticity initial conditions very much from their first guess. The model/data misfit at later times is not as sensitive to changes in these initial conditions, as it is to changes in the boundary conditions at later times. Hence the estimated error is not changed much from its *a priori* value. Only in the immediate vicinity of the observing array does the assimilation improve the relative error in the vorticity initial conditions.

The vorticity boundary conditions are changed from their first guess only in the southwest corner, as was seen in the last two sections. Hence the relative error is low only in the southwest corner at early times. The meander event in the observations at later times is produced in the assimilation by changing the boundary vorticity in the
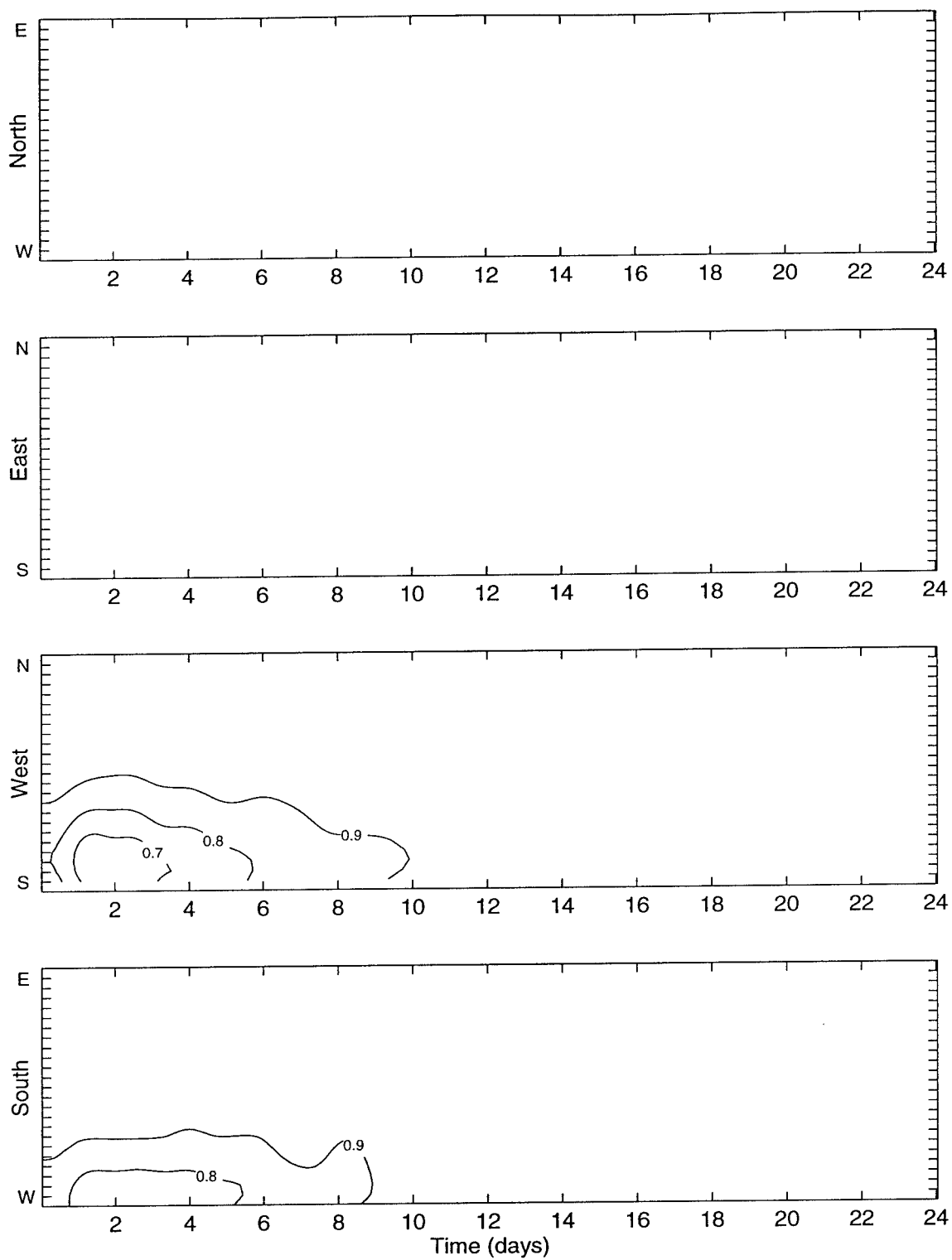
Figure 4.10: Estimated relative error in the vorticity boundary conditions for case C2 from chapter three.
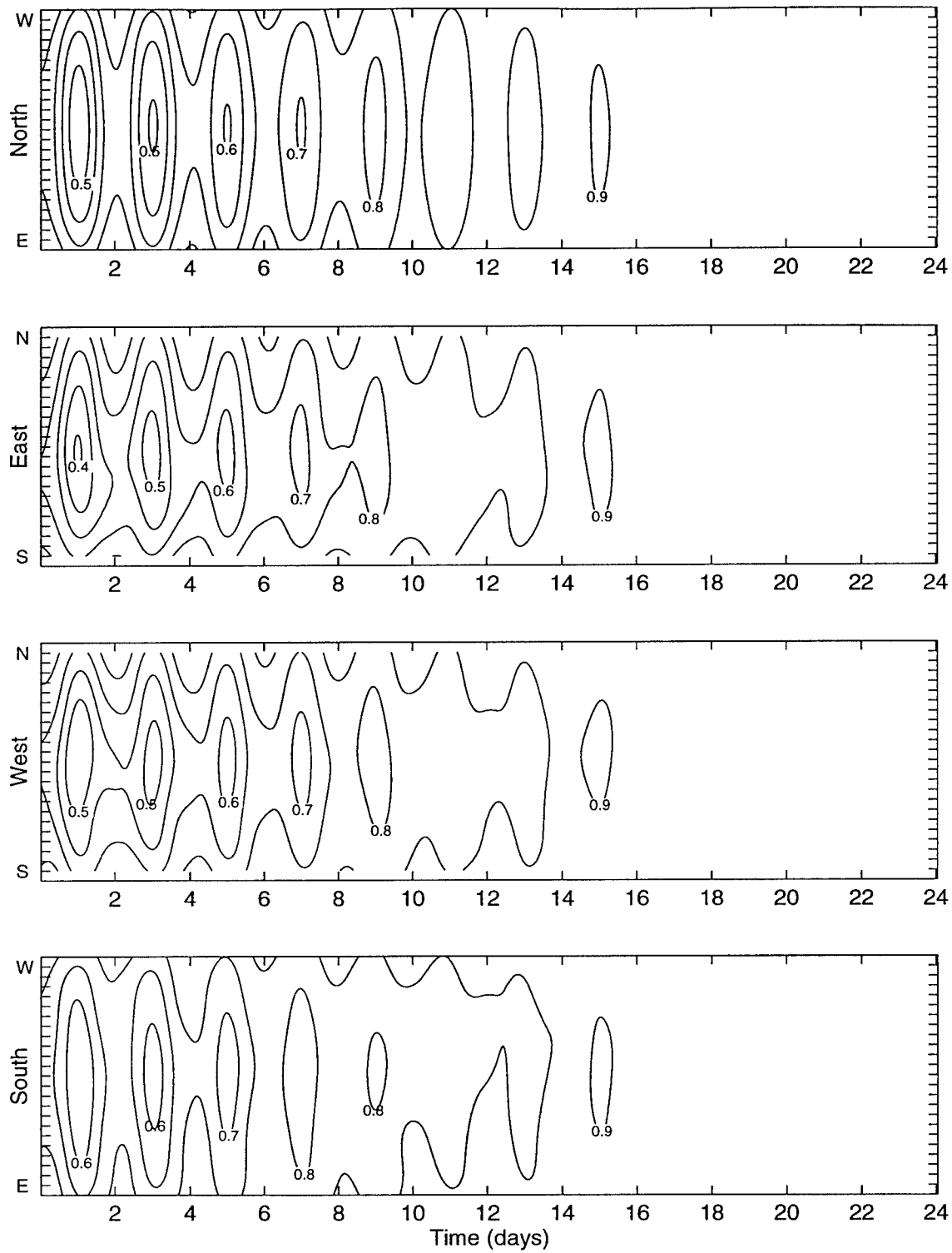
Figure 4.11: Estimated relative error in the streamfunction boundary conditions for case C2 from chapter three.

southwest corner at early times away from its first guess. Elsewhere on the boundary, vorticity does not influence the model/data misfit.

From the sensitivity calculations we saw that boundary streamfunction instantaneously affects the model/data misfit at observation times. This effect dominates the relative error maps for boundary streamfunction. The relative error becomes lower at earlier times because a change in boundary streamfunction at some time causes the entire interior streamfunction field to change at that time, thus affecting the entire streamfunction field at any later time. Also the highly advective nature of the flow means that it takes time to go from the boundary to the data points. Hence the earlier boundary streamfunction influences more observations than the later boundary streamfunction, so the estimated error is lower at earlier times.

An interesting comparison would be to calculate the Hessian for case D2, to see whether continuous data sampling improves the estimated error. For practical reasons this is beyond the scope of this study as the sensitivity matrix for case D2 is larger (greater number of elements) than the Hessian, due to the much greater number of data points. The sensitivity matrix method would thus be an inefficient way of calculating the Hessian for case D2, and one might be better off using finite-differences or the second order adjoint method of Wang *et al.* (1992). To further complicate matters, the data points would not be independent of each other if the continuous data sampling was obtained by interpolation, and one would have to include off–diagonal covariances in **R**.

4.5   Estimated errors in the interior

In section 2.1 it was shown that errors in the control variables can be transformed into errors in the model counterparts of the observations by the sensitivity matrix, in its role as a Jacobian matrix, i.e.

$$\mathbf{m}(\hat{\theta}) - \mathbf{m}(\theta) = \frac{\partial \mathbf{m}}{\partial \theta}[\hat{\theta} - \theta],$$

where $\hat{\theta}$ is the optimally estimated control vector and θ is the true control vector. A similar transformation may be constructed to transform errors in the control variables into errors in the interior fields of streamfunction and vorticity,

$$\psi_{ij}^t(\hat{\theta}) - \psi_{ij}^t(\theta) = \frac{\partial \psi_{ij}^t}{\partial \theta}[\hat{\theta} - \theta].$$

Then the expected error variance of the interior streamfunction is given by

$$
\begin{aligned}
< (\psi_{ij}^t(\hat{\theta}) - \psi_{ij}^t(\theta))^2 > &= \frac{\partial \psi_{ij}^t}{\partial \theta} < (\hat{\theta} - \theta)(\hat{\theta} - \theta)^T > \left(\frac{\partial \psi_{ij}^t}{\partial \theta}\right)^T \\
&= \frac{\partial \psi_{ij}^t}{\partial \theta} \widehat{\mathbf{P}} \left(\frac{\partial \psi_{ij}^t}{\partial \theta}\right)^T
\end{aligned}
$$

where $\widehat{\mathbf{P}}$ is the estimated error covariance of the control variables, computed from the inverse Hessian using the sensitivity matrix method. The main diagonal elements of $\widehat{\mathbf{P}}$ were presented in the previous section.

The vector $\frac{\partial \psi_{ij}^t}{\partial \theta}$ can be computed using the same method as was used to construct the sensitivity matrix described in section 2.3.2. That is, the cost function used in the optimization, J, is replaced by an interior streamfunction (or vorticity) value, ψ_{ij}^t. The forward and adjoint models are then run, starting from the optimally estimated control variables, to produce the gradient of ψ_{ij}^t with respect to θ at the minimum of the cost function.

To calculate the expected error in streamfunction or vorticity at one interior grid–point at one time requires one iteration of the forward and adjoint models. Thus an error map over all of the interior grid–points at one time requires 529 iterations, which can be done in a reasonable amount of time. Twice this number of iterations are performed because the above expression for the expected error variance of ψ_{ij}^t, needs to be compared to the *a priori* error variance of ψ_{ij}^t given by

$$\frac{\partial \psi_{ij}^t}{\partial \theta} \mathbf{P_0} \left(\frac{\partial \psi_{ij}^t}{\partial \theta}\right)^T$$

where $\mathbf{P_0}$ is the *a priori* error covariance matrix for the control variables (see section 1.2). The above expression is thus the variance in ψ_{ij}^t due to the *a priori* variance in the initial and boundary conditions.

The relative error defined by

$$\left[\frac{\frac{\partial \psi_{ij}^t}{\partial \theta} \widehat{P} \left(\frac{\partial \psi_{ij}^t}{\partial \theta} \right)^T}{\frac{\partial \psi_{ij}^t}{\partial \theta} P_0 \left(\frac{\partial \psi_{ij}^t}{\partial \theta} \right)^T} \right]^{\frac{1}{2}}$$

is shown as a contour plot in figure 4.12, for the interior streamfunction (top) and interior vorticity (bottom), from case C2 at day 16.

As one would expect the relative error for the interior streamfunction is lowest in the vicinity of the observing array, and is generally lower in the southern part of the sub–domain where the interior field is more sensitive to the inflow and outflow at the boundaries. The relative error map for interior vorticity is more interesting. Comparing this map to the estimated vorticity map at day 16 for case C2 shown in figure 3.9, one can see that there is a region of large relative error in the northern part of the sub–domain that corresponds closely with the region of low vorticity seen in the estimated vorticity map. The tongues of positive and negative vorticity that cross the observing array in a northwest–southeast direction have low relative error.

At day 16 the meander event is passing through the observing array (see the estimated streamfunction plots in figure 3.8). This event is the strongest signal in the available data, and the optimization adjusts the boundary conditions so as to re–construct this event in the estimated flow field. There is therefore a strong sensitivity between the interior streamfunction and vorticity in the meander at day 16 and the boundary conditions at previous times.

In sections 4.2 and 4.4 of this chapter it was illustrated that the boundary values of streamfunction and vorticity most sensitive to the available data are those in the southwest corner of the sub–domain at early times. Through the model dynamics these boundary values are forced by the available data to vary in order that the interior streamfunction and vorticity at day 16, in the vicinity of the observing array, is in agreement with the observed velocities. By this process information about the

122
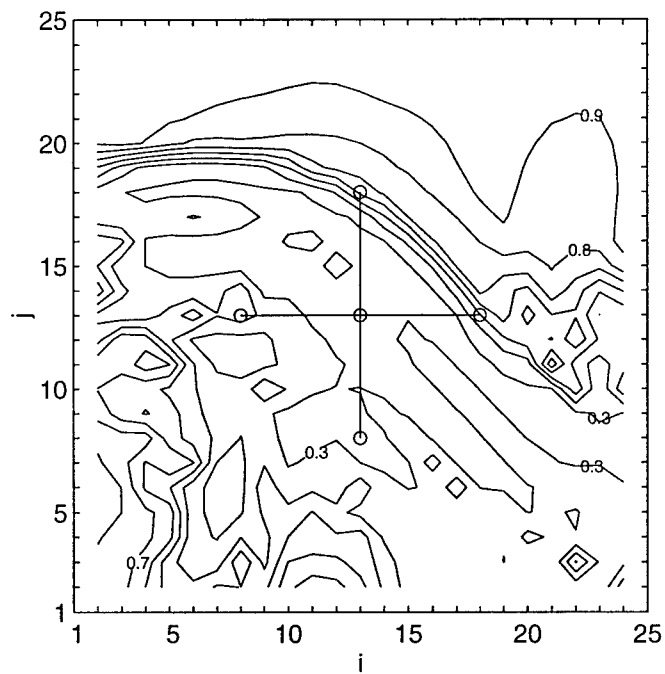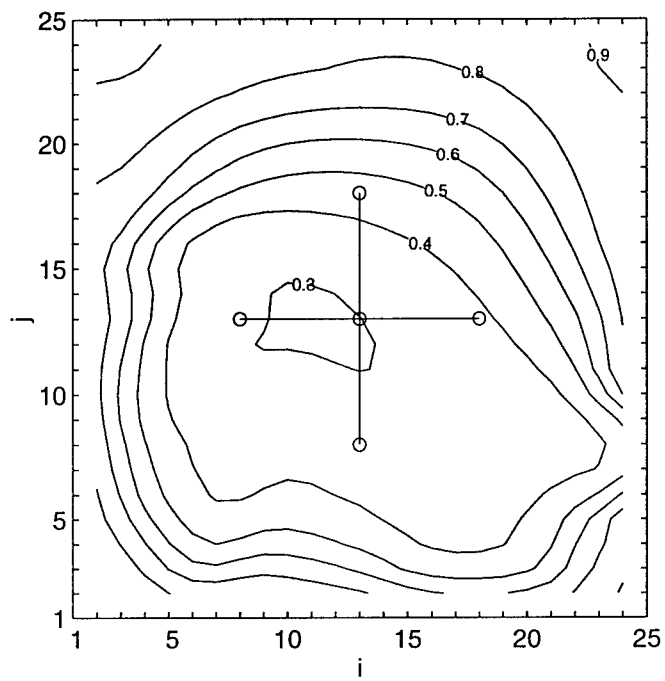
Figure 4.12: Estimated relative error in the interior (top) streamfunction and (bottom) vorticity fields at day 16, for case C2.

point measurements of velocity is spread through parts of the sub–domain, reducing the relative error.

Chapter 5

Conclusions

Experiments were carried out in this dissertation to explore the estimation of open ocean boundary and initial conditions from simulated sparse data in the presence of strong nonlinearity. The results of these experiments represent a significant step towards the assimilation of SYNOP East data into an open ocean model.

There are two aspects to judging the success of an assimilation. The first aspect concerns the comparison of *a posteriori* statistics with *a priori* statistics, which one can do with real data. The second aspect concerns comparisons of the estimated flow field with the true flow field, which can only be made in the context of twin experiments.

For the first type of judgement, the primarily accepted measure of success is the final value of the cost function. Successful minimization of the cost function is a necessary condition for the model to be judged consistent with the data. In this study when the cost function is minimized to order one, the model/data residuals are of the same order as the *a priori* error in the data. The sensitivity matrix, which can be calculated when the assimilation uses real data, illustrates by which pathways the data improves the estimation of the control variables. A qualitative view of the dependence of an observation upon the control variables can be readily seen from the columns of the sensitivity matrix. Quantitative error estimates for the control

variables can also be calculated from the sensitivity matrix by the method described in chapter two. Most importantly, the error estimates can be calculated when the assimilation uses real data.

The second way of judging the success of an assimilation is by comparison with the true fields. Here this has been done qualitatively by displaying the true streamfunction fields alongside the estimated streamfunction fields. In the cases presented in chapter one and chapter three, this means of comparison enables one to see that the estimated flow field looks quite similar to the true flow field in the vicinity of the observing array, but differs as one moves towards the boundaries where the estimated flow field is more influenced by the boundary conditions. Quantitative measures of the residuals between the estimated and true fields were shown in section 4.1.

Chapter one presented the model and the data used in all twin experiments performed in this study. These first experiments were an attempt to avoid the estimation of the open boundary conditions, by treating them as known and diminishing their influence on the assimilation by the inclusion of a sponge layer around the boundary. None of these experiments were successful in diminishing the effect of the prescribed boundary conditions. However, case A1, which employed thirteen current meters, was able to adequately minimize the cost function. Case B1 and Case C1, which both employed five current meters and two tomographic reciprocal travel times, were not able to minimize the cost function adequately. There was more information available in the data in case A1, as the observing array covered the jet at all times. The available data in cases B1 and C1 contained relatively less information about the jet, as the jet appeared in the observations only at later times as it meandered through the array.

For all of cases A1, B1 and C1, the estimated flow fields were quite different from the true flow fields in regions away from the array. It was seen that the model set–up for these twin experiments was inconsistent with the strong flow velocities observed at the array. The prescribed boundary conditions in the model cause the

optimization to estimate vorticity initial conditions that contain the strong flow within the model boundaries. In the true flow field, over the period of the assimilation, this strong flow originates from farther away, beyond the artificial boundaries of the model.

Chapter two presented the estimation of errors for the estimated control variables. It was shown by Gauss–Markov theory, that the estimated error covariance of the control variables is given by the inverse Hessian of the cost function at the minimum, as long as a nonlinear term could be neglected. The Hessian was calculated by two methods: finite–differences and the sensitivity matrix. The calculations were performed for an experiment which had strongly nonlinear dynamics, and for an experiment which had weakly nonlinear dynamics. The control variables for both experiments were the vorticity initial conditions.

The explicit expression for the Hessian of the cost function, equation (2.6) on page 44, contains a nonlinear term, $\frac{\partial^2 \mathbf{m}}{\partial \theta^2} \mathbf{R}^{-1}(\mathbf{m}(\theta) - \mathbf{d})$, arising from the nonlinearity of the model counterparts of the data, $\mathbf{m}$, with respect to the control variables, $\mathbf{x}$. From the theory, it was determined that this term needs to be ignored in order for the estimated error covariance of the control variables to be given by the inverse Hessian. The sensitivity matrix method of computing the error covariance matrix ignores this term from the outset and the Hessian is well–conditioned, both for strongly nonlinear dynamics and weakly nonlinear dynamics. The finite–difference method implicitly includes the nonlinear term in its calculation of the Hessian. Thus the inverse of the finite–difference Hessian gives the error covariance matrix only when the nonlinear term is negligible. For weakly nonlinear dynamics this was found to be the case. The Hessian matrices produced by both methods were essentially the same, and both could be inverted to produce the relative error in the vorticity initial conditions shown in figure 2.3.

In the presence of strong nonlinearity, the nonlinear term may be significant enough to deteriorate the strong positive–definiteness contributed by the other terms in equation 2.6, rendering the Hessian ill–conditioned. In fact the finite–difference

Hessian was found to be ill–conditioned, while the sensitivity matrix method produced a well–conditioned Hessian which was inverted to give the relative error in the vorticity initial conditions shown in figure 2.1. Despite the ill–conditioning of the finite–difference Hessian, it was found to be very similar, in structure and size, to the Hessian computed by the sensitivity matrix method. Thus, although the nonlinear term makes a small contribution to the finite–difference Hessian, it is big enough to render the Hessian ill–conditioned.

In terms of the behavior of the cost function in the vicinity of its estimated minimum, the sensitivity matrix method gives only the local curvature of the cost function in control space, under the assumption that this curvature is quadratic. If the residuals in the model/data misfit are large compared to the *a priori* errors, as was the case for the twin experiment used in chapter two, the nonlinear term will be significant when $m(x)$ is nonlinear. Thus, if the model/data residuals are small in the nonlinear case, the finite–difference Hessian could be well–conditioned even in the presence of strong nonlinearity.

Examination of the off–diagonal structure of the estimated error covariance matrix showed that the dynamics acted to reduce the length–scale of spatial covariance in the vorticity initial conditions. The *a priori* length–scale set by the Laplacian smoothing term is larger than the length–scale for vorticity that is inherent in the model dynamics.

The sensitivity matrix was also found to be useful in illustrating the dependence that the model counterparts of the data have to the vorticity initial conditions. For the weakly nonlinear case a velocity observation was seen to be most sensitive to those vorticity initial conditions in the immediate vicinity of the observing location, even late in the assimilation period. For the strongly nonlinear case, a velocity observation taken late in the assimilation was seen to be strongly sensitive to the vorticity initial conditions throughout the domain because the flow field is forced to be contained by the boundaries.

128

The results of the experiments in chapter one and chapter two lead to the conclusion that in order for the estimated flow field to resemble the true flow field, the time–dependent values of streamfunction and vorticity on the artificial boundaries of the model domain need to be estimated as part of the assimilation.

Explicit expressions for the gradient of the cost function with respect to boundary streamfunction and vorticity were formulated (shown in the appendix). The time–series of boundary streamfunction and vorticity were expanded in Fourier series so as to reduce the number of control variables. Several twin experiments were performed that illustrated the dependence of the estimated flow field upon the first guess used for the control variables, and upon the presence of noise in the observations and the first guess.

The experimental set–up for these experiments was more sophisticated than those in the first chapters. In chapter three the control variables were the sufficient set of initial and boundary conditions needed to integrate the barotropic vorticity equation forward in time in a domain with open boundaries (Charney *et al.*, 1950). The only *a priori* information needed was a first guess and scaling for the control variables, that is, a point in control–space at which to start the optimization with relative weights for each control variable. The first guess and scaling have physical meaning and can be estimated beforehand for real data: the first guess is the expected values of the initial and boundary conditions, and the scaling is the expected variance in these values.

All the twin experiments presented in chapter three performed well in the sense that the cost function was minimized to order one for all experiments. The best minimization was for case C2 where the cost function was minimized to the lowest value relative to its value at the start of the minimization. For this case, persistence in time of the true initial conditions was used as a first guess for the control variables, and noise-free data was available every two days. The choice of a time–invariant state as a first guess is how one could proceed if using real data. Often there is a regional

hydrographic survey at the start of a mooring time–series. If not, one could use a climatology for the region for a first guess. Case G2 was the same as case C2 but with noisy observations, and the initial conditons were taken from simulated hydrographic survey of streamfunction objectively mapped onto the model grid. This experiment may be regarded as the most successful as it is the one that is most applicable to the real world.

In chapter four the quality of the assimilation experiments of chapter three was assessed. Root–mean–square residuals with the true field were presented, showing the differing ranges of spread of information for each experiment. The computation of the sensitivity matrix showed how information from an observation was spread backwards in time by the adjoint model, and showed the relative influence of boundary and initial conditions on a datum. The estimated error covariance for the estimated initial and boundary conditions for case C2 was calculated using the sensitivity matrix method. Error maps for the interior streamfunction and vorticity fields were also constructed. From the error maps for the boundary and interior vorticity, the process can be seen by which strong signals in the available data influence the boundary conditions and how the relative error is reduced in regions where the information spreads.

The sampling period of the velocity data was found to enter into the temporal behavior of the estimated boundary streamfunction. This behavior was found to be a property of the dynamics. The elliptic nature of the Poisson equation relating streamfunction to vorticity means that a variation in streamfunction anywhere in the model domain, at any particular time, is instantaneously felt throughout the domain. This phenomenon gives rise to jumps in the boundary streamfunction whenever velocity observations are available. Because the dynamical equations do not apply at the boundary points of the domain, the jumps in boundary streamfunction are not smoothed in time by the dynamics.

For all of the experiments from chapter three, the optimization was able to minimize the cost function by varying the temporal behavior of the boundary stream-

function and vorticity away from their first guess values. The vorticity is varied in the course of the optimization at boundary points, where it is advected into the domain and subsequently advected through the observing array. Boundary streamfunction, on the other hand, is varied by the optimization at all boundary points due to the elliptic effect that has been previously discussed. Varying boundary streamfunction at earlier times has a greater effect on the interior flow field.

The next step, before model/data assimilations can be run using real data, is to implement vertical variability in the quasi–geostrophic dynamical model. One could readily include the first and second baroclinic modes in the dynamical model used here, or construct a two or three layer model (see Flierl, 1978).

An interesting and potentially powerful observation from the SYNOP East dataset is areally–averaged vorticity. This can be obtained by integrating tomographic reciprocal travel times around the edges of the polygon defined by the locations of the acoustic transceivers (see Chester, 1993). Using the adjoint method with a quasi–geostrophic model, a vorticity observation would provide much more influence on the Lagrange multipliers than the streamfunction observations used here (see appendix, also Tziperman & Thacker, 1989). Moreover, the forcing in the adjoint model would be at every point within the areal average. Note that the areally–averaged vorticity data would not add more information to the assimilation beyond the along–path velocities given by the acoustic travel times. By relating a velocity observation to vorticity rather than streamfunction, the adjoint method may converge more readily.

The twin experiments presented here to estimate optimal boundary conditions used an assimilation period of only 24 days, during which time only one energetic event passed through the array. The estimated boundary conditions were varied by the optimization, around the inflow area prescribed by the first guess, so as to best reconstruct this single energetic event. It would be interesting if a longer assimilation period were used during which there were several energetic features observed.

The information from the observations would spread further in different directions, hopefully to give better boundary estimates.

In the original setting of this study with respect to the SYNOP dataset and the dynamics of the Gulf Stream, there were two issues that needed to be investigated before one could assimilate real data into a dynamical model. These issues were (i) the effect of strongly nonlinear dynamics on a model/data assimilation and the desirability of making error estimates in the presence of strong nonlinearity, (ii) the treatment of unknown boundary conditions for a regional open–ocean model.

The most important conclusion from the experiments performed here is that it is possible to estimate errors in the presence of strong nonlinearity, without linearizing the dynamical evolution of the flow field.

Modellers have had many problems with open boundaries, such as radiation conditions at outflow points (Orlanski, 1976; Chapman, 1985; Blumberg & Kantha, 1985). These problems are circumvented in the formalism of the adjoint method. At every iteration of the minimization of the cost function, the forward model dynamics are exactly obeyed because they are applied as a strong constraint in the adjoint method. The control variables are varied in the course of the minimization so as to always keep the strong constraint satisfied. Hence boundary values of stream-function and vorticity along outflow regions of the boundary are consistent with the neighboring interior values.

There is also the problem with characteristic points on the boundary where inflow changes to outflow and the streamlines run parallel to the boundary (Bennett,1992). The possibility of infinite vorticity gradients at characteristic points can be removed by adding a penalty term for gradients of vorticity on the boundary (Bennett, 1992). In the experiments of chapter three a term was added to the cost function to penalize the second derivatives of streamfunction and vorticity along the boundary. This part of the cost function may be preventing large vorticity gradients from forming near characteristic points. The formal ill–posedness at characteristic

points is a rather subtle matter. Further study is needed to isolate this effect from other much larger sources of error in experiments such as the ones presented here.

In a previous study (Seiler, 1993), boundary values of streamfunction and vorticity were optimally estimated using the adjoint method, while keeping the initial conditions at some specified values. Here the full set of initial and boundary conditions are estimated from the data.

For most of the twin experiments presented here, the first guess values for the boundary and initial conditions were chosen based upon almost total ignorance. The first guess values for the control variables were far from the true values in control-space. For all of the experiments except case E2, it was seen that the estimated boundary conditions were no closer to the true boundary conditions than were their first guess values. However, for case E2 we saw that when the first guess values were sufficiently close to the true values, the optimal estimates were closer to the true values than they were to their first guess values. Although the first guess for case E2 was obtained by randomly perturbing the true values causing the boundary smoothness cost rather than the model/data cost to force the estimates towards the true values, the results indicate that when the first guess is within some neighborhood of the true values the estimates will be forced towards the true values.

For the assimilation of the SYNOP dataset, the true boundary conditions are unknown. One could follow the strategy of case G2 and objectively map a large–scale time–dependent dataset for the region (such as OTIS for the Gulf Stream system), onto the grid–points of the model domain and onto the temporal variation at the boundaries, and use these mapped fields as a first guess for the initial and boundary conditions. The methods presented in this study could then be used to improve the estimated values of the initial and boundary conditions, the improvement arising from the assimilation of the interior observations with the dynamical constraints.

133

Appendix A

The adjoint method

A.1 General Form

The nonlinear minimization problem and a method of solution are presented here. As in the other chapters, vectors are denoted by lower–case boldface characters and matrices are denoted by upper–case boldface characters.

Given some state variables, ϕ, and control variables, θ, that are related by $\mathbf{f}(\phi, \theta) = 0$, the goal is to find the control variables that minimize some cost function or performance criteria, $J(\phi, \theta)$. That is, minimize

$$J(\phi, \theta)$$

with respect to θ while keeping the constraint

$$\mathbf{f}(\phi, \theta) = 0,$$

where the cost function and the constraint can be nonlinear functions. The fundamental difference between state variables and control variables here is that the values of control variables are unknown and need to be found, whereas the state variables are determined from the control variables via the constraint.

When the system of equations, $\mathbf{f}(\phi, \theta) = 0$, is treated as a strong constraint, then Lagrange multipliers may be introduced to solve this problem. An augmented

cost function is defined,

$$L(\phi, \theta, \lambda) = J(\phi, \theta) + \lambda^T \mathbf{f}(\phi, \theta)$$

where the Lagrange multipliers, λ, can be arbitrarily chosen. When the constraint is satisfied, $L = J$, and thus also the first variation, $dL = dJ$, where

$$
\begin{aligned}
dL &= L(\phi + d\phi, \theta, \lambda) - L(\phi, \theta, \lambda) + L(\phi, \theta + d\theta, \lambda) - L(\phi, \theta, \lambda) + \\
& \quad L(\phi, \theta, \lambda + d\lambda) - L(\phi, \theta, \lambda) \\
&= \frac{\partial L}{\partial \phi} d\phi + \frac{\partial L}{\partial \theta} d\theta + \frac{\partial L}{\partial \lambda} d\lambda.
\end{aligned}
$$

Usually J is a quadratic, as in this study, and has a minimum where $dJ = 0$. Thus minimizing J entails finding a point where the gradients vanish. Now it is obvious that $\frac{\partial L}{\partial \lambda} = 0$, from the constraint. The λ are now chosen such that $\frac{\partial L}{\partial \phi} d\phi = 0$, ie.

$$\left(\frac{\partial J}{\partial \phi} + \lambda^T \frac{\partial \mathbf{f}}{\partial \phi} \right) d\phi = 0.$$

This system is called the adjoint equations, from which the λ can be determined.

Thus,

$$dJ = dL = \frac{\partial L}{\partial \theta} d\theta$$

or

$$\frac{dJ}{d\theta} = \frac{\partial L}{\partial \theta}$$

which states that $\frac{\partial L}{\partial \theta}$ is the gradient of J with respect to θ, while holding $\mathbf{f}(\phi, \theta) = 0$ and while the λ are given by the adjoint equations.

An explicit expression for the gradient $\frac{\partial L}{\partial \theta}$ is determined from the augmented cost function. A gradient–search algorithm can then be used to find a minimum of the cost function with respect to the control variables. This can be quite an involved task when there are thousands of control variables, yet using a conjugate gradient routine the minimum is found in a few iterations when the constraint is linear. For nonlinear constraints there may be multiple local minima, and the minimum found

135

by gradient–search may depend upon where the search was started from, ie. the first choice for the control variables.

In this study the cost function is the least–squares misfit between the data and the model counterparts of the data. The constraint is the time evolution of the state variables given by a dynamical model. The full mathematical formulation is quite cumbersome involving much algebra. Only the more salient features of the formulation are presented here. Other derivations and formulations of adjoint methods for ocean models may be found in Tziperman & Thacker (1989), Thacker & Long (1988) and Talagrand & Courtier (1987).

Making the problem time–dependent, the constraint is the time evolution equation for the state variables, and the control variables are the initial conditions for the state variables, ϕ_0. The cost function is the least–squares model/data misfit, equation (1.3). The problem becomes: Minimize

$$J = \sum_k \frac{(m_k(\phi_0) - d_k)^2}{\sigma_k^2}$$

with respect to ϕ_0 while

$$\phi_{t+1} = \mathbf{f}(\phi_t),$$

for all $t = 0, \ldots, N$. As before we construct the augmented cost function

$$L(\phi_0, \ldots, \phi_N, \lambda_1, \ldots, \lambda_N) = J + \sum_{t=1}^N \lambda_t^T [\phi_t - \mathbf{f}(\phi_{t-1})].$$

Taking the first variation we get

$$dL = \frac{\partial L}{\partial \phi_0} d\phi_0 + \sum_{t=1}^N \left[\frac{\partial L}{\partial \phi_t} d\phi_t + \frac{\partial L}{\partial \lambda_t} d\lambda_t \right],$$

and $dJ = dL$ when the time–evolution equation for the state variables is being satisfied. As before $\frac{\partial L}{\partial \lambda_t} = 0$, and we get the adjoint model equations by setting $\frac{\partial L}{\partial \phi_t} d\phi_t = 0$, for all $t = 1, \ldots, N$, ie.

$$\left(\frac{\partial J}{\partial \phi_t} \right)^T + \lambda_t - \left(\frac{\partial \mathbf{f}}{\partial \phi_t} \right)^T \lambda_{t+1} = 0$$

where $\lambda_{N+1} \equiv 0$. This is an evolution equation for the Lagrange multipliers that runs backward in time forced by $\left(\frac{\partial J}{\partial \phi_t}\right)$. Note that this adjoint model is linear in λ_t, and uses the transpose of $\frac{\partial \mathbf{f}}{\partial \phi_t}$ as its transition matrix (which is why this whole procedure of solution is called the adjoint method).

When the adjoint model and the forward model equations are satisfied,

$$dJ = dL = \frac{\partial L}{\partial \phi_0} d\phi_0$$

thus the gradient of the cost function with respect to the control variables is

$$\frac{dJ}{d\phi_0} = \frac{\partial J}{\partial \phi_0} - \lambda_1^T \frac{\partial \mathbf{f}}{\partial \phi_0}$$

which can be calculated, then used to find the minimum of J with respect to ϕ_0.

Given the gradient of J with respect to ϕ_0, one can start from some guess of ϕ_0, calculate the gradient and move in the direction of the minimum of J. Then make a new guess for ϕ_0, get the new gradient and iteratively move through the vector space spanned by the control variables, looking for the minimum of J. There are many gradient search routines available that perform this procedure.

A.2 Discretized Ocean Model

The forward model equations, (1.1), are appended to the cost function with Lagrange multipliers, $\alpha_{i,j}^t$, $\mu_{i,j}^t$ and $\nu_{i,j}^t$ to make an augmented Lagrangian,

$$
\begin{aligned}
L = & \ J + \sum_{i=2}^{N-1} \sum_{j=2}^{M-1} \left(\sum_{t=0}^{T} \left[\mu_{i,j}^t \left(\nabla^2 \psi_{i,j}^t - \zeta_{i,j}^t \right) + \nu_{i,j}^t \left(\nabla^2 \zeta_{i,j}^t - \eta_{i,j}^t \right) \right] + \right. \\
& \left. \sum_{t=1}^{T} \alpha_{i,j}^t \left[\frac{\zeta_{i,j}^t - \zeta_{i,j}^{t-1}}{\Delta t} + \mathcal{J}(\psi,\zeta)_{i,j}^{t-1} + \beta \left(\frac{\psi_{i+1,j}^{t-1} - \psi_{i-1,j}^{t-1}}{2\Delta x} \right) + \epsilon_b \zeta_{i,j}^{t-1} + \epsilon_h \nabla^2 \eta_{i,j}^{t-1} \right] \right)
\end{aligned}
$$

$$(\text{A.1})$$

where $\mathcal{J}$ is the nine-point Arakawa Jacobian defined by

$$\mathcal{J}(\psi,\zeta)_{i,j} \equiv \left[\left(\psi_{i-1,j} - \psi_{i,j-1} \right) \zeta_{i-1,j-1} + \right.$$

$$
\begin{aligned}
&(\psi_{i-1,j-1} + \psi_{i-1,j} - \psi_{i+1,j-1} - \psi_{i+1,j})\, \zeta_{i,j-1} + \\
&(\psi_{i,j-1} - \psi_{i+1,j})\, \zeta_{i+1,j-1} + \\
&(\psi_{i+1,j-1} + \psi_{i,j-1} - \psi_{i+1,j+1} - \psi_{i,j+1})\, \zeta_{i+1,j} + \\
&(\psi_{i+1,j} - \psi_{i,j+1})\, \zeta_{i+1,j+1} + \\
&(\psi_{i+1,j+1} + \psi_{i+1,j} - \psi_{i-1,j+1} - \psi_{i-1,j})\, \zeta_{i,j+1} + \\
&(\psi_{i,j+1} - \psi_{i-1,j})\, \zeta_{i-1,j+1} + \\
&(\psi_{i-1,j+1} + \psi_{i,j+1} - \psi_{i-1,j-1} - \psi_{i,j-1})\, \zeta_{i-1,j} \,]\, \frac{1}{12 \Delta x \Delta y}
\end{aligned}
$$

and the standard five–point Laplacian is used. i and j are the indices for the east–west direction and the north–south direction respectively, t is the index for the time–step.

The forward model equations that are appended to the cost function with Lagrange multipliers in equation (A.1) are in a slightly different yet equivalent form to the forward model equations (1.1) on page 19. The biharmonic operator acting on vorticity in the horizontal friction term of (1.1) somewhat complicates the discretization. To ease the discrete formulation of the forward and adjoint model equations, the state variable, $\eta_{i,j}^t$, is introduced. It is defined by

$$
\nabla^2 \zeta_{i,j}^t = \eta_{i,j}^t.
$$

The boundary conditions for $\eta_{i,j}^t$ need to be specified in order to integrate the forward model equations. $\eta_{i,j}^t$ is set to zero on the boundaries for all time, this assumption about the Laplacian of vorticity on the boundaries does not affect the results significantly (Seiler, 1993).

For the optimization experiments presented in chapter three, the state variables are:

$\psi_{i,j}^t$, $\eta_{i,j}^t$ at interior points for $t = 0, \ldots, T$

$\zeta_{i,j}^t$ at interior points for $t = 1, \ldots, T$.

The control variables are:

ψ_b^t, ζ_b^t for $t = 0, \ldots, T$

$\zeta_{i,j}^0$ at interior points.

where the subscript b denotes the grid points at the edges of the model domain.

138

Following the procedure outlined in the last section, the first variation of L (given by equation A.1) is taken. Setting the gradients of L with respect to the Lagrange multipliers to zero returns the forward model equations. The adjoint model equations are obtained by setting the gradient of L with respect to the state variables to zero, ie.

$\frac{\partial L}{\partial \zeta_{i,j}^t} = 0$ at interior points for $t = 1, \ldots, T$

$\frac{\partial L}{\partial \psi_{i,j}^t} = 0$ at interior points for $t = 0, \ldots, T$

$\frac{\partial L}{\partial \eta_{i,j}^t} = 0$ at all points for $t = 0, \ldots, T$

After much algebra these equations become respectively

$$\frac{\alpha_{i,j}^t - \alpha_{i,j}^{t+1}}{\Delta t} - \mathcal{J}\left(\psi_{i,j}^t, \alpha_{i,j}^{t+1}\right) + \epsilon_b \alpha_{i,j}^{t+1} - \mu_{ij}^t + \nabla^2 \nu_{i,j}^t = 0$$

$$\frac{\partial J}{\partial \psi_{i,j}^t} - \mathcal{J}\left(\alpha_{i,j}^{t+1}, \zeta_{i,j}^t\right) - \beta\left(\frac{\alpha_{i+1,j}^{t+1} - \alpha_{i-1,j}^{t+1}}{2\Delta x}\right) + \nabla^2 \mu_{i,j}^t = 0$$

$$\epsilon_h \nabla^2 \alpha_{i,j}^{t+1} - \nu_{ij}^t = 0 \qquad\qquad (A.2)$$

These three equations are referred to as the adjoint model equations in this study. The first is a prognostic equation for α, the second and third are diagnostic equations for μ and ν respectively. Together with the forward model equations they are called the Euler–Lagrange equations.

The appropriate boundary conditions for the Lagrange multipliers in the adjoint model equations are zero at all boundary points for all time and zero at the final time. The adjoint model equations are integrated backward in time forced by $\frac{\partial J}{\partial \psi_{i,j}^t}$ at interior grid–points. This forcing term can be derived by differentiating the cost function given by equation (1.5) on page 23, with respect to $\psi_{i,j}^t$. This adjoint forcing term is non–zero at grid points and times where the model counterpart of the data is a functional of the streamfunction. Note that if observations of vorticity, or the Laplacian of vorticity, were available there would be forcing terms due to $\frac{\partial J}{\partial \zeta_{i,j}^t}$ and $\frac{\partial J}{\partial \eta_{i,j}^t}$ in the adjoint model equations. This not the case in any of the experiments performed in this study, and observations of such high spatial derivatives are unlikely in the real ocean.

The complete history of streamfunction and vorticity in space and time from the forward model, is needed to integrate the adjoint model equations. This may present a problem in computing memory for long assimilation periods. Here only the streamfunction history needs to be stored from the forward model, as vorticity can be readily calculated from streamfunction and the boundary conditions for vorticity via the Poisson equation.

The first variation of L now only contains the gradients of L with respect to the control variables, ie.

$$
\begin{aligned}
dL = & \sum_{i=2}^{N-1} \sum_{j=2}^{M-1} \frac{\partial L}{\partial \zeta_{i,j}^0} d\zeta_{i,j}^0 + \\
& \sum_{t=0}^{T} \left[\sum_{i=1}^{N} \left(\frac{\partial L}{\partial \psi_{i,1}^t} d\psi_{i,1}^t + \frac{\partial L}{\partial \zeta_{i,1}^t} d\zeta_{i,1}^t + \frac{\partial L}{\partial \psi_{i,M}^t} d\psi_{i,M}^t + \frac{\partial L}{\partial \zeta_{i,M}^t} d\zeta_{i,M}^t \right) + \right. \\
& \left. \sum_{j=2}^{M-1} \left(\frac{\partial L}{\partial \psi_{1,j}^t} d\psi_{1,j}^t + \frac{\partial L}{\partial \zeta_{1,j}^t} d\zeta_{1,j}^t + \frac{\partial L}{\partial \psi_{N,j}^t} d\psi_{N,j}^t + \frac{\partial L}{\partial \zeta_{N,j}^t} d\zeta_{N,j}^t \right) \right] \quad (A.3)
\end{aligned}
$$

Explicit expressions for the derivatives of L with respect to the control variables can be obtained by differentiating equation (A.1). After some algebra we get,

Gradient for initial vorticity at interior points ($i \neq 1$ or N ; $j \neq 1$ or M):

$$
\frac{\partial L}{\partial \zeta_{i,j}^0} = \frac{-\alpha_{i,j}^0}{\Delta t}
$$

where

$$
\alpha_{i,j}^0 \equiv \frac{\partial J}{\partial \zeta_{i,j}^0} - \mu_{i,j}^0 - \frac{\alpha_{i,j}^1}{\Delta t} - \mathcal{J}\left(\psi^0, \alpha^1\right)_{i,j} + \epsilon_b \zeta_{i,j}^0
$$

since $\alpha_{i,j}^0$ is not defined in the augmented Lagrangian. This expression for the gradient with respect to the initial vorticity conditions is that obtained by Tziperman & Thacker (1989).

Gradient for boundary streamfunction at all times (for example along the western edge of the model domain, $i=1$)

$$
\begin{aligned}
\frac{\partial L}{\partial \psi_{1,j}^t} = & \frac{\partial J}{\partial \psi_{1,j}^t} - \frac{\beta}{2\Delta x} \alpha_{2,j}^{t+1} + \frac{\mu_{2,j}^t}{\Delta x^2} - \\
& \left[(\zeta_{1,j+1} - \zeta_{2,j}) \alpha_{2,j+1} + \right.
\end{aligned}
$$

140

$$(\zeta_{1,j+1} + \zeta_{2,j+1} - \zeta_{1,j-1} - \zeta_{2,j-1})\alpha_{2,j} +$$
$$(\zeta_{2,j} - \zeta_{1,j-1})\alpha_{2,j-1}] \frac{1}{12\Delta x \Delta y} \qquad (A.4)$$

Gradient for boundary vorticity at all times (for example on the western edge of the model domain, $i=1$)

$$\frac{\partial L}{\partial \zeta_{1,j}^t} = \frac{\partial J}{\partial \zeta_{1,j}^t} + \frac{\nu_{2,j}^t}{\Delta x^2} +$$
$$[(\psi_{1,j+1} - \psi_{2,j})\alpha_{2,j+1} +$$
$$(\psi_{1,j+1} + \psi_{2,j+1} - \psi_{1,j-1} - \psi_{2,j-1})\alpha_{2,j} +$$
$$(\psi_{2,j} - \psi_{1,j-1})\alpha_{2,j-1}] \frac{1}{12\Delta x \Delta y} \qquad (A.5)$$

The adjoint method works as follows:

(i) A first guess for the control vector is selected.

(ii) Boundary and initial conditions are taken from the control vector and used to integrate the forward model equations forward in time.

(iii) At observation times and locations, the model data misfit is calculated, and at the end of the integration period the value of the cost function is calculated.

(iv) The cost function, the model/data misfits, and the complete forward history of streamfunction are stored.

(v) The adjoint model equations are integrated backward in time, forced by the model/data misfit at observing times and locations.

(v) Along the way, and when $t = 0$ is reached, the gradients of the augmented cost function with respect to boundary and initial conditions are calculated and stored in a vector.

(vi) Values of cost function, gradient vector and control vector, are passed to the gradient-search routine, which returns a new control vector.

(vii) If the norm of the gradient vector is below a certain value then stop. If it is not then go to (ii)

The above sequence of steps is called one iteration of the optimization or minimization.

141

Following are a few comments about the various terms in the adjoint model equations and the gradient expressions:

— The appearance of the cost function J in (A.4) and (A.5) is not due to there being data on the boundaries. This forcing term arises from the terms for size and smoothness of boundary streamfunction and vorticity in the cost function.

Terms are included in J to enforce spatial smoothness of streamfunction and vorticity along the boundaries.

— When the first variation of the augmented cost function given by equation (A.1) is taken, the right–hand side is integrated by parts and manipulated into the form of equation (A.3). This is done in order that the coefficients of $d\zeta_{i,j}^0$, etc. can be equated with the gradients of L in equation (A.3). There are boundary terms resulting from the integration by parts that are due to the spatial derivatives in equation (A.1). Thus on the right–hand side of the expression for the gradient with respect to boundary streamfunction, equation (A.4), the second term is from the $\beta \frac{\partial \psi}{\partial x}$ term in the prognostic equation and the third term is from the Laplacian relating streamfunction to vorticity. The fourth term on the right hand side of equation (A.4) is from the "edge" of the Arakawa Jacobian along the western boundary. For the continuous integral formulation of the adjoint, it can be shown that as Δx, $\Delta y \to 0$ this latter term becomes $\alpha \frac{\partial \psi}{\partial y}$.

The interior flow field, during the evolution of the forward model, responds to the boundary values of streamfunction and vorticity through the various spatial derivatives. As the adjoint model equations are integrated backward in time the Lagrange multipliers advect and propagate the model/data misfit throughout the interior. The adjoint forms of the various spatial derivatives near the boundaries, as described above, allow the gradient of the cost with respect to boundary streamfunction and vorticity to respond to interior forcing.

— The forward model equations, that are used as a strong constraint in the augmented cost function (equation A.1), only hold at the interior grid–points. The disadvantage

of this is that streamfunction and vorticity at the boundary grid–points are not required to obey any dynamical constraints. Thus the gradients of the augmented cost function with respect to boundary streamfunction and vorticity, equations (A.4) and (A.5), only contain contributions from terms in the forward model equations that have spatial derivatives. There is no constraint on the temporal evolution of boundary streamfunction and vorticity.

Now from the adjoint model equations which govern the behavior of the Lagrange multipliers in the interior, equations (A.2), one can see that the Laplacian of μ is proportional to the forcing term from the model/data misfit, $\frac{\partial J}{\partial \psi_{i,j}^t}$. This Poisson equation needs to be solved for μ at each time–step as the adjoint model equations are integrated backward in time. Due to the elliptic character of the Poisson equation, the field of of μ at all interior grid points instantaneously responds to any changes in $\frac{\partial J}{\partial \psi_{i,j}^t}$.

The gradient with respect to boundary streamfunction, equation (A.4), is proportional to the Lagrange multiplier, μ, at the grid–points adjacent to the boundary points. Thus at an observation time, the gradient with respect to boundary streamfunction instantaneously responds at all boundary points, to the forcing by $\frac{\partial J}{\partial \psi_{i,j}^t}$. These instantaneous responses produce spikes at observation times, in the gradient with respect to boundary streamfunction. In the course of the minimization the control vector is preferentially varied in the directions of these high gradients. Hence for data that is sampled sparsely in time, the values of streamfunction all around the boundary will show sensitivity to the data at the sampling times.

Because there are no temporal constraints on the boundary streamfunction or vorticity, the spikes in the boundary streamfunction are not smoothed at all by the dynamics.

The gradient with respect to boundary vorticity, equation (A.5), does not exhibit this type of behavior as it is not proportional to interior values of μ. The instantaneous domain–wide changes in μ appear as a forcing in the prognostic equa-

tion for α. The field of α is therefore smooth in time, resulting in smooth fields of ν. Hence the gradient with respect to boundary vorticity is smooth in time.

— The particular gradient–search method that is to minimize the cost function is the L–BFGS method, which is a limited–memory quasi–Newton method. The reader is referred to Zou *et al.* (1993) and Wang *et al.* (1995), who describe the L–BFGS method in detail. For this method the iterative search for the minimum stops when the norm of the gradient vector falls below a pre–determined value. In this study the pre–determined value is chosen by calculating the gradient when the true values of the control variables are supplied as the first guess for the minimization. Gill *et al.*, (1981), give a comprehensive treatment of methods of solving nonlinear optimization problems.

— Navon *et al.* (1992) indicate that the large scale features of the flow field are constructed during the first several iterations of the minimization using the conjugate gradient method to look for the minimum of the cost function. Later iterations make finer adjustments that do not affect the flow field significantly.

REFERENCES

Bennett, A. F., 1992: *Inverse methods in physical oceanography*, Cambridge University Press, New York, 346 pp.

Bennett, A. F., and P. E. Kloeden, 1981: The ill–posedness of open ocean models, J. Phys. Oceanogr., **11**, 1027–1029.

Bennett, A. F., and P. C. McIntosh, 1982: Open ocean modeling as an inverse problem, J. Phys. Oceanogr., **12**, 1004–1018.

Bevington, P. R., and D. K. Robinson, 1992: *Data Reduction and Error Analysis for the Physical Sciences*, McGraw–Hill, New York, 328 pp.

Blumberg, A., and L. Kantha, 1985: Open boundary condition for circulation models, J. Hydrol. Eng., **111**, No. 2, 237–255.

Bretherton, F. P., R. E. Davis and C. B. Fandry, 1976: A technique for objective analysis and design of oceanographic experiments applied to MODE-73, Deep–Sea Res., **23**, 559–582.

Bryden, H. L., 1982: Sources of eddy activity in the Gulf Stream recirculation region, J. Marine. Res., **40**, 1047–1068.

Bryson, A. E. Jr., and Y–C Ho, 1975: *Applied Optimal Control*, Hemisphere, New York, 481 pp.

Chapman, D. C., 1985: Numerical treatment of cross–shelf open boundaries in a barotropic coastal ocean model, J. Phys. Oceanogr., **15**, 1060–1075.

Charney, J. G., R. Fjørtoft and J. von Neumann, 1950: Numerical integration of the barotropic vorticity equation, Tellus, **2**, 237–254.

Chester, D. B., 1993: A tomographic view of the Gulf Stream southern recirculation gyre at 38°N, 55°W. PhD thesis, Mass. Inst. of Technol./Woods Hole Oceanogr. Inst. Joint Program, Cambridge, Mass., 165pp.

Chester, D., P. Malanotte–Rizzoli, J. Lynch and C. Wunsch, 1994: The eddy radiation field of the Gulf Stream as measured by ocean acoustic tomography, Geophys. Res. Let., **21**, No. 3, 181–184.

Evenson, G., 1994: Inverse methods and data assimilation in nonlinear ocean models, Physica D, (in press).

Flierl, G. R., 1978: Models of vertical structure and the calibration of two–layer models, Dyn. Atmos. Ocean., **2**, 341–381.

Flierl, G. R., P. Malanotte–Rizzoli and N. J. Zabusky, 1987: Nonlinear waves and coherent vortex structures in barotropic β–plane jets, J. Phys. Oceanogr., **17**, 1408–1438.

Ghil, M., and P. Malanotte–Rizzoli, 1991: Data assimilation in meteorology and oceanography, Adv. Geoph., **33**, 141–266.

Gill, P. E., W. Murray, and M. H. Wright, 1981: *Practical Optimization*, Academic, San Diego, Calif., 386 pp.

Hogg, N. G., 1985: Evidence for baroclinic instability in the Gulf Stream recirculation region, Prog. Oceanog., **14**, 209–229.

Hogg, N. G., 1988: Stochastic wave radiation by the Gulf Stream, J. Phys. Oceanogr., **18**, 1687–1701.

Hogg, N. G., 1992: On the transport of the Gulf Stream between Cape Hatteras and the Grand Banks, Deep–Sea Res., **39**, 1231–1246.

Hogg, N. G., 1993: Toward parameterization of the eddy field near the Gulf Stream, Deep–Sea Res., **40**, No. 11–12, 2359–2376.

Hogg, N. G., 1994: Observations of Gulf Stream meander–induced disturbances, J. Phys. Oceanogr., **24**, 2534–2545.

Holland, W. R., and P. B. Rhines, 1980: An example of eddy–induced ocean circulation, J. Phys. Oceanogr., **10**, 1010–1031.

Hua, B. L., J. C. McWilliams and W. B. Owens, 1986: An objective analysis of the POLYMODE Local Dynamics Experiment. Part II: Streamfunction and potential vorticity fields during the intensive period, J. Phys. Oceanogr., **16**, 506–522.

Lacarra, J–F, and O. Talagrand, 1988: Short–range evolution of small perturbations in a barotropic model, Tellus, **40A**, 81–95.

Levitus, S., 1982: Climatological Atlas of the World Ocean, NOAA Professional Paper, *No. 13*, U.S. Gov. Printing Office, 173 pp.

Liebelt, P. B., 1967:*An Introduction to Optimal Estimation*, Addison–Wesley, Reading, Mass., 273 pp.

Malanotte–Rizzoli, P., 1984: Boundary–forced nonlinear planetary radiation, J. Phys. Oceanogr., **14**, 1032–1046.

Malanotte–Rizzoli, P., D. B. Haidvogel and R. E. Young, 1987: Numerical solution of transient boundary–forced radiation. Part I: The linear regime, J. Phys. Oceanogr., **17**, 1439–1457.

Malanotte–Rizzoli, P., N. G. Hogg and R. E. Young, 1995: Stochastic wave radiation by the Gulf Stream: numerical experiments, Deep–Sea Res., **42**, 389–423.

Malanotte–Rizzoli, P., and R. E. Young, 1992: How useful are localized clusters of traditional oceanographic measurements for data assimilation ?, Dyn. Atm. Oceans, **17**, 23–61.

Marotzke, J., and C. Wunsch, 1993: Finding the steady state of a general circulation model through data assimilation: application to the North Atlantic Ocean, J. Geophys. Res., **98**, 20149–20167.

Moore, A. M., 1991: Data assimilation in a quasi–geostrophic open–ocean model of the Gulf Stream region using the adjoint method, J. Phys. Oceanogr., **21**, 398–427.

Morse, P. M., and H. Feshbach, 1953: *Methods of Theoretical Physics*, Vol. I, McGraw–Hill, New York, 997 pp.

Navon, I. M., X. L. Zou, J. Derber and J. Sela, 1992: Variational data assimilation with an adiabatic version of the NMC spectral model, Mon. Wea. Rev., **120**, 1433–1466.

Orlanski, I., 1976: A simple boundary condition for unbounded byperbolic flows, J. Comput. Phys., **21**, 251–269.

Pedlosky, J., 1977: On the radiation of mesoscale energy in the mid–ocean, Deep–Sea Res., **24**, 591–600.

Pedlosky, J., 1979: *Geophysical Fluid Dynamics*, Springer–Verlag, New York, 624pp.

Plumb, R. A., 1986: Three–dimensional propagation of transient quasi–geostrophic eddies and its relationship with the eddy–forcing of the time–mean flow, J. Atmos. Sci., **43**, 1657–1678.

Press, W. H., B. P. Flannery, S. A. Teukolsky, and W. T. Vetterling, 1986: *Numerical Recipes*, Cambridge University Press, New York, 818 pp.

Richman, J. G., C. Wunsch and N. G. Hogg, 1977: Space and time scales of mesoscale motion in the western North Atlantic, Rev. Geoph. Space Phys., **15**, 385–420.

Robinson, A. R., and D. B. Haidvogel, 1980: Dynamical forecast experiments with a barotropic open ocean model, J. Phys. Oceanogr., **10**, 1909–1928.

Robinson, A. R., M. A. Spall and N. Pinardi, 1988: Gulf Stream simulations and the dynamics of ring and meander processes, J. Phys. Oceanogr., **18**, 1320–1353.

Schiller, A., 1995: The mean circulation of the Atlantic Ocean north of 30S determined with the adjoint method applied to an ocean general circulation model, J. Marine. Res., **53**, 453–497.

Schmitz, W. J., 1976: Eddy kinetic energy in the deep western North Atlantic, J. Geophys. Res., **81**, 4981–4982.

Schröter, J., and C. Wunsch, 1986: Solution of nonlinear finite difference ocean models by optimization methods with sensitivity and observational strategy analysis, J. Phys. Oceanogr., **16**, 1855–1874.

Seiler, U., 1993: Estimation of Open Boundary Conditions With the Adjoint Method, J. Geophys. Res., **98**, 22,855–22,870.

Talagrand, O., and P. Courtier, 1987: Variational assimilation of meteorological observations with the adjoint vorticity equation. I: Theory, Q. J. R. Meteorol. Soc., **113**, 1311–1328.

Thacker, W. C., 1988: Fitting models to inadequate data by enforcing spatial and temporal smoothness, J. Geophys. Res., **93**, 10,655–10,665. b

Thacker, W. C., 1989: The role of the Hessian matrix in fitting models to measurements, J. Geophys. Res., **94**, 6177–6196.

Thacker, W. C., and R. B. Long, 1988: Fitting dynamics to data, J. Geophys. Res., **93**, 1227–1240.

Tziperman, E., and W. C. Thacker, 1989: An optimal–control/adjoint–equations approach to studying the oceanic general circulation, J. Phys. Oceanogr., **19**, 1471–1485.

Vallis, G. K., 1983: On the predictability of quasi–geostrophic flow: the effects of beta and baroclinicity, J. Atmos. Sci., **40**, 10–27.

Wang, Z., I. M. Navon, F. X. LeDimet and X. Zou, 1992: The second order adjoint analysis: theory and applications, Meteorol. Atmos. Phys., **50**, 3–20.

Wyrtki, K., L. Magaard and J. Hager, 1976: Eddy energy in the oceans, J. Geophys. Res., **81**, 2641–2646.

Zou, J., W. W. Hsieh and I. M. Navon, 1995: Sequential open–boundary control by data assimilation in a limited–area model, Mon. Wea. Rev., **123**, 1–11.

Zou, X., I. M. Navon, M. Berger, K. H. Phua, T. Schlick and F. X. LeDimet, 1993: Numerical experience with limited–memory quasi–newton and truncated newton methods, SIAM J. Optimization, **3**, 582–608.

University of California, San Diego
SIO Library 0175C
9500 Gilman Drive
La Jolla, CA 92093-0175

Hancock Library of Biology & Oceanography
Alan Hancock Laboratory
University of Southern California
University Park
Los Angeles, CA 90089-0371

Gifts & Exchanges
Library
Bedford Institute of Oceanography
P.O. Box 1006
Dartmouth, NS, B2Y 4A2, CANADA

Commander
International Ice Patrol
1082 Shennecossett Road
Groton, CT 06340-6095

NOAA/EDIS Miami Library Center
4301 Rickenbacker Causeway
Miami, FL 33149

Research Library
U.S. Army Corps of Engineers
Waterways Experiment Station
3909 Halls Ferry Road
Vicksburg, MS 39180-6199

Institute of Geophysics
University of Hawaii
Library Room 252
2525 Correa Road
Honolulu, HI 96822

Marine Resources Information Center
Building E38-320
MIT
Cambridge, MA 02139

Library
Lamont-Doherty Geological Observatory
Columbia University
Palisades, NY z10964

Library
Serials Department
Oregon State University
Corvallis, OR 97331

Pell Marine Science Library
University of Rhode Island
Narragansett Bay Campus
Narragansett, RI 02882

Working Collection
Texas A&M University
Dept. of Oceanography
College Station, TX 77843

Fisheries-Oceanography Library
151 Oceanography Teaching Bldg.
University of Washington
Seattle, WA 98195

Library
R.S.M.A.S.
University of Miami
4600 Rickenbacker Causeway
Miami, FL 33149

Maury Oceanographic Library
Naval Oceanographic Office
Building 1003 South
1002 Balch Blvd.
Stennis Space Center, MS, 39522-5001

Library
Institute of Ocean Sciences
P.O. Box 6000
Sidney, B.C. V8L 4B2
CANADA

Library
Institute of Oceanographic Sciences
Deacon Laboratory
Wormley, Godalming
Surrey GU8 5UB
UNITED KINGDOM

The Librarian
CSIRO Marine Laboratories
G.P.O. Box 1538
Hobart, Tasmania
AUSTRALIA 7001

Library
Proudman Oceanographic Laboratory
Bidston Observatory
Birkenhead
Merseyside L43 7 RA
UNITED KINGDOM

IFREMER
Centre de Brest
Service Documentation - Publications
BP 70 29280 PLOUZANE
FRANCE

50272-101

REPORT DOCUMENTATION PAGE	1. REPORT NO. MIT/WHOI 95-23	2.	3. Recipient's Accession No.

4. Title and Subtitle Estimating Open-Ocean Boundary Conditions: Sensitivity Studies	5. Report Date September 1995
	6.

7. Author(s) James R. Gunson	8. Performing Organization Rept. No.

9. Performing Organization Name and Address MIT/WHOI Joint Program in Oceanography/Applied Ocean Science & Engineering	10. Project/Task/Work Unit No. MIT/WHOI 95-23
	11. Contract(C) or Grant(G) No. (C) (G)

12. Sponsoring Organization Name and Address Funding was provided by the Office of Naval Research through Grants N00014-90-J-1481 and N00014-95-1-0226 through the Massachusetts Institute of Technology.	13. Type of Report & Period Covered Ph.D. Thesis
	14.

15. Supplementary Notes

This thesis should be cited as: James R. Gunson, 1995. Estimating Open-Ocean Boundary Conditions: Sensitivity Studies. Ph.D. Thesis. MIT/WHOI, 95-23.

16. Abstract (Limit: 200 words)

The estimation of boundary conditions for an open-ocean model is addressed here. To mimick the SYNOP experiment in the Gulf Stream, a meandering jet is modeled by the nonlinear barotropic vorticity equation. Simulated observations of velocity are taken. Twin experiments are performed using the adjoint method of assimilating data. Various choices of scaling and first guess for the control variables are applied with various observational strategies. A major new result obtained is the successful estimation of the complete set of initial and boundary conditions. Starting from persistence, temporal variations at the boundaries are created that make the interior flow match well the velocity observations. The spread of information from the observations to the boundaries is investigated. The evaluation of the full error covariance matrix for the control variables from the inverse Hessian is investigated along with its dependence upon the degree of nonlinearity in the dynamics. Further major new results here obtained are the availability of off-diagonal covariances, and the calculation of error covariances for all boundary and initial conditions and for interior fields of streamfunction and vorticity. The role of the Hessian matrix is assessed in gauging the sensitivity of the estimated boundary and initial conditions to the observations.

17. Document Analysis   a. Descriptors

boundary
adjoint
assimilation

b. Identifiers/Open-Ended Terms

c. COSATI Field/Group

18. Availability Statement Approved for publication; distribution unlimited.	19. Security Class (This Report) UNCLASSIFIED	21. No. of Pages 153
	20. Security Class (This Page)	22. Price

(See ANSI-Z39.18)	See Instructions on Reverse	OPTIONAL FORM 272 (4-77) (Formerly NTIS-35) Department of Commerce